

ABSTRACT

Title of Document: CHANGES IN THE SEASONAL AMPLITUDE OF
 ATMOSPHERIC CARBON DIOXIDE
 CONCENTRATION: CAUSES AND FUTURE
 PROJECTIONS

Fang Zhao, Doctor of Philosophy, 2015

Directed By: Professor Ning Zeng and Professor Eugenia Kalnay
 Department of Atmospheric and Oceanic Science

The atmospheric carbon dioxide (CO₂) observations reveal a seasonal cycle that is dominated by the growth and decay of land vegetation. Ground-based and aircraft-based observations indicate that the amplitude of this seasonal cycle has increased over the past five decades, suggesting enhanced biosphere activity. Previous studies have tried to explain the amplitude increase with stimulated vegetation growth by higher concentrations of CO₂ and warming, but the understanding of all the important mechanisms and their relative contribution is still lacking. This work comprises of three individual studies that contribute to better understanding of the CO₂ amplitude increase over time and space. With improved crop simulation scheme in a terrestrial carbon model, a new mechanism—the intensive farming practices of the agricultural Green Revolution—is presented as a driver of changes in the seasonal features of the global carbon cycle. Results are

further compared with eight other models' simulations and a number of observation-based datasets on the seasonal characteristics of simulated carbon flux, and on the relative contribution of rising CO₂, climate and land use/cover change. In addition, future projections on the amplitude change of CO₂ seasonal cycle are examined using simulations from 10 Coupled Model Intercomparison Project Phase 5 (CMIP5) earth system models. Results from this work demonstrate that human land-management activities are powerful enough to modify the basic seasonal characteristics of the biosphere, as reflected by atmospheric CO₂. Models attribute $83 \pm 56\%$, $-3 \pm 74\%$ and $20 \pm 30\%$ of global carbon flux amplitude increase to the CO₂, climate and land use/cover factors, respectively. Additionally, the models' underlying mechanisms for the simulated carbon flux amplitude increase in different regions are substantially different. Strong productivity increase under higher CO₂ concentration is also seen in the CMIP5 models, leading to $62 \pm 19\%$ global mean CO₂ amplitude increase in 2081-2090 compared to 1961-1970. Both groups of models suggest that models simulating larger amplitude increase tend to show a larger gain in land carbon sink (with a cross-model R² of ~0.5 in both cases). Overall, this work presents significant insights in the change of CO₂ amplitude and model representation of global carbon cycle.

CHANGES IN THE SEASONAL AMPLITUDE OF ATMOSPHERIC CARBON
DIOXIDE CONCENTRATION: CAUSES AND FUTURE PROJECTIONS

By

Fang Zhao

Dissertation submitted to the Faculty of the Graduate School of the
University of Maryland, College Park, in partial fulfillment
of the requirements for the degree of
Doctor of Philosophy
2015

Advisory Committee:
Professor Ning Zeng, Chair/Advisor
Professor Eugenia Kalnay, Co-Advisor
Professor George Hurtt
Professor Ross Salawitch
Professor Antonio Busalacchi

© Copyright by
Fang Zhao
2015

Dedication

To my parents, thank you for everything.

Acknowledgements

First and foremost, I owe my deepest gratitude to Ning Zeng, who has invested tremendous amount of time in teaching me the VEGAS model, improving my coding habits and instilling me the right mentality in solving problems and scientific communication. I thoroughly enjoyed the learning experience and scientific discoveries while discussing the model simulation results with him. I always felt progress after each of our long and productive meeting, and I constantly benefited from his vision and experience. After a few years of doing research under his supervision, I become more confident as an independent researcher. I shall always remember and benefit from his valuable suggestions in my future work.

I am also very grateful for the advising and encouragement from Eugenia Kalnay, who have kindly brought me into the excellent Ph.D. program here at University of Maryland, one month earlier than the start date. That period of head start was especially valuable for me in learning scientific tools and adjusting to Ph.D. life, which was never easy coming from a geography background. She also graciously involved me into her human-earth modeling effort, and as part of the work, I developed a river routing model. That valuable experience was very helpful for me getting a postdoctoral job in Germany, working on the water sector of the ISI-MIP2 project.

I would like to thank other members of my dissertation committee, George Hurtt, Ross Salawitch, Antonio Busalacchi, for their generous and valuable support. In addition, I thank James Collatz and Tristram West for sharing their expertise during the start of this project. I appreciate the teaching of our professors in the

department, who spent so much time helping us to learn the core concepts of atmospheric and earth science. I also thank the support from my classmates and friends, and our wonderful staff members in the department. Special thanks also to Rashid Rafique who generously helped to improve the dissertation.

I am very grateful to David Keeling, a visionary scientist whose meticulous work makes the high quality long-term CO₂ observation possible, therefore building foundation for the following scientific discoveries including the ones in this dissertation. Thanks also to many other scientists whose efforts provide valuable observations and observation-based datasets to evaluate the models in this work.

I would like to extend my gratification to multiple model intercomparison coordination teams, EMICAR5, TRENDY MsTMIP and CMIP5 for designing the framework and organizing the simulation efforts. Participating in EMICAR5, TRENDY (multiple phases), MsTMIP and ISI-MIP have offered valuable opportunity for me to better understand our VEGAS model, gain experience in supercomputer computing, and communicate with great scientists worldwide. Thanks also to countless fellow modelers who spent considerable effort in providing the simulation data to the science community.

Finally, and most importantly, I am deeply grateful to my parents, Zonghua Zhao and Xianhui Hu, for their patience and understanding throughout the six years of my graduate study in a foreign country.

Table of Contents

Dedication	ii
Acknowledgements	iii
Table of Contents	v
List of Tables	vii
List of Figures	ix
Chapter 1: Introduction	1
Background	1
Causes of historical CO ₂ seasonal amplitude increase	4
The CO ₂ fertilization effect	4
Climate change impact	6
Land use/cover change	9
Priority Questions Regarding CO ₂ amplitude increase	9
Objectives	10
The Dissertation and its Organization	10
Chapter 2: The agricultural Green Revolution as a driver of the increasing atmospheric CO ₂ seasonal amplitude	13
Preface	13
Abstract	13
Introduction	14
Results and Discussion	18
Mean seasonal cycle	18
Temporal evolution	21
Spatial pattern	23
Natural vegetation vs. cropland	25
Data	28
Research significance	30
Methods	30
Data	30
Modeling the agricultural Green Revolution	32
Validation of crop simulation	37
Sensitivity experiment on land cover effects	40
Availability of data and model output	40
Supplementary Information	41
Acknowledgement	42
Author contributions	42
Chapter 3: Attributing the role of CO ₂ , climate and land use in regulating the seasonal carbon fluxes in terrestrial ecosystems: a multimodal analysis	43
Preface	43
Abstract	44

Introduction.....	45
Methods.....	49
Terrestrial Ecosystem Models.....	49
Observations and observational based estimates	50
Calculating the mean seasonal cycle and its amplitude change.....	51
Factorial analyses.....	52
Spatial attribution.....	53
Results.....	54
Mean seasonal cycle of F_{TA}	54
Temporal evolution of FTA seasonal amplitude	61
Attribution of global and regional FTA seasonal amplitude	64
Discussion and conclusion.....	73
Supplementary figures	78
Appendix.....	81
A. Environmental drivers for TRENDY.....	81
B. Environmental drivers for TRENDY	82
Acknowledgement	83
Chapter 4: Continued increase in atmospheric CO ₂ seasonal amplitude in the 21st century projected by the CMIP5 Earth system models.....	84
Preface.....	84
Abstract.....	84
Introduction.....	85
Method	89
Model descriptions.....	89
Analysis procedure.....	90
Results.....	93
Changes of CO ₂ and NBP seasonal amplitude	93
Production vs. respiration	98
Spatial and latitudinal contributions	101
Mechanisms for amplitude increase.....	107
Relationship with mean carbon sink.....	110
Discussion.....	112
Conclusion	129
Acknowledgements.....	130
Chapter 5: Conclusion and future perspective	131
Bibliography	141

List of Tables

Table 2-1: Summary of changes in population, cropland area, and crop production from 1961 to 2010 from FAO data and other statistics, and Harvest Index (HI), Management Intensity (MI) and NPP_{crop} from the VEGAS model. Crop production is harvested edible parts of crops, while NPP_{crop} is total biomass production including above and below-ground biomass. Harvest Index (HI) is grain and above-ground biomass ratio. All are measured in terms of carbon mass, which is typically about 50% of plant dry mass. Model results are in parentheses.	17
Table 2-2: The trend of CO_2 seasonal amplitude change from three model sensitivity experiments. Each experiment has only a single forcing of climate (CLIM) or CO_2 (CO_2) or land use and management (LU) change. Their percentage contributions are in parenthesis and the total is SUM. Additionally, the experiment ALL is the simulation with all three forcings as in Figures 2-2 and 2-3. The trend is calculated with a least-square linear fit of the unsmoothed time series of seasonal amplitude of modeled land-atmosphere carbon flux F_{TA} , and may be somewhat different from a visual inspection of Figure 2-2 where the data has been smoothed to remove interannual variability.	21
Table 3-1: Basic information for the nine TRENDY models used in this study.	49
Table 3-2: Global mean net land carbon flux, seasonal amplitude, the maximum and minimum months of F_{TA} for the nine TRENDY models and their ensemble mean during 1961-1970 and 2001-2010 periods. For the later period, characteristics of the atmosphere inversions Jena99 and CarbonTracker are also listed.	55
Table 3-3: The seasonal amplitude (maximum minus minimum, in $PgC\ y^{-1}$) of mean net carbon flux for 2001-2010 relative to the 1961-1970 period, according to the nine TRENDY models (values are listed as percentage change in brackets, for both regions and the entire globe). The four large latitudinal regions are the same as in Figure 3: boreal (50-90N), temperate (23.5-50N), Northern tropics (0-23.5N), Southern tropics (0-23.5S), and Southern extra-tropics (23.5-90S). Values from the two inversions Jena99 and CarbonTracker are also listed for comparison.	64
Table 3-4: Global and regional attribution of CO_2 , climate change and land use/cover change effects on the relative amplitude changes of F_{TA} simulated by the TRENDY models, and the ensemble mean of the relative changes during 1961-2012 period ($\% y^{-1}$). The models are listed in the order of simulated S3 global relative amplitude increase for this period (most to least).	66
Table 4-1: List of Models used and their characteristics	90
Table 4-2: Amplitude (maximum minus minimum) of global mean column atmospheric CO_2 , CO_2 growth rate (CO_2g) and global total NBP, averaged over 1961-	

1970 and 2081-2090 for the nine models, and their multi-model ensemble (MME) and standard deviation (SD)..... 95

Table 4-3: Amplitude increase (ppm) and trends of maxima/minima of surface CO₂ from eight models, their multi-model ensemble (MME), and ESRL's Global mean CO₂ (CO₂GL)..... 96

Table 4-4: Column atmospheric CO₂ and NBP amplitude (computed by CCGCRV, slightly different from max minus min) Increases of nine models by 2081-2090 relative to their 1961-1970 values and their multi-model ensemble (MME). 98

List of Figures

Figure 1-1: Monthly mean atmospheric carbon dioxide at Mauna Loa Observatory, Hawaii from 1958 to 2015 (red curve). The black curve presents the long-term trend, after correction for the average seasonal cycle. (Figure from NOAA/ESRL: www.esrl.noaa.gov/gmd/ccgg/trends/, accessed on Sep 8, 2015) 1

Figure 1-2: Time series of the relative amplitude of the seasonal cycle of atmospheric CO₂ at the MLO (black) and anomalies in observed annual land temperatures (red) for the latitudinal band from 30°N to 80°N (except Greenland). The relative amplitudes are in respect to the mean amplitude of the first 5 year of CO₂ record (1959–1963). Temperature anomalies are relative to the 1959–2004 study period (Buermann et al., 2007). 7

Figure 1-3: Change in amplitude of the seasonal cycle of CO₂ between 1958 to 1961 and 2009 to 2011 versus amplitude of the seasonal cycle for 2009 to 2011 at 500 mb, averaged over 45° to 90°N, in observations and in simulations of the CMIP5 land models (Graven et al., 2013). 8

Figure 2-1: Changing world population (billions), cropland area (million kilometer squared) and annual crop production (PgC) during 1961-2010. Crop production tripled to support 2.5 times more people on only 20% more cropland area, enabled by the agricultural Green Revolution. Plotted in (c) is the VEGAS model simulated crop production, compared to estimate from FAO statistics. The inset in (c) shows modeled GPP for three periods 1901-10, 1961-70, and 2001-10 for a location in the US Midwest agricultural belt (98W, -40N) that was initially naturally vegetated and later converted to cropland. The change in seasonal characteristics from these transitions may have contributed to the change in atmospheric CO₂ seasonal amplitude. 16

Figure 2-2: Temporal evolution of seasonal amplitude. Trends for VEGAS simulated land-atmosphere carbon flux F_{TA} (black), of MLO CO₂ mixing ratio (CO₂_{MLO}, green) and global CO₂ mixing ratio (CO₂_{GLOBAL}, purple), and F_{TA} from atmospheric inversions of Jena81 (red), Jena99 (brown), and CarbonTracker (blue). Changes are relative to the 1961-70 mean for VEGAS and the other time series are offset to have the same mean for 2001-2010. Seasonal amplitude is calculated as the difference between the maximum and the minimum of each year after detrending and band pass filtering with a standard tool CCGCRV (Extended Data Fig. 3). A 7-year bandpass smoothing removes interannual variability whose 1- σ standard deviation is shown for CO₂_{MLO} (green shading) and VEGAS F_{TA} (grey shading). Inset: average seasonal cycle of VEGAS F_{TA} (PgC y⁻¹) for the two periods 1961-70 and 2001-10, showing enhanced CO₂ uptake during spring/summer growing season. 19

Figure 2-3: Average seasonal cycle of land-atmosphere carbon flux. F_{TA} (in PgC y^{-1}) for the period 2001-2010 from VEGAS model, compared to atmospheric inversions of Jena81, Jena99, and CarbonTracker. 20

Figure 2-4: Time series analysis for seasonal cycles. (a) MLO CO_2 ; (b) MLO CO_2 growth rate ($d\text{CO}_2/dt$); (c) Net land-atmosphere carbon flux (F_{TA}) from VEGAS; (d) Net land-atmosphere carbon flux from the atmospheric inversion of Jena81. Trends and high frequency variations have been removed following Thoning et al. (1989)²³. Seasonal amplitude in Figures 2-3 is calculated as the difference between maximum and minimum of each year. 22

Figure 2-5: Latitude dependence of the seasonal amplitude of land-atmosphere carbon flux. Fluxes are summed over latitude bands for the VEGAS model and from two atmospheric CO_2 inversions Jena99 and the CarbonTracker. Northern Hemisphere (NH) mid-high latitude region, driven by winter-summer temperature contrast, is the main contributor. The Southern Hemisphere has opposite phase from the NH, but its contribution to global total is small due to its small land area. The two subtropical maxima around 10N and 10S are due to the wet-dry seasonal shift in the Inter-Tropical Convergence Zone (ITCZ) and monsoon movement that are out of phase and largely cancel each other out in terms of their net contribution to global total F_{ta} seasonal amplitude. The results are resampled into 2.5° latitude bands and the unit is PgC y^{-1} per 2.5° latitude from the original resolutions of $0.5^\circ \times 0.5^\circ$ for VEGAS, $5.0^\circ \times 5.0^\circ$ for Jena99 and $1.0^\circ \times 1.0^\circ$ for CarbonTracker. 24

Figure 2-6: Latitudinal distribution of the seasonal amplitude of land-atmosphere carbon flux. Calculated separately for natural vegetation (green lines) and cropland (red lines), for the averages of two periods 1961-1970 (dashed) and 2001-2010 (solid). Unit: PgC y^{-1} per 2.5° degree latitude. 25

Figure 2-7: Modeled linear trends (kgC m^{-2} over 50 years, upper panel) from 1961 to 2010 show major increases in agricultural areas of North America, Europe and Asia (lower panel: crop fraction in 2000). There are also wide spread increases in much of Northern Hemisphere especially the high latitude regions in response to warming and CO_2 fertilization effect. Together, they are mostly responsible for the increase in F_{TA} and CO_2 seasonal amplitude. Decreases in some regions are due to climate trends. . 27

Figure 2-8: Sun-induced chlorophyll fluorescence (SIF). Measurements with the GOME-2 instrument on board the MetOp-A satellite platform (Guanter et al., 2014) are compared to GPP estimates from the data-driven model from MPI-BGC (Jung et al., 2011), and 4 mechanistic carbon cycle models (VEGAS, LPJ, Orchidee, and LPJ-Guess) from the TRENDY international project. 28

Figure 2-9: Attribution of causes with factorial analysis. Relative change of seasonal amplitude from three sensitivity experiments, each with a single forcing: climate only (CLIM), CO_2 only (CO_2), and land use and management only (LU). The results from CO_2 and LU are added on top of CLIM sequentially. The ALL experiment is the same as in Fig.2, driven by all three forcings. 29

Figure 2-10: Management Intensity (MI, relative to year 2000) and Harvest Index (HI) change over time as used in the model. The analytical functions are hyperbolic tangent (see text), and the parameter values correspond to 10% smaller MI in 1961 compared to 2010, and the HI index is 0.31 in 1961 and 0.49 in 2010, based on literature review (Sinclair, 1998). 34

Figure 2-11: Model-Data site validation. Comparison of VEGAS model (line) and FLUXNET observations (circles) at an agricultural site Bondville, Illinois (88.290398W, 40.006199N). (a) GPP, (b) R_e (total ecosystem respiration), (c) NEE ($=R_e - GPP$; Net Ecosystem Exchange, i.e., net land-atmosphere carbon flux), in $gC\ m^{-2}\ month^{-1}$. Shown are seasonal cycles averaged over the period 1996-2007. 39

Figure 2-12: Uncertainty due to model parametric errors in representing agricultural NPP. 42

Figure 3-1: Mean seasonal cycle of global net carbon flux from nine TRENDY models (S3 experiment) and two inversions, Jena99 and CarbonTracker, averaged over 2001-2010. 54

Figure 3-2: Mean seasonal cycle of net carbon flux totals over boreal (50-90N), Northern temperate (23.5-50N), Northern tropics (0-23.5N), Southern tropics (0-23.5S) and Southern extra-tropics (23.5-90S) from nine TRENDY models and two inversions, Jena99 and CarbonTracker, averaged over 2001-2010. 57

Figure 3-3: Latitude dependence of the seasonal amplitude of land-atmosphere carbon flux from the TRENDY multi-model median (red line, and the pink shade indicates 10 to 90 percentile range of model spread) and two atmospheric CO_2 inversions Jena99 and CarbonTracker. Fluxes are first resampled to $2.5^\circ \times 2.5^\circ$ grids, then summed over each 2.5° latitude bands ($PgC\ y^{-1}$ per 2.5° latitude) for the TRENDY ensemble and inversions. 58

Figure 3-4: Latitude dependence of the seasonal amplitude of land-atmosphere carbon flux from each TRENDY model and two atmospheric CO_2 inversions Jena99 (black dashed) and the CarbonTracker (grey dashed). Fluxes are first resampled to $2.5 \times 2.5^\circ$ grids, then summed over each 2.5° latitude bands ($PgC\ y^{-1}$ per 2.5° latitude) for the TRENDY ensemble and inversions. 59

Figure 3-5: The F_{TA} minimum (peak carbon uptake) month for the 2001-2010 average for each spatial grid based on the S3 experiment results from the nine TRENDY models. 60

Figure 3-6: The F_{TA} maximum (peak carbon release) month for the 2001-2010 average for each spatial grid based on the S3 experiment results from the nine TRENDY models. 60

Figure 3-7: Trends for seasonal amplitude of TRENDY simulated multi-model ensemble mean land-atmosphere carbon flux F_{TA} (black), of MLO CO_2 mixing ratio

(CO₂_{MLO}, green) and global CO₂ mixing ratio (CO₂_{GLOBAL}, purple), and of F_{TA} from atmospheric inversions of Jena81 (red), Jena99 (orange), and CarbonTracker (blue). The trends are relative to the 1961-70 mean for the TRENDY ensemble and Mauna Loa CO₂, and the other time series are offset to have the same mean as the TRENDY ensemble for the last ten years (2003-2012). A 9-year Gaussian smoothing (Harris, 1978) removes inter-annual variability for all time series, and its 1-σ standard deviation is shown for CO₂_{MLO} (green shading). Note that the grey shading here instead indicates 1-σ models' spread, which is generally larger than the standard deviation of TRENDY ensemble's decadal variability. Inset: average seasonal cycles of models' ensemble mean F_{TA} (PgC y⁻¹) for the two periods: 1961-1970 (dashed, lighter grey shade indicates 1-σ model spread) and 2001-2010 (solid, darker grey shade indicates 1-σ model spread), revealing enhanced CO₂ uptake during spring/summer growing season. Mean seasonal cycles global F_{TA} from the atmospheric inversions for 2001-2010 are also shown (same color as the main figure) for comparison. 61

Figure 3-8: Trends for seasonal amplitude of global total net carbon fluxes from S1 (CO₂ only), S2 (CO₂+Climate) and S3 (CO₂+Climate+Land Use/Cover) for each individual TRENDY model. Mauna Loa CO₂ seasonal amplitude is shown for comparison purpose. All amplitude time series are relative to their own 1961-1970 mean amplitude. 63

Figure 3-9: Attribution of the seasonal amplitude trend of global net land carbon flux for the period 1961-2012 to three key factors of CO₂, climate and land use/cover. The red dots represent models' global amplitude increase of F_{TA} from the S3 experiment, and error bars indicate 1-σ standard deviation. The increasing seasonal amplitude of F_{TA} is decomposed into the influence of time varying atmospheric CO₂ (blue), climate (light green), and land use/cover change (gold). Also shown is the trend of Mauna Loa CO₂ seasonal amplitude (thick black line) and its 1-σ standard deviation (grey shade) for the same period. 65

Figure 3-10: Attribution of the seasonal amplitude trend of regional (boreal (50-90N), Northern temperate (23.5-50N), Northern tropics (0-23.5N), Southern tropics (0-23.5S) and Southern extra-tropics (23.5-90S)) net land carbon flux for the period 1961-2012 to three key factors CO₂, climate and land use/cover. The red dots represent models' global amplitude increase of F_{TA} from the S3 experiment. The increasing seasonal amplitude of F_{TA} is decomposed into the influence of time varying atmospheric CO₂ (blue), climate (light green), and land use/cover change (gold). 67

Figure 3-11: Latitudinal contribution of trends for seasonal amplitude of global land-atmosphere carbon flux from TRENDY models in the three sensitivity experiments. Fluxes are summed over each 2.5 ° latitude bands (PgC y⁻¹ per 2.5 ° latitude) before computing the “max-min difference” (refer to Methodology section for definition). For each 2.5 ° latitude band, trend is calculated for the period 1961-2012. 68

Figure 3-12: Contribution from land use/cover change on trends in the seasonal amplitude of global land-atmosphere carbon flux. For each spatial grid, the trend is computed as trends of the “max-min difference” (refer to Methodology section for definition) in the S2 experiment (changing CO₂ and climate) subtracted by trends in S1 (changing CO₂ only)..... 72

Figure 3-13: Relationship between the increase in net biosphere production (NBP, equal to $-F_{TA}$) and increase in NBP seasonal amplitude (as in Figure 4’s red dots), for 1961-2012 period for nine TRENDY models. Error bars indicate the standard errors of the trend estimates. Amplitude increase and associated standard deviation in Mauna Loa CO₂ is plotted in green horizontal line and shade, respectively. Increase in residual land sink is estimated by taking the difference between two residual land sinks, over 2004-2013 and 1960-1969 (an interval of 44 years), as reported in Le Quéré et al. (2015). This difference is then scaled by 52/44 (to make it comparable with models’ NBP change for this figure), which is displayed in black vertical line and shade (error add in quadrature, assuming Gaussian error for the two decadal residual land sinks, then also scaled). The cross-model correlation ($R^2=0.61$, $p < 0.05$) suggests that a model with a larger net carbon sink increase is likely to simulate a higher increase in NBP seasonal amplitude..... 75

Figure 3-S1: Contribution of trends for seasonal amplitude of global land-atmosphere carbon flux for each TRENDY model in the S1 experiment (changing CO₂ only). Trends are calculated for the period 1961-2012 for the “two-month difference” (refer to Methodology section for definition). 79

Figure 3-S2: Similar as Figure 3-S1, but for trends in the S2 experiment (changing CO₂ and climate) subtracting trends in S1, therefore representing effect of climate change with the linear assumption. 80

Figure 3-S3: Similar as Figure 3-S1, but for trends in the S3 experiment (changing CO₂, climate and land use/cover)..... 81

Figure 4-1: Nine-model (excluding IPSL) averaged monthly detrended a). Global mean CO₂ (ppm, column average); b). Global mean CO₂ growth rate (PgC Month⁻¹, using a conversion factor of 1 ppm = 2.12 PgC Month⁻¹); and c). Global total -NBP (PgC Month⁻¹) from 1961 to 2099. Panel d) presents eight-model (excluding IPSL and INM) averaged monthly detrended global mean CO₂ (ppm) at lowest model level and ESRL’s global mean detrended surface CO₂ observation (shown in green). 94

Figure 4-2: Time series of the relative seasonal amplitude (relative to 1961-1970 mean) of a). Global mean atmospheric CO₂; and b). Global total NBP from 1961 to 2099. Thick black line represents multi-model ensemble, and one standard deviation model spread is indicated by light grey shade. 97

Figure 4-3: Seasonal cycle of detrended global mean CO₂ growth rate (a, b), global total -NBP (c, d), global total -NPP (e, f), and global total R_h* (g, h, computed as

NPP minus NBP), averaged over 1961-1970 and 2081-2090 for the CMIP5 models (excluding INM, also excluding IPSL for CO₂ growth rate). Seasonal cycles of individual models are presented in the left panel (dashed for 1961-1970, and solid for 2081-2090). Ensemble mean and one standard deviation model spread (black/grey for 1961-1970, red/pink for 2081-2090) are displayed in the right panels. Blue arrows mark the changes in June and October (NBP maxima and minima), except for CO₂ growth rate and -NPP, where arrows also indicate phase shifts of minima between the two periods. We show -NBP and -NPP so that the negative values represent carbon uptake by the biosphere, and positive values indicate carbon release from the biosphere. Note that -NBP and its two components -NPP and Rh* are not detrended, so that the sum of panels f and h equals to panel d. Detrended -NBP seasonal cycle (not shown) looks very similar to panel d, as its trend is small compared to the magnitude of seasonal cycle. 99

Figure 4-4: Spatial patterns and latitudinal distributions of 10-model mean -NBP (gC m⁻² day⁻¹) changes between 2081-2090 and 1961-1970, during mean a) peak growing season (May-July) and b) dormant season (October-December). Panel c aggregates the spatial patterns in panels a and b zonally, where the black curve corresponds to the -NBP changes in May-July (panel a), and the red curve corresponds to the -NBP changes in October-December (panel b). Further reduction of -NBP in peak growing season—where the black curve falls on the left of the zero line, and increase of -NBP in dormant season—where the red curve is on the right of the zero line, both contribute to amplitude increase. We shade those instances in green, and shade the reversed case (contribute negatively to global total -NBP amplitude increase) in yellow. It is clear that the amplitude increase is dominated by the boreal regions, and by changes in peak growing season. 102

Figure 4-5: Zonal amplitude of NBP from the 10 CMIP5 models (PgC Month⁻¹ per 2° band), averaged over 1961-1970 (black) and 2081-2090 (red). For each model, NBP is first regridded to a 2° × 2° common grid. Monthly zonal totals are then computed for every 2° band, which determine the amplitude (maximum minus minimum) at every band. The Southern Hemisphere has an opposite phase from its northern counterpart, but its magnitude is small due to its small land area. The two subtropical maxima around 10°N and 10-15°S reflect the wet-dry seasonal shift in the Inter-Tropical Convergence Zone (ITCZ) and monsoon movement. They have similar magnitude as the Northern Hemisphere maxima in about a third of the models, however their net contribution to global total NBP seasonal amplitude is small, because they are out of phase and largely cancel each other out. 104

Figure 4-6: Seasonal cycles of global and regional total -NBP, averaged over 1961-1970 (black) and 2081-2090 (red). The last month of the year is repeated. The Northern and Southern subtropics are clearly out of phase and largely cancel each other out. GFDL-ESM2M represents the largest tropical contribution to its global -NBP seasonal cycle (maxima in September and minima in June) of all models, accounting for about a quarter of the amplitude increase. 106

Figure 4-7: Spatial patterns of GFDL-ESM2M $-NBP$ ($gC\ m^{-2}\ day^{-1}$) changes between 2081-2090 and 1961-1970, during mean peak growing season (May-July, first row) and dormant season (October-December, second row) for the esmFdbk2 (first column, constant CO_2 fertilization and changing climate) and esmFixClim2 (second column, constant climate and rising CO_2) experiments. The Northern high latitude regions show mixed response to climate change during peak growing season (panel a), and most of the Northern temperate and boreal regions see enhanced carbon uptake under elevated CO_2 (panel b). Net carbon release is increased both under climate change (panel c) and elevated CO_2 conditions (panel d), however they have different spatial patterns..... 108

Figure 4-8: Same as figure 4-7, but for IPSL-CM5A-LR. Both the carbon uptake in peak growing season and net carbon release in dormant season are clearly dominated by changes in atmospheric CO_2 rather than climate for this model..... 109

Figure 4-9: Relationship between $-NBP$ change and increase of NBP seasonal amplitude, calculated as the differences between 2081-2090 and 1961-1970 for 10 CMIP5 ESMs. The negative cross-model correlation ($R=-0.73$, $p<0.05$) suggests that a model with a larger net carbon sink increase is likely to simulate a higher increase in NBP seasonal amplitude. 111

Figure 4-10: Spatial patterns of $-NBP$ ($gC\ m^{-2}\ day^{-1}$) changes between 2081-2090 and 1961-1970, during peak growing season (May-July mean) for the 10 models.. 113

Figure 4-11: Spatial patterns of $-NBP$ ($gC\ m^{-2}\ day^{-1}$) changes between 2081-2090 and 1961-1970, during dormant season (October-December mean) for the 10 models. 114

Figure 4-12: CO_2 mean seasonal amplitude (ppm) during 2001-2005 and increase in CO_2 seasonal amplitude at Mauna Loa during 1959-2005 ($\% yr^{-1}$, linear trend) from eight CMIP5 models and observation. The big black circle represent surface CO_2 observation at Mauna Loa, Hawaii (19.5°N, 155.6°W; 3400m above sea level). The colored squares represent the 700 hPa (close to the altitude of Mauna Loa station surface) CO_2 output at the original grid that covers Mauna Loa from each of the eight models. Error bars indicate ± 1 standard error in the trend calculation. Compared to the surface observation, only MPI-ESM-LR and GFDL-ESM2M overestimate CO_2 mean seasonal amplitude at Mauna Loa, while the other models underestimate this amplitude. Models split between overestimating and underestimating the CO_2 seasonal amplitude increase at Mauna Loa..... 116

Figure 4-13: CO_2 seasonal amplitude (1951-2100) from eight models (excluding INM and IPSL) at the model grid that covers Mauna Loa, Hawaii (19.5°N, 155.6°W) at 700hPa. The thick black line represents seasonal amplitude of observed Mauna Loa CO_2 records during 1959-2005. All curves are computed by the CCGCRV package. Note that 1951-2005 model data are from esmHistorical, and 2006-2100 data are from esmRCP85..... 117

Figure 4-14: CO₂ mean seasonal amplitude (ppm) during 2001-2005 and increase in CO₂ seasonal amplitude at Pt. Barrow during 1974-2005 (% yr⁻¹, linear trend) from eight CMIP5 ESMs and observation. The big black circle represent surface CO₂ observation at Point Barrow, Alaska (71.3 °N, 156.5 °W; 11m above sea level). The colored squares represent the CO₂ output at lowest model level (four models at 1000 hPa, and four at 925 hPa) at the original grid that covers Point Barrow from each of the eight models. Error bars indicate ±1 standard error in the trend calculation. Compared to the surface observation, only MPI-ESM-LR overestimate the CO₂ mean seasonal amplitude at Point Barrow, while the other models underestimate this amplitude. Models split between overestimating and underestimating the CO₂ seasonal amplitude increase at Point Barrow..... 118

Figure 4-15: CO₂ seasonal amplitude (1951-2100) from 8 models (excluding INM and IPSL) at the model grid that covers Point Barrow, Alaska (71.3N, 156.5W) at lowest level (four models at 1000hPa, and four others at 925hPa). The thick black line represents seasonal amplitude of observed Point Barrow CO₂ records during 1974-2005. All curves are computed by the CCGCRV package. Note that 1951-2005 model data are from esmHistorical, and 2006-2100 data are from esmRCP85..... 119

Figure 4-16: Spatial patterns of soil moisture (cm) changes between 2081-2090 and 1961-1970, during peak growing season (May-July mean) for the 10 models. 121

Figure 4-17: Spatial patterns of soil moisture (cm) changes between 2081-2090 and 1961-1970, during dormant season (October-December mean) for the 10 models.. 122

Figure 4-18: Spatial patterns of near-surface soil temperature (°C) changes between 2081-2090 and 1961-1970, during peak growing season (May-July mean) for the 10 models. 123

Figure 4-19: Spatial patterns of near-surface soil temperature (°C) changes between 2081-2090 and 1961-1970, during dormant season (October-December mean) for the 10 models. 124

Figure 4-20: Changes of tree cover fractions between future (2081-2090) and historical (1961-1970) periods from six CMIP5 ESMs. The values represent fractional cover changes relative to the whole grid cell, instead of relative change of tree cover. For MPI-ESM-LR and INM-CM4, tree fraction has increased over wide areas of the Northern high latitude regions. For MIROC-ESM, tree fraction has generally decreased over the same regions, possibly in response to a hotter and drier climate condition..... 126

Figure 4-21: Changes of natural grass fractions between future (2081-2090) and historical (1961-1970) periods from six CMIP5 ESMs. The values represent fractional cover changes relative to the whole grid cell, instead of relative change of natural grass cover. Notable increase over the Northern high latitude regions is found for BNU-ESM. 127

Figure 4-22: Changes of crop fraction between future (2081-2090) and historical (1961-1970) periods for five CMIP5 ESMs. Except for INM-CM4, the models show similar patterns of crop fraction change, which is expected given they are all driven by the same land cover change scenario. 128

Chapter 1: Introduction

Background

Since 1958, continuous atmospheric measurement at Mauna Loa (MLO), Hawaii (19.5 °N, 155.6 °W, 3400m altitude) has recorded an increase from <320 parts per million (ppm) to over 400 ppm in the mixing ratio of atmospheric CO₂ (Figure 1-1). This increase of ~80 ppm directly corresponds to 170 petagrams (Pg) of additional carbon (using a factor of 2.12 PgC ppm⁻¹ according to Prather et al., 2012)), or 620 Pg of additional CO₂ accumulated (from 1958 to now) in the atmosphere.

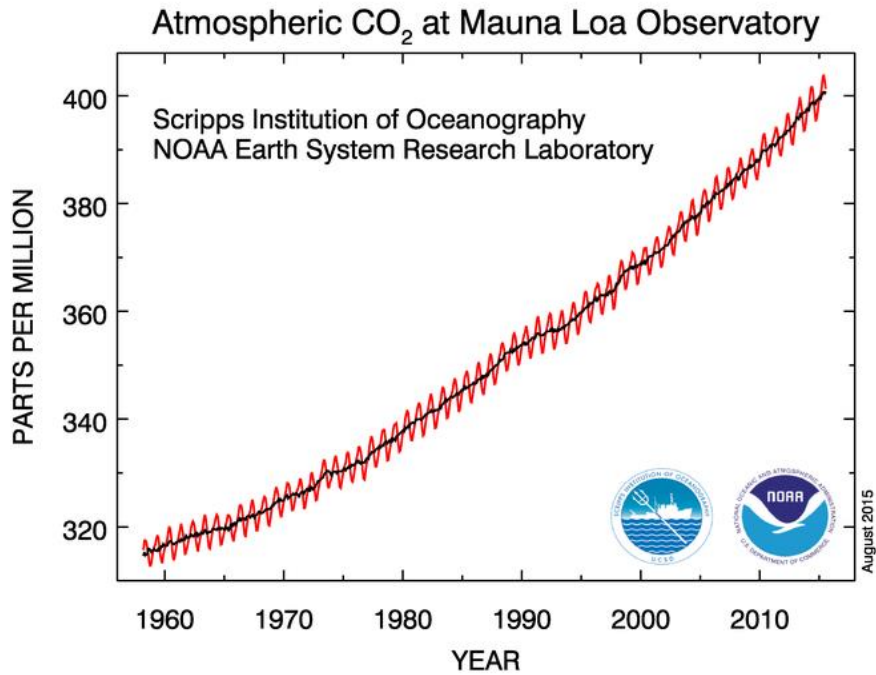


Figure 1-1: Monthly mean atmospheric carbon dioxide at Mauna Loa Observatory, Hawaii from 1958 to 2015 (red curve). The black curve presents the long-term trend, after correction for the average seasonal cycle. (Figure from NOAA/ESRL: www.esrl.noaa.gov/gmd/ccgg/trends/, accessed on Sep 8, 2015)

The atmospheric CO₂ increase is primarily caused by fossil fuel combustion, which had increased from 3.1 PgC y⁻¹ in 1960-1969 to 8.9 PgC y⁻¹ in 2004-2013 (Le Quéré et al., 2015). The carbon release from fossil fuel combustion and land use/cover changes (~1.5 PgC y⁻¹, according to inventory-based estimates) would have caused a rising atmospheric CO₂ twice as fast as observed. Instead, the capacity of ocean and terrestrial ecosystems absorbing CO₂ is also increasing, collectively taking up more than half of the increased CO₂ from fossil fuel combustion and land use/cover changes (Le Quéré et al., 2015). Ocean and land each contributes approximately equally to the carbon sink, which has increased to 2.6±0.5 PgC y⁻¹ and 2.9±0.8 PgC y⁻¹, respectively, over 2004-2013 (Le Quéré et al., 2015). While the ocean carbon sink is estimated from observations and models, the terrestrial carbon sink is estimated from the residual of the other budget terms (Eq 1, Le Quéré et al., 2015):

$$S_{LAND} = E_{FF} + E_{LUC} - (G_{ATM} + S_{OCEAN}) \quad (1)$$

Where E_{FF} is the CO₂ emissions from fossil fuel combustion and cement production, E_{LUC} is the CO₂ emissions resulting from human induced land-use change, G_{ATM} is the growth rate of CO₂ in the atmosphere and S_{OCEAN} is the ocean uptake of CO₂. The size and location of this terrestrial carbon sink remains a major source of uncertainty, and the future projections are not consistent in the sign and magnitude of land-atmosphere carbon fluxes (Friedlingstein et al., 2013).

In addition to the long-term increase, the atmospheric CO₂ record also shows a prominent seasonal cycle (Figure 1-1, red curve) with peak-to-trough amplitude of 6.5 ppm. The seasonal cycle is characterized with a 5-month decrease (minimum in

October) and a 7-month increase (maximum in May), mostly attributed to the growth and decay of plants in Northern Hemisphere (NH) (Heimann, 1986). In an early study investigating the trend of MLO CO₂ over 1958–1972, Hall et al. (1975) found no evidence of long-term amplitude change. However, a few years later, rapid increase in MLO CO₂ amplitude was observed (Pearman and Hyson, 1981; Cleveland et al., 1983; Bacastow et al., 1985). This increasing trend of MLO CO₂ amplitude was 20% for 1964-1994 (Keeling et al., 1996), but declined considerably in the following decade (Buermanm et al., 2007). Updated estimates (Graven et al., 2013; Zeng et al., 2014) put the trend at 15% for 1961-2010, slightly lower than the number given by Keeling et al. (1996) 20 years ago, which is consistent with the declining trend of the CO₂ seasonal amplitude derived from space-borne measurements (Schneising et al., 2014). Four decades of CO₂ observations at a high latitude site—Point Barrow, Alaska (71.3 N, 156.6 W, 11m altitude) generally exhibited similar decadal variability, but with two fold increasing trend compared with MLO record. Overall, the evolution of MLO CO₂ amplitude during 1958-2015 can be described as a relatively steady long-term increase, modulated by decadal variations.

Whether the CO₂ amplitude will increase or decrease in the future is an open question. Both rising temperature and increasing CO₂ may result in elevated CO₂ amplitude in response to stimulated ecosystem activities. In contrast, the increasing frequency, intensity and/or duration of heat waves, drought and flood (IPCC, 2013) may reduce the ecosystem productivity and thus the CO₂ seasonal amplitude. As an important indicator of terrestrial ecosystem activity, the seasonal cycle of MLO CO₂ observation will be closely monitored to provide more valuable data in future.

However, to make reasonable projections on how its amplitude will change in the future, it is crucial to better understand the underlying mechanisms for its amplitude increase in the past.

Causes of historical CO₂ seasonal amplitude increase

Using observational evidence and modeling simulations, many scientists have studied the causes of historical CO₂ seasonal amplitude increase. Changes in ecosystem productivity and respiration directly influence the CO₂ seasonal amplitude, as the atmospheric CO₂ seasonal cycle is closely tied to ecosystem activities (Randerson et al., 1997). Earlier studies have speculated on decreasing global primary production in response to global changes (such as acid rain and deforestation) (Reiners, 1973; Whittaker and Likens, 1973). However, no decreasing trend of CO₂ amplitude was observed, probably because the biosphere was too big to be affected or the degradation of biosphere was balanced by enhanced ecosystem productivity (Hall et al., 1975). These complex interactions are controlled by several factors including CO₂ fertilization effect, climate change and land use change.

The CO₂ fertilization effect

One of the earliest suggestions was that increase in the CO₂ concentration would function similar to fertilizer (thus the term “CO₂ fertilization”), enhancing metabolic activity of the land biota, and therefore increasing the CO₂ seasonal amplitude (Bacastow et al., 1985). This idea has been supported by several in situ experiments, where an increased plant growth was observed under higher-than-

normal CO₂ concentrations (Wulff and Strain, 1982; Grifford, 1977). Similarly, numerous other studies extensively have discussed the various CO₂ fertilization mechanisms including increased photosynthesis and suppressed photorespiration (Bazzaz, 1990), improved efficiency in water (Field et al., 1995) and nutrients use (Drake et al., 1997), and reduced sensitivity to drought (Korner, 2000). Free Air CO₂ Enrichment (FACE) experiments also suggested enhanced forest ecosystem productivity under higher partial pressure of CO₂ (Ainsworth and Long, 2005; DeLucia et al., 2005). Even though, all this evidence is consistent in some aspect, the response of individual species would often change drastically at the community level (Bazzaz, 1990), or with different experiment design (Klironomos et al., 2005), and field/model studies on plant communities were inconclusive (Curtis et al., 1989; Oechel et al., 1994).

Nitrogen (Reich and Hobbie 2013; Sillen and Dieleman 2012) and phosphorus (Vitousek et al., 2010), as mostly discussed, could significantly limit the CO₂ fertilization effect in actual ecosystems compared to those under controlled experiments. Observational evidence, such as data from International Tree ring Data Bank (ITRDB), suggested that CO₂ fertilization affects only about 20 percent of sites globally (Gedalof and Berg, 2010). Little biomass stimulation was observed under elevated CO₂ when nitrogen or phosphorus and water were limited in three long-term (>5 years) open air CO₂ × N experiments (Schneider et al., 2004; Dukes et al., 2005; Reich et al., 2006). Overall, the effect of CO₂ fertilization at the global scale remains inconclusive, but according to some observational and modeling evidences, it should

explain no more than 25% of the observed amplitude increase (Kohlmaier et al., 1989).

Climate change impact

Keeling et al. (1996) observed a close relationship between annually averaged land surface temperature and CO₂ amplitude change, with the CO₂ amplitude peak lagging two years behind the temperature peak, at several sites including MLO. This high CO₂ sensitivity to temperature could not be explained by short-term photosynthesis response, which is typically a 40-100% increase for every 10 °C increase in temperature (Larcher, 1984). They also observed a phase advance of about one week during the declining phase of the cycle, suggesting a lengthening of the growing season, but reasons were not provided for the long-term CO₂ amplitude increase. Nevertheless, their study inspired a follow-up work by Myneni et al. (1997) which showed an increase in the seasonal amplitude of satellite-derived normalized difference vegetation index (NDVI) during 1981-1991, especially at 45-70 °N, associated with the lengthening of growing season. However, lengthening of growing season does not necessarily mean a higher peak ecosystem productivity (Baptist et al., 2010). Earlier spring may even decrease peak summer productivity with soil moisture deficiency in peak summer (Buermann et al., 2013). Many other climate-related changes, including invasive species and community shifts are part of the complicated ecosystem responses to climate change (Walther et al., 2002) that may have led to the observed temperature-CO₂ seasonal amplitude relationship.

Such relationship did not persist in the decade following the discovery by Keeling et al. (1996). As displayed in Figure 1-2, Buermann et al. (2007) found that

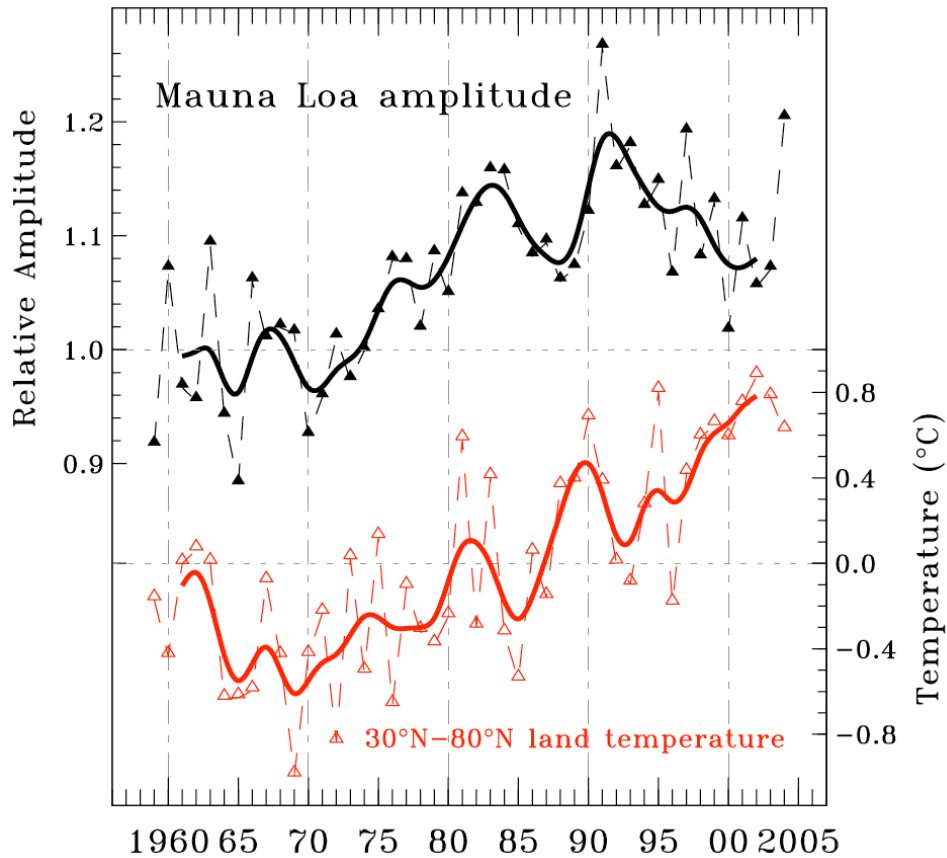


Figure 1-2: Time series of the relative amplitude of the seasonal cycle of atmospheric CO₂ at the MLO (black) and anomalies in observed annual land temperatures (red) for the latitudinal band from 30°N to 80°N (except Greenland). The relative amplitudes are in respect to the mean amplitude of the first 5 year of CO₂ record (1959–1963). Temperature anomalies are relative to the 1959–2004 study period (Buermann et al., 2007).

despite the increase in land temperature after 1994, CO₂ amplitude at MLO decreased. This decline was attributed to reduction in carbon sequestration over North America (due to drought during 1998–2003), and a shift in atmospheric circulation

patterns. On the other hand, by comparing recently available aircraft observations with earlier data from 1958-1961, Graven et al. (2013) found that the CO₂ seasonal amplitude at altitudes of 3 to 6 km had increased by 50% for 45-90°N, substantially higher than the rate observed at MLO and Point Barrow. This magnitude of CO₂ amplitude increase implied a rise of 30 to 60% in the carbon fluxes from northern extratropical land ecosystems, especially the boreal forests, a change that was significantly underrepresented in the terrestrial ecosystem models participating in the fifth phase of the Coupled Model Intercomparison Project (CMIP5) (Figure 1-3). They suggested that climate change may have shifted ecosystem age and species composition, which could be responsible to the CO₂ amplitude increase (Graven et al., 2013).

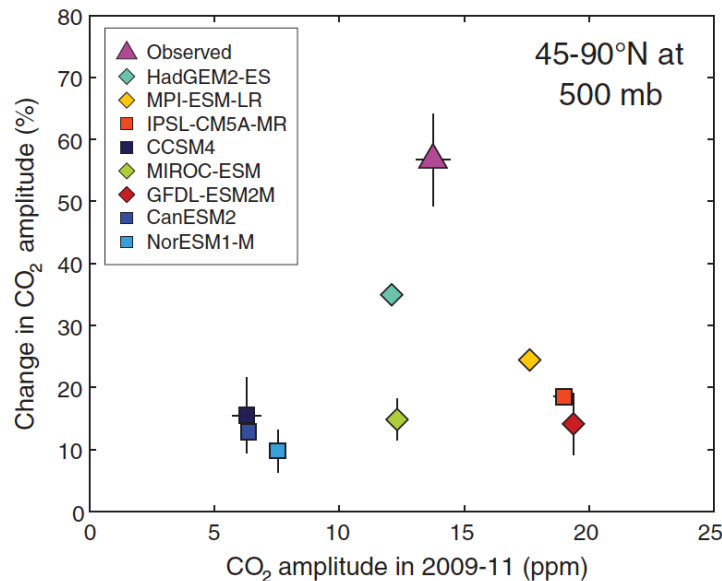


Figure 1-3: Change in amplitude of the seasonal cycle of CO₂ between 1958 to 1961 and 2009 to 2011 versus amplitude of the seasonal cycle for 2009 to 2011 at 500 mb, averaged over 45° to 90°N, in observations and in simulations of the CMIP5 land models (Graven et al., 2013).

Land use/cover change

Even though, the role of land use/cover change in altering the terrestrial ecosystem has been extensively studied, its impact on CO₂ seasonal amplitude was largely overlooked. Only a few studies (Hall et al., 1975; McGuire et al., 2001) briefly discussed this particular issue. Changes in land cover (i.e., deforestation and forest regrowth) can alter the seasonal cycle of carbon flux, due to different ecosystem productivities of old and new ecosystems. Furthermore, sudden carbon release during the conversion processes (i.e., slash and burn) can strongly affect the seasonal carbon cycle. Similarly, even without changing the land cover, advancement in agricultural technology (irrigation, fertilizers, and crop varieties with high yield/resistance) and different land management practices can strongly impact the crop productivity and also the seasonal carbon cycle. In the last fifty years, the global agricultural production has tripled, an incredible achievement that is largely due to improved farming practices. Compared to natural systems, crops have a short growing season, and in some cases a larger seasonal amplitude compared to nearby natural vegetation (Miles et al., 2012). It is possible for crops to have a significant impact on the seasonal cycle of carbon flux, especially in the mid-latitude regions (world's major crop belt).

Priority Questions Regarding CO₂ amplitude increase

1. Is the observed CO₂ amplitude increase sufficiently explained by the effects of CO₂ fertilization and climate change? Could agriculture intensification significantly alter the observed atmospheric CO₂ seasonal cycle?

2. Can the latest generation of terrestrial ecosystem models capture the seasonal characteristics of global carbon cycle? How important are the different controlling factors according to the models?

3. Will the atmospheric CO₂ amplitude—indicator of terrestrial ecosystem activities—continues to increase in the future? How reliable are the model projections?

Objectives

1. To investigate if agricultural intensification would cause increase in CO₂ amplitude, the mechanisms and latitudinal patterns, and its strength relative to other factors.

2. To evaluate the simulation of the seasonal cycle of global carbon flux spatially and temporally with latest generation of dynamic vegetation models, and to attribute relative contributions of different factors in the model simulated amplitude change of land-atmosphere carbon flux.

3. To explore the future projection of CO₂ amplitude change using fully coupled earth system models, and to understand the main contributors (ecosystem production or respiration, main regions of contribution) that lead to the projections.

The Dissertation and its Organization

Chapter 1 (this chapter) introduced the background of the long-term increase in atmospheric CO₂ concentration measured at MLO; the global carbon budget; and the decadal variation and long-term trend of the atmospheric CO₂ seasonal amplitude

increase. Then a short overview is presented on some of the major causes (CO₂ fertilization, climate change and land use/cover change) of the observed amplitude increase in atmospheric CO₂.

Chapter 2 describes an initial modeling attempt to capture the first-order effect of agricultural intensification on the global carbon cycle. The rationale regarding why agricultural intensification can impact the CO₂ seasonal cycle will be explained. Simulated changes in the phase and amplitude of global total land-to-the-atmosphere carbon flux will also be discussed. This will be followed by the temporal and spatial patterns of the carbon flux, contributions of natural vegetation versus cropland at different latitudes, and the magnitude of land use/cover contribution relative to CO₂ fertilization and climate change.

Chapter 3 expands the investigation of model simulated amplitude increase of terrestrial carbon flux to eight other terrestrial ecosystem models, under the same experiment protocol. The model simulations of net carbon flux will be carefully evaluated against observation-based datasets on global and regional seasonal cycle. Then the relative contributions from CO₂ fertilization, climate and land use/cover change will be quantified globally and regionally. In addition, the spatial attribution of the factorial experiment results will be examined with a new “two-month difference” method.

Chapter 4 extends the interest towards future projection of CO₂ amplitude increase, analyzing simulation results from fully coupled models contributing to the Intergovernmental Panel on Climate Change (IPCC) Fifth Assessment Report. We will explore the close relationship between the seasonal cycle of CO₂ and net

terrestrial carbon flux, and the seasonal cycle of the latter will be separated into net primary production (NPP) and respiration. The spatial patterns of carbon flux from individual models and the multi-model mean will also be presented and analyzed for the main contributing region.

Finally, Chapter 5 presents conclusions and scientific significance of the results presented in previous chapters. The dissertation concludes with discussions of future research directions.

Chapter 2: The agricultural Green Revolution as a driver of the increasing atmospheric CO₂ seasonal amplitude

Preface

Ning Zeng¹, Fang Zhao¹, George J. Collatz², Eugenia Kalnay¹, Ross J. Salawitch¹,
Tristram O. West³, Luis Guanter⁴

¹Department of Atmospheric and Oceanic Science and Earth System Science
Interdisciplinary Center, University of Maryland, USA

²Hydrospheric and Biospheric Sciences, NASA Goddard Space Flight Center, USA

³Joint Global Change Research Institute, Pacific Northwest National Laboratory,
USA

⁴Institute for Space Sciences, Freie Universität Berlin, Germany

Published in:

Nature (2014) 515, 394-397

Abstract

A long-standing puzzle in the global carbon cycle is the increase in the amplitude of the seasonal cycle of atmospheric CO₂ (Bacastow et al., 1985; Keeling et al., 1996). This increase likely reflects enhanced biological activity in the Northern Hemisphere (NH). It has been hypothesized that vegetation growth may have been stimulated by higher concentrations of CO₂ as well as warming in recent decades, but the role of such specific mechanisms has not been quantified and they have been

unable to explain the full range and magnitude of observations. Here we suggest another potential driver of the increased seasonal amplitude: the intensification of agriculture from the Green Revolution that led to a 3-fold increase in world crop production over the last 5 decades. Our analysis of CO₂ data and atmospheric inversions shows a robust 15% long-term increase in CO₂ seasonal amplitude from 1961 to 2010 that is punctuated by large decadal and interannual variations. The three pillars of the Green Revolution, consisting of high yield cultivars, fertilizer use, and irrigation, are represented in a terrestrial carbon cycle model. The results reveal that the long-term increase in CO₂ seasonal amplitude arises from two major regions: the mid-latitude cropland between 25N-60N and the high-latitude natural vegetation between 50N-70N. The long-term trend of seasonal amplitude is 0.3% per year, of which sensitivity experiments attribute 43% to land use change, 31% to climate variability and change, and 26% to CO₂ fertilization. The recent decade 2001-2010 has an earlier vegetation growth (by 1-2 weeks) and a deeper maximum drawdown of CO₂ in July (by 5 PgC y⁻¹), compared to the early decade 1961-70, suggesting human land use and management is a key driver in the changing seasonal 'breathing' of the biosphere.

Introduction

Superimposed on the continued increase in the atmospheric CO₂ concentration is a prominent seasonal cycle with peak-to-trough amplitude of about 6 ppm (Tans, P. P. & Keeling, 2013). This cycle arises mostly from the seasonal imbalance of growth and decay of the Northern Hemisphere (NH) biosphere as vegetation takes up CO₂

during the boreal spring and summer growing season and releases CO₂ back into the atmosphere throughout the year (Bacastow et al., 1985; Tucker et al., 1986; Keeling et al., 1996). The CO₂ seasonal amplitude has increased over time, suggesting an increase in NH biosphere activity (Heimann, 1986; Keeling et al., 1996; Randerson et al., 1997). Early work suggested enhanced vegetation growth due to stronger fertilization at higher level of CO₂, but the observed amplitude increase would require an unrealistically large CO₂ fertilization effect (Kohlmaier et al., 1989). Another tantalizing possibility is the enhanced vegetation growth or the ‘greening’ of the high latitude regions in response to warming over the last few decades that has resulted in a lengthening of the growing season (Keeling et al., 1996; Myneni et al., 1997; Buermann et al., 2007). Despite of their plausibility and the apparent correlation between the rising CO₂/temperature and the increasing CO₂ seasonal amplitude, such possibilities could not be quantitatively verified in comprehensive carbon cycle models (Kohlmaier et al., 1989; McGuire et al., 2001). For instance, while a strong CO₂ fertilization effect can produce a large seasonal amplitude change in some models, the required increases in productivity and mean carbon sink are not consistent with other observational constraints (Randerson et al., 1997; Cadule et al., 2010; Piao et al., 2013). Here we suggest that human land use and management have modified the seasonal characteristics of the global carbon cycle, and is a ‘missing link’ to the puzzle of increasing CO₂ seasonal amplitude.

In a 50-year time span from 1961 to 2010, the world population more than doubled, from 3 to 7 billion, while crop production tripled, from 0.5 to 1.5 PgC y⁻¹ (Petagram carbon per year; Figure 2-1). It is striking that the 3-fold increase in crop

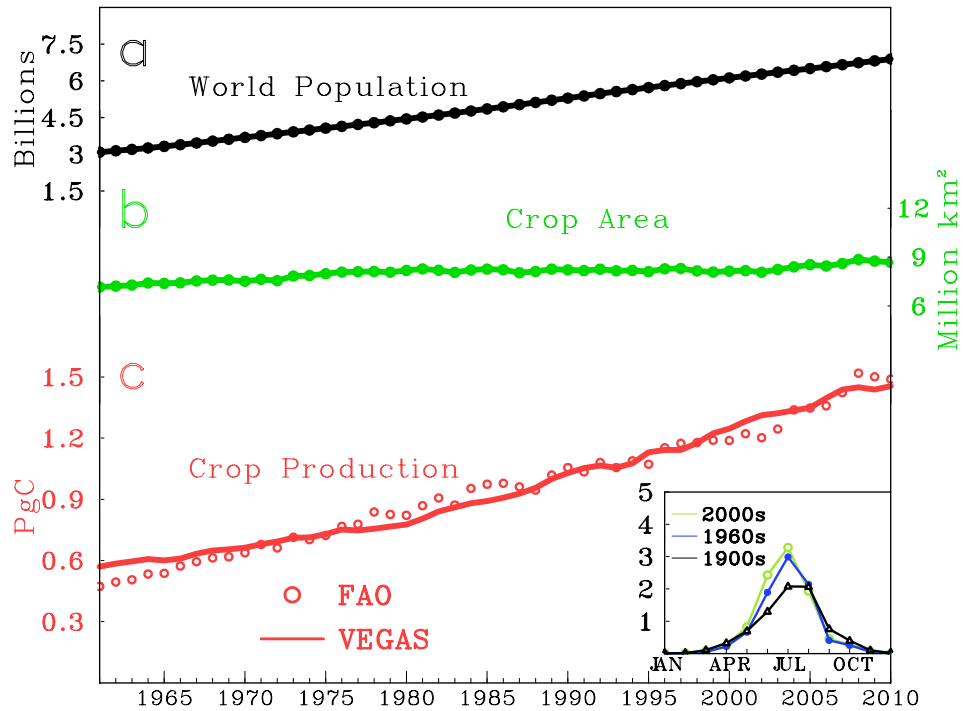


Figure 2-1: Changing world population (billions), cropland area (million kilometer squared) and annual crop production (PgC) during 1961-2010. Crop production tripled to support 2.5 times more people on only 20% more cropland area, enabled by the agricultural Green Revolution. Plotted in (c) is the VEGAS model simulated crop production, compared to estimate from FAO statistics. The inset in (c) shows modeled GPP for three periods 1901-10, 1961-70, and 2001-10 for a location in the US Midwest agricultural belt (98W, -40N) that was initially naturally vegetated and later converted to cropland. The change in seasonal characteristics from these transitions may have contributed to the change in atmospheric CO₂ seasonal amplitude.

production was accompanied by a mere 20% increase in the land area of major crops from 7.2 to 8.7 million km² (Table 2-1). Higher crop production is thus due mostly to greater yield per unit area, an extraordinary technological feat often termed the agricultural Green Revolution. The higher yield can be attributed to three major factors: high yield crop varieties such as hybrid dwarf rice and semi-dwarf wheat, use of fertilizer and pesticide, and widespread use of irrigation (Jain, 2010).

Table 2-1: Summary of changes in population, cropland area, and crop production from 1961 to 2010 from FAO data and other statistics, and Harvest Index (HI), Management Intensity (MI) and NPP_{crop} from the VEGAS model. Crop production is harvested edible parts of crops, while NPP_{crop} is total biomass production including above and below-ground biomass. Harvest Index (HI) is grain and above-ground biomass ratio. All are measured in terms of carbon mass, which is typically about 50% of plant dry mass. Model results are in parentheses.

	Population (billions)	Cropland area (million km ²)	Crop production (PgC y ⁻¹)	Harvest Index (HI)	Management Intensity (MI, relative to 2000)	Total production on cropland (NPP_{crop} , PgC y ⁻¹)
1961	3	7.2	0.5 (0.6)	(0.31)	(0.9)	(4.0)
2010	7	8.7	1.5 (1.4)	(0.49)	(1.03)	(6.2)
Change 2010-1961	4	1.5	1.0 (0.8)	(0.18)	(0.13)	(2.2)
Percent change 2010-1961	130%	20%	200% (130%)	(60%)	(12%)	(55%)

The plausibility of a potential Green Revolution impact on the CO₂ seasonal cycle follows from a ‘back-of-envelope’ estimate. The global total terrestrial biosphere Net Primary Productivity (NPP) is about 60 PgC y⁻¹, and the seasonal variation from peak to trough is between 30-60 PgC y⁻¹ (Cramer et al., 1999). Of the 60 PgC y⁻¹ in NPP, about 6 PgC y⁻¹, or 10% is associated with crop production as the human appropriated NPP (Vitousek et al., 1986; Imhoff et al., 2004; Haberl et al., 2007). Assuming a doubling in crop NPP, i.e., 3 PgC y⁻¹ increase, this leads to an increase of global NPP by 5-10% (3 divided by 60 or 30). This rate is substantial compared to the increase in CO₂ seasonal amplitude (Randerson et al., 1997).

We studied this hypothesis by analyzing a variety of observational data and model output, including the Mauna Loa (MLO) CO₂ record from 1958 and a global total CO₂ index from 1981 (Tans, P. P. & Keeling, 2013), and atmospheric inversions

Jena81 and Jena99 (Rodenbeck et al., 2003) and the CarbonTracker (Peters et al., 2007). Another key tool is the terrestrial carbon cycle model VEGAS (Zeng, 2003; Zeng et al., 2005a) which, in a first such attempt, represents the increase in crop Gross Primary Productivity (GPP) by changes in crop management intensity (MI) and Harvest Index (HI, ratio of grain and total aboveground biomass). Seasonal amplitude is calculated using a standard tool CCGCRV (Thoning et al., 1989). Details are described in Methods.

Results and Discussion

Mean seasonal cycle

The VEGAS model was run from 1701 to 2010, forced by observed climate, annual mean CO₂ and land use and management history. The model simulates an increase in crop production from 0.6 PgC y⁻¹ in 1961 to 1.4 PgC y⁻¹ in 2010, a 0.8 PgC y⁻¹ increase, slightly smaller than the FAO statistics of 1 PgC y⁻¹ (Figure 2-1). The net terrestrial carbon flux to the atmosphere (F_{TA}) has a minimum in July, corresponding to the highest rate of vegetation growth and carbon uptake (Figure 2-2 inset). The maximum of F_{TA} occurs in October when growth diminishes yet the temperature is still sufficiently warm for high rates of decomposition in the NH. The model simulated seasonal cycle of F_{TA}, in both amplitude and phasing, is within the range of uncertainty from the atmospheric inversions (Figure 2-3).

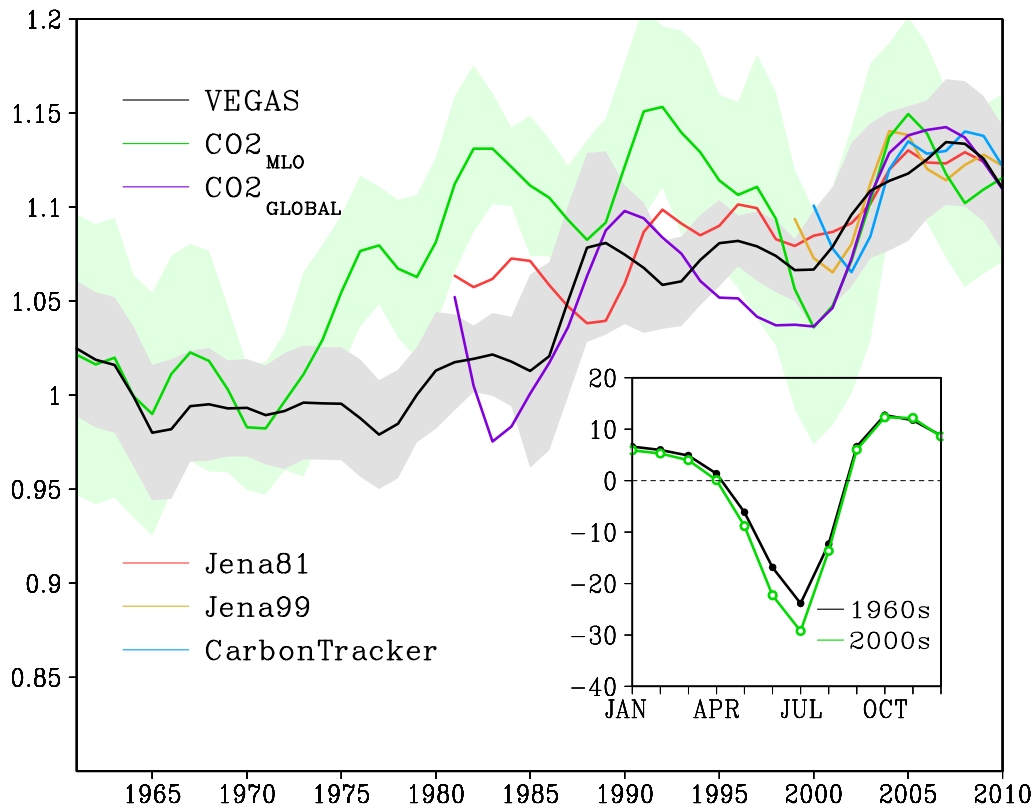


Figure 2-2: Temporal evolution of seasonal amplitude. Trends for VEGAS simulated land-atmosphere carbon flux F_{TA} (black), of MLO CO_2 mixing ratio (CO_2^{MLO} , green) and global CO_2 mixing ratio (CO_2^{GLOBAL} , purple), and F_{TA} from atmospheric inversions of Jena81 (red), Jena99 (brown), and CarbonTracker (blue). Changes are relative to the 1961-70 mean for VEGAS and the other time series are offset to have the same mean for 2001-2010. Seasonal amplitude is calculated as the difference between the maximum and the minimum of each year after detrending and band pass filtering with a standard tool CCGCRV (Extended Data Fig. 3). A 7-year bandpass smoothing removes interannual variability whose 1- σ standard deviation is shown for CO_2^{MLO} (green shading) and VEGAS F_{TA} (grey shading). Inset: average seasonal cycle of VEGAS F_{TA} ($PgC\ y^{-1}$) for the two periods 1961-70 and 2001-10, showing enhanced CO_2 uptake during spring/summer growing season.

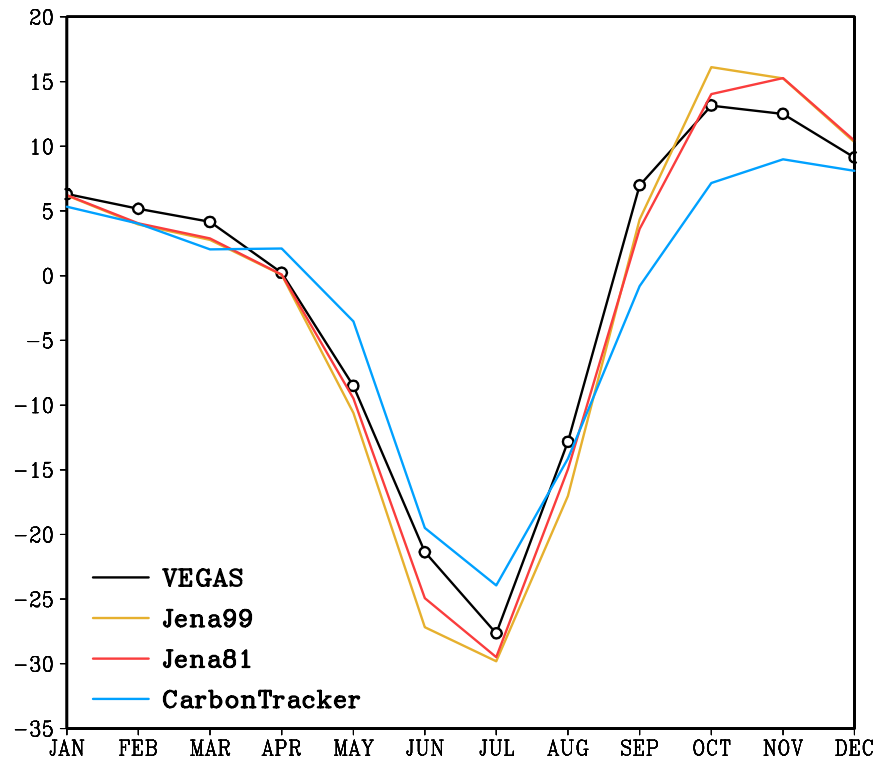


Figure 2-3: Average seasonal cycle of land-atmosphere carbon flux. F_{TA} (in PgC y^{-1}) for the period 2001-2010 from VEGAS model, compared to atmospheric inversions of Jena81, Jena99, and CarbonTracker.

In the decade of 1961-1970, the average seasonal amplitude of F_{TA} is 36.6 PgC y^{-1} . It increased to 41.6 PgC y^{-1} during 2001-2010 (Figure 2-2 inset). This amplitude increase appears mostly as an earlier and deeper drawdown during the spring-summer growing season. Using -15 PgC y^{-1} , the mid-point of F_{TA} drawdown as a threshold, we find that the growing season has lengthened by 14 days, with spring uptake 10 days earlier. The annual mean F_{TA} is -1.6 PgC y^{-1} for 2001-2010, implying a net sink whose value is within the uncertainty range from global carbon budget analysis (Le Quéré et al., 2013). This mean sink increased over the period,

suggesting a relation between seasonal amplitude and the mean sink (Randerson et al., 1997).

Temporal evolution

The temporal evolution of the seasonal amplitude of F_{TA} exhibits a long-term rise of 15% over 50 years, or 0.3% per year (Figure 2-2 and Table 2-2; also see Figure 2-4 for the detrended monthly time series). There are large decadal and interannual variabilities. Mauna Loa CO_2 mixing ratio (CO_{2MLO}) shows a similar

Table 2-2: The trend of CO_2 seasonal amplitude change from three model sensitivity experiments. Each experiment has only a single forcing of climate (CLIM) or CO_2 (CO_2) or land use and management (LU) change. Their percentage contributions are in parenthesis and the total is SUM. Additionally, the experiment ALL is the simulation with all three forcings as in Figures 2-2 and 2-3. The trend is calculated with a least-square linear fit of the unsmoothed time series of seasonal amplitude of modeled land-atmosphere carbon flux F_{TA} , and may be somewhat different from a visual inspection of Figure 2-2 where the data has been smoothed to remove interannual variability.

	CLIM	CO ₂	LU	SUM	ALL
1961-2010 trend (% per year)	0.088	0.076	0.135	0.299	0.319
Percentage contribution to SUM	29%	26%	45%	100%	

overall trend but only resemblance to VEGAS on decadal time scales. Most noticeably, a rise in CO_{2MLO} during 1975-85 precedes a similar rise in VEGAS by several years. This rise was a focus of earlier research (Kohlmaier et al., 1989; Keeling et al., 1996). A major caveat is that Mauna Loa CO_2 is not directly

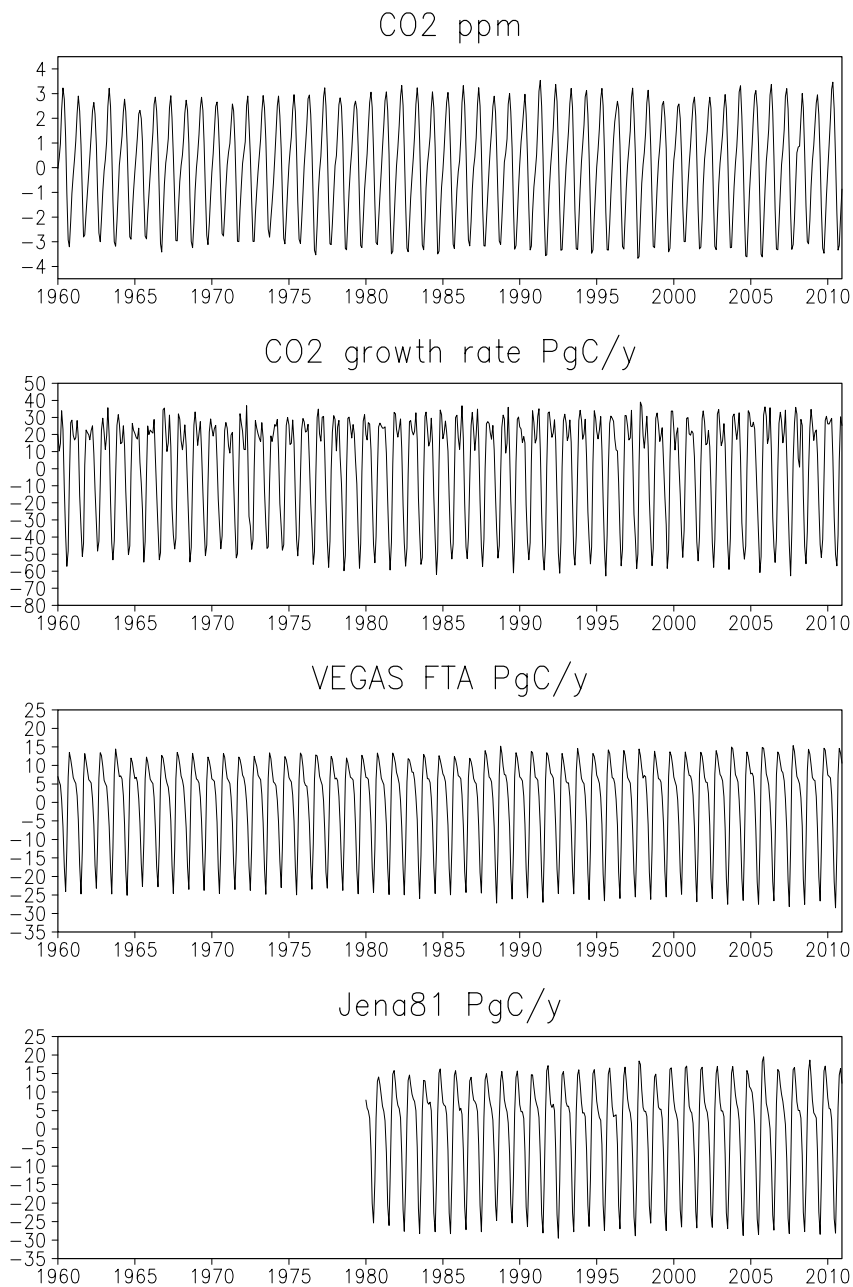


Figure 2-4: Time series analysis for seasonal cycles. (a) MLO CO₂; (b) MLO CO₂ growth rate (dCO_2/dt); (c) Net land-atmosphere carbon flux (F_{TA}) from VEGAS; (d) Net land-atmosphere carbon flux from the atmospheric inversion of Jena81. Trends and high frequency variations have been removed following Thoning et al. (1989)²³. Seasonal amplitude in Figures 2-3 is calculated as the difference between maximum and minimum of each year.

comparable with modeled F_{TA} because this single station is also influenced by atmospheric circulation, as well as fossil fuel emissions and ocean-atmosphere fluxes. The comparison is nonetheless valuable because MLO is the only long-term record and is generally considered representative of global mean CO_2 (Heimann, 1986).

We also include in our comparison a global total CO_2 index ($CO_{2GLOBAL}$) and F_{TA} from three atmospheric inversions. The seasonal amplitude of $CO_{2GLOBAL}$, Jena81 and VEGAS are similar but with some differences in the early 1980s (Figure 2-2). Otherwise they are similar to VEGAS, supporting above interpretation of local influence in MLO CO_2 (Buermann et al., 2007). In contrast, if only considering the period since 1981, MLO CO_2 shows little trend because much of the increase occurred earlier in the 1970s. A decrease in seasonal amplitude in the late 1990s are seen in all data, possibly due to drought in the NH midlatitude regions (Zeng et al., 2005b; Buermann et al., 2007). Similarly, there is consistency in the rapid increase in the first few years of the 21st century. In our view, the change in the seasonal CO_2 amplitude is best characterized as relatively steady long-term increase, modulated by decadal variations, though the appearance can alternatively be viewed as periods of slow changes or even slight decreases punctuated by large episodic increases.

Spatial pattern

We further analyze the spatial patterns underlying the seasonal amplitude of land-atmosphere carbon flux. The latitudinal distribution of seasonal amplitude of F_{TA} (Figure 2-5) shows major contribution from NH mid-high latitude regions 30N-70N, primarily driven by the large seasonal temperature variations there. The two

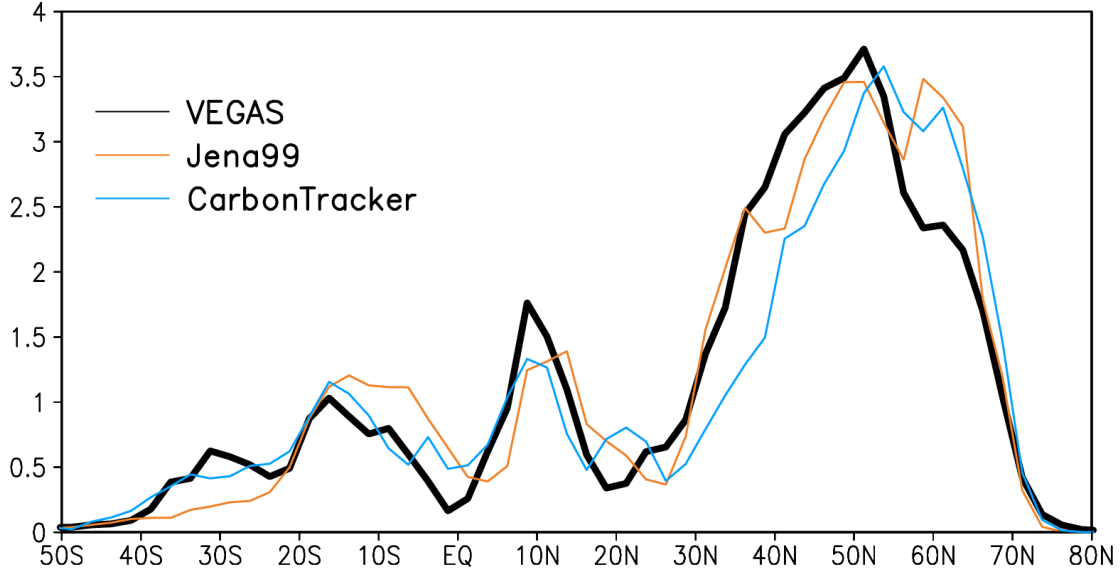


Figure 2-5: Latitude dependence of the seasonal amplitude of land-atmosphere carbon flux. Fluxes are summed over latitude bands for the VEGAS model and from two atmospheric CO₂ inversions Jena99 and the CarbonTracker. Northern Hemisphere (NH) mid-high latitude region, driven by winter-summer temperature contrast, is the main contributor. The Southern Hemisphere has opposite phase from the NH, but its contribution to global total is small due to its small land area. The two subtropical maxima around 10N and 10S are due to the wet-dry seasonal shift in the Inter-Tropical Convergence Zone (ITCZ) and monsoon movement that are out of phase and largely cancel each other out in terms of their net contribution to global total F_{ta} seasonal amplitude. The results are resampled into 2.5° latitude bands and the unit is PgC y⁻¹ per 2.5° latitude from the original resolutions of 0.5°×0.5° for VEGAS, 5.0°×5.0° for Jena99 and 1.0°×1.0° for CarbonTracker.

subtropical zones centered at 10N and 10S have smaller but distinct seasonal cycles caused by the subtropical wet-dry monsoon-style rainfall changes. The Southern Hemisphere (SH) between 40S-25S has a clear seasonal cycle with opposite sign of NH, but it is much smaller due to less landmass. The atmospheric inversions also depict these broad features, in particular, the major peak in the NH. VEGAS overestimates the seasonal amplitude between 30N-45N compared to both inversions.

Because of seasonal phase differences even within the same hemisphere, the latitudinal distribution does not automatically add up to the global total in Figure 2-2 inset, in particular, SH partially cancels out the NH signal.

Natural vegetation vs. cropland

Next we examine the relative contributions of natural vegetation vs. cropland in driving the rising seasonal amplitude of F_{TA} . We conducted a similar latitudinal analysis of modeled F_{TA} but separated cropland from natural vegetation, using a

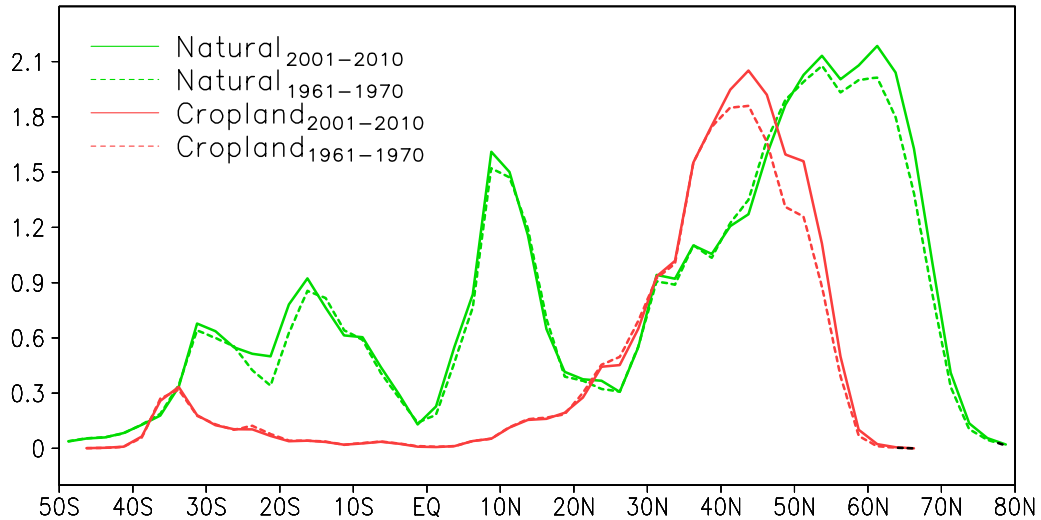


Figure 2-6: Latitudinal distribution of the seasonal amplitude of land-atmosphere carbon flux. Calculated separately for natural vegetation (green lines) and cropland (red lines), for the averages of two periods 1961-1970 (dashed) and 2001-2010 (solid). Unit: PgC y^{-1} per 2.5 degree latitude.

cropland mask for year 2000. Results are shown in Figure 2-6. While the seasonal cycle is dominated by natural vegetation at high latitude, cropland is important in the latitude bands 25N-60N, encompassing the world's major agricultural lands of Asia,

Europe and North America. Between 35N and 45N, the seasonal amplitude of F_{TA} on cropland is even higher than natural vegetation. In the SH, there is some contribution from cropland between 20S-40S. A confounding factor is the contemporaneous change in cropland area. However, a sensitivity experiment conducted using the cropland mask of 1961 yielded similar results.

The seasonal amplitude increase between the two time periods 1961-70 and 2001-10 is clear both in the naturally vegetated area and cropland area (Figure 2-6). Over cropland, seasonal amplitude increased nearly everywhere, while major increase occurred in NH natural vegetation between 50N and 70N. Because the model is forced by the three factors: climate, CO_2 and land use changes, the seasonal amplitude increase in natural vegetation can only come from climate and CO_2 . Between 25N-50N, there is little amplitude change from natural vegetation, suggesting the combined effect of climate and CO_2 is small there. This can arise from two possibilities: either both effects are small, or climate and CO_2 have opposite impacts that more or less cancel each other out. Because CO_2 fertilization likely enhances NPP and therefore CO_2 amplitude (Kohlmaier et al., 1989), changes in climate may have had a negative impact on the mid-latitude natural vegetation. In contrast, the large F_{TA} seasonal amplitude change seen in cropland area between 35N and 55N suggests that land use is responsible there, assuming that crop responds to the combined effect of climate and CO_2 in a way similar to natural vegetation in the same climatic zone. The spatial pattern of NPP trend (Figure 2-7) shows largest increase in NH agricultural belts of North America, Europe and Asia, supports the above interpretation on a key role from the intensification of agriculture.

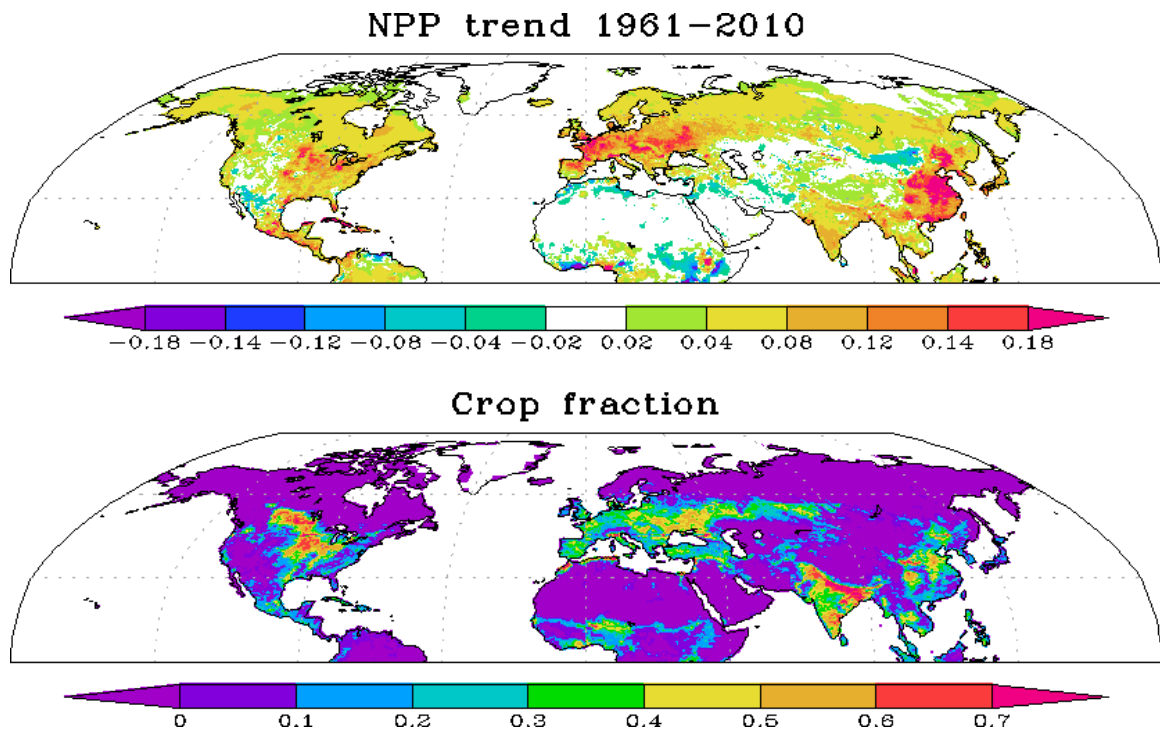


Figure 2-7: Modeled linear trends (kgC m^{-2} over 50 years, upper panel) from 1961 to 2010 show major increases in agricultural areas of North America, Europe and Asia (lower panel: crop fraction in 2000). There are also wide spread increases in much of Northern Hemisphere especially the high latitude regions in response to warming and CO_2 fertilization effect. Together, they are mostly responsible for the increase in F_{TA} and CO_2 seasonal amplitude. Decreases in some regions are due to climate trends.

It may seem surprising that cropland can have such a large impact, because crops are often considered less productive compared to the natural vegetation they replace, though the opposite may be found for highly productive crops or on irrigated arid land (Vitousek et al., 1986; Kohlmaier et al., 1989). However, for the impact on CO_2 seasonal cycle, what matters most is the fact that crops have a short but vigorous growing season, leading to a sharper peak and larger seasonal amplitude in GPP

(Figure 2-1c inset). A sensitivity experiment shows that land cover change interacts with land management in a non-trivial way (Methods), but the contribution of crops to the increased seasonal amplitude is due mostly to higher crop productivity. Recent space-based measurements of sun-induced fluorescence (SIF) shows vividly that at the height of NH growing season (July), cropland has highest productivity, even more than the surrounding dense forests with similar climate conditions (Figure 2-8), an effect that is broadly captured by VEGAS, but in general not by the other three models analyzed.

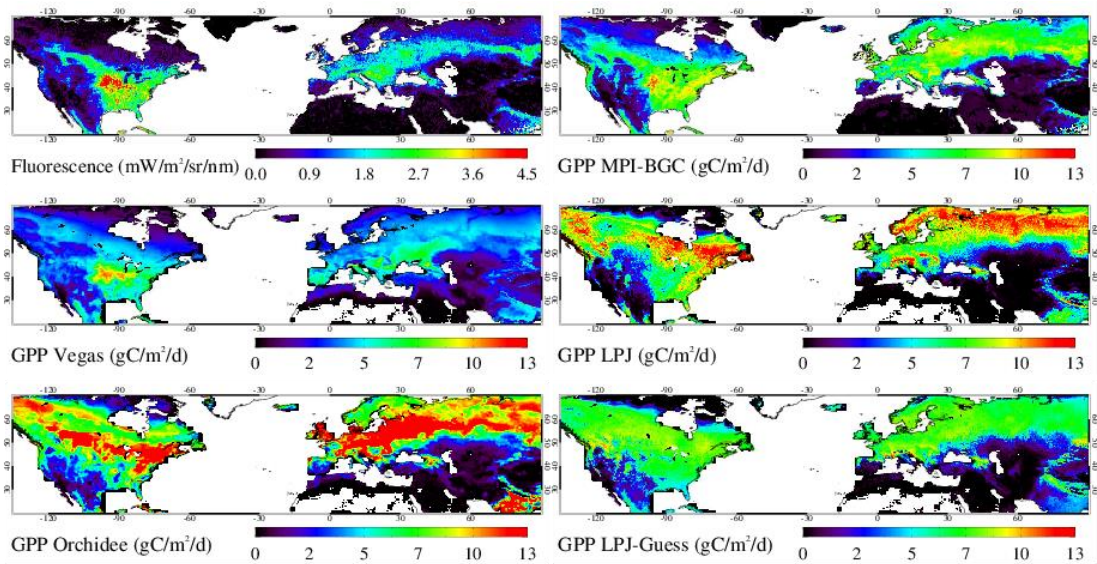


Figure 2-8: Sun-induced chlorophyll fluorescence (SIF). Measurements with the GOME-2 instrument on board the MetOp-A satellite platform (Guanter et al., 2014) are compared to GPP estimates from the data-driven model from MPI-BGC (Jung et al., 2011), and 4 mechanistic carbon cycle models (VEGAS, LPJ, Orchidee, and LPJ-Guess) from the TRENDY international project.

Data

To further delineate the relative contribution of climate, CO₂ fertilization and land use, we conducted three additional model experiments, termed CLIM, CO₂ and

LU, respectively. In each experiment, only one of the three forcings is used as model driver while the other two are fixed. Figure 2-9 shows the evolution of F_{TA} seasonal

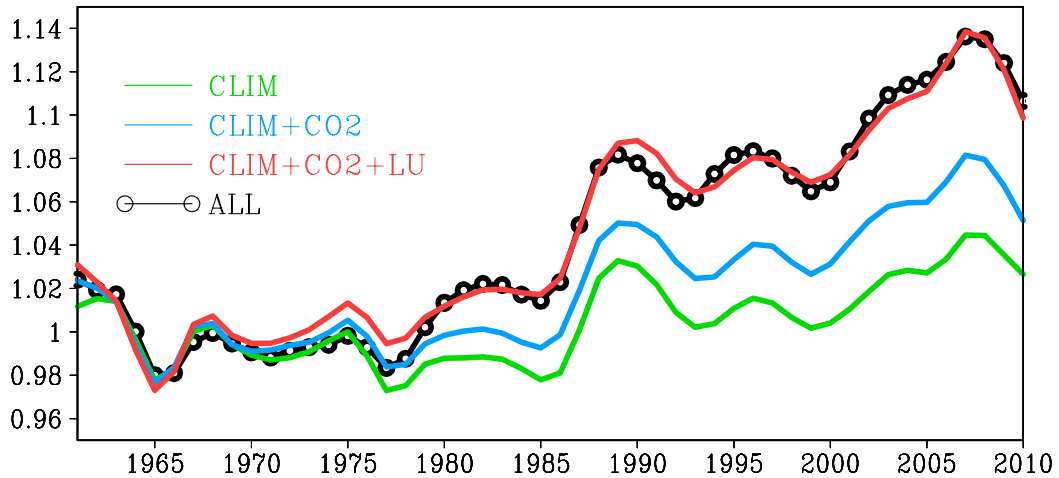


Figure 2-9: Attribution of causes with factorial analysis. Relative change of seasonal amplitude from three sensitivity experiments, each with a single forcing: climate only (CLIM), CO₂ only (CO₂), and land use and management only (LU). The results from CO₂ and LU are added on top of CLIM sequentially. The ALL experiment is the same as in Fig.2, driven by all three forcings.

amplitude, similar to Figure 2-2, but with the fluxes from the three experiments added successively. The sum of the three experiments is similar but not identical to the original simulation (ALL). We calculated the trend to be 0.088% per year for CLIM, 0.076% for CO₂, and 0.135% for LU, corresponding to percentage contributions of 29%, 26% and 45% (Table 2-2). The SUM of the three is 0.299% per year, or 3% per decade, or 15% over 50 years. Given uncertainties in the model and data, the quantitative attribution should only be considered suggestive. In particular, VEGAS has a CO₂ fertilization strength weaker than some other models that can account for

the full amplitude change with fertilization alone (McGuire et al., 2001). A more challenging task would be to explain better spatial patterns as models may underestimate significantly the high latitude trend (Graven et al., 2013) even if the global total is simulated correctly, the latter being the focus of this paper. Carbon cycle models may have a long way to go in explaining the long-term changes in the seasonal cycle (Graven et al., 2013; Guanter et al., 2014), but our results strongly suggest that intensification of agriculture should be included in consideration.

Research significance

It is generally known that land use activities such as deforestation and intense agriculture tend to release carbon to the atmosphere, and recovery from past land clearance sequesters carbon. Our study here suggests yet another aspect of human impact on the global carbon cycle and the Earth system: The very basic rhythm of seasonal ‘breathing’ of the biosphere has also been modified by human land management activities.

Methods

Data

Crop production and cropland area is aggregated from FAO statistics for the major crops (FAOSTAT, <http://faostat.fao.org/site/567/default.aspx#ancor>). Specifically, it is the sum of the cereals (wheat, maize, rice, barley, etc.) and five other major crops (cassava, oil palm, potatoes, soybean and sugarcane), which comprises of 90% of the global amount of carbon harvested. Following Ciais et al.

(2007), conversion factors are used to convert the wet biomass to dry biomass, then to carbon content. The final conversion factor from wet biomass to carbon is 0.41 for cereals, 0.57 for oil palm, 0.11 for potatoes, 0.08 for sugarcane, 0.41 for soybean and cassava.

Sun-induced chlorophyll fluorescence (SIF) data are derived from top-of-atmosphere radiance spectra measured by the Global Ozone Monitoring Experiment-2 (GOME-2) instrument on board the Eumetsat's MetOp-A platform. SIF retrievals are performed in the 715-758 nm spectral window, sampling the second peak of the SIF emission (Joiner et al., 2013). The retrievals have been quality-filtered, aggregated as monthly averages and gridded globally in half-degree grid boxes. The SIF is thought to be a direct indicator of GPP, though the relationship may be complex (Parazoo et al., 2013; Guanter et al., 2014).

Mauna Loa and global mean CO₂ are both from NOAA/ESRL (www.esrl.noaa.gov/gmd/ccgg/trends/). The MLO CO₂ record dates back to 1958 but is limited to one single station. The global average is based on multiple marine surface sites, available from 1981, and is constructed by first fitting a smoothed curve as a function of time to each site, and then the smoothed value for each site is plotted as a function of latitude for 48 equal time steps per year. A global average is calculated from the latitude plot at each time (Thoning et al., 1989; Masarie and Tans, 1995).

Atmospheric inversions use CO₂ concentration measurements from a global network of stations and information on atmospheric motion in a transport model to infer the surface CO₂ fluxes. The two inversions from the Max Planck Institute of Biogeochemistry (Rodenbeck et al., 2003) used here are version 3.4 (<http://www.bgc-jena.mpg.de/~christian.roedenbeck/download-CO2/>), with Jena81 for the period 1981-2010 using CO₂ data from 15 stations, and Jena99 from 61 stations for 1999-2010. The CarbonTracker (Peters et al., 2007) from NOAA/ESRL is the version CT2011 (<http://www.esrl.noaa.gov/gmd/ccgg/carbontracker/>), covering 2000-2010, using flask samples from 81 stations, 13 continuous measurement stations and 9 towers. CarbonTracker also uses the surface fluxes from land and ocean carbon models as prior fluxes.

Calculation of CO₂ and flux seasonal amplitude The seasonal amplitude of MLO or global CO₂ growth rate and fluxes from model and inversions was calculated as the difference between maximum and minimum values of each year using high-frequency filtered data with the standard package CCGCRV from NOAA/ESRL (<http://www.esrl.noaa.gov/gmd/ccgg/mb/krvfit/krvfit.html>), involving polynomial and harmonic fitting, detrending and band-pass filtering.

Modeling the agricultural Green Revolution

Important progress has been made in modeling agriculture in global carbon cycle models (Kucharik and Brye, 2003; Gervois et al., 2004; Bondeau et al., 2007). Such models typically simplify the problem of dealing with multiple crops by using

only a handful of crop functional types. Yet this still requires a large number of input data or assumptions on irrigation, crop selection, fertilizer use, planting, harvesting and other management practices that vary widely in space and time. More importantly, there is a general lack of information on historical changes in these driver data and parameter values so that the temporal changes are not easily represented in such models. Here we adopt a minimalist approach, aiming at capturing the first-order effects relevant to the global carbon cycle with generic rules, avoiding the need for unavailable details. Acknowledging its coarse ‘precision’, to our knowledge, it is a first attempt in global carbon cycle modeling to simulate the *intensification* of agriculture associated with the Green Revolution. The results are validated using FAO crop production, human appropriated NPP, satellite measurements of chlorophyll fluorescence and site flux measurements (below).

We simulate agriculture with a generic crop functional type that represents an average of the three dominant crops: maize, wheat and rice. The characteristics are in many respects similar to warm C3 grass, one of the natural PFTs in VEGAS (Zeng et al., 2005a). A major difference is the narrower temperature growth function to represent warmer temperature requirement than natural vegetation. Management of cropland is modeled as an enhanced gross carbon assimilation rate by the human-selected cultivar, application of fertilizers and pesticides, and irrigation. These three factors are thought to have contributed about equally to the increase in agricultural productivity over the last half century (Sinclair, 1998). However, the intensity of management varies widely and has not always changed in synchrony in different parts of the world. Instead of using an extensive set of actual management data that are not

available or incomplete, we model the first-order effects on carbon cycle by parameterizations with the following rules.

To represent the enhanced productivity from cultivar and fertilization, the gross carbon assimilation rate is modified by a management intensity factor (MI) that varies spatially and changes over time:

$$MI = M_0 M_1 (1 + 0.2 \tanh(\frac{year - 2000}{70})) \quad (1)$$

where M_1 is the spatially varying component while M_0 is a scaling parameter. M_1 is stronger in temperate and cold regions while tropical countries tend to be less, represented here using the annual mean temperature as a surrogate. The term in parentheses is the temporal change, modeled by a hyperbolic tangent function, with parameter values such that in 1961 it was about 10% lower than in 2000, and 20% lower asymptotically far back in time (Figure 2-10, top panel).

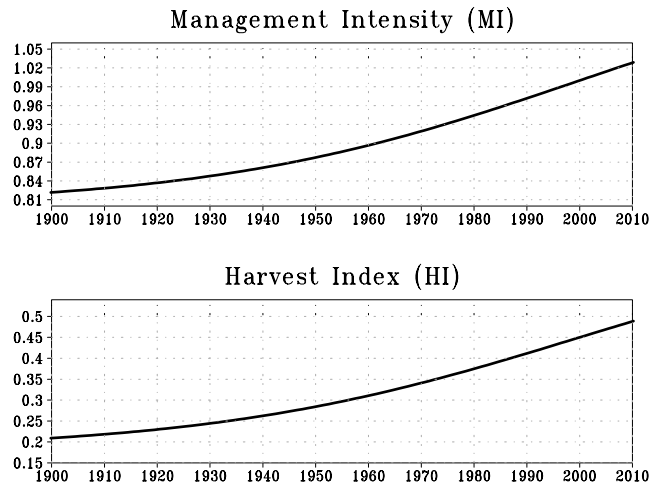


Figure 2-10: Management Intensity (MI, relative to year 2000) and Harvest Index (HI) change over time as used in the model. The analytical functions are hyperbolic tangent (see text), and the parameter values correspond to 10% smaller MI in 1961 compared to 2010, and the HI index is 0.31 in 1961 and 0.49 in 2010, based on literature review (Sinclair, 1998).

To represent the effect of irrigation, the soil moisture function beta ($\beta=w_1$ for unmanaged grass, where w_1 is surface soil wetness) is modified as:

$$b = 1 - \frac{1 - w_1}{W_{irrg}} (2)$$

The irrigation intensity W_{irrg} varies spatially from 1 (no irrigation) to 1.5 (high irrigation), corresponding to a β range of 0 (no irrigation) to 0.33 (high irrigation) under extreme dry natural condition (extreme desert: $w_1=0$). This formulation also modifies β when w_1 is not zero, but the effect of irrigation becomes smaller when w_1 increases and has no effect when w_1 is one (saturated). Thus β (therefore photosynthesis rate) depends on naturally available water (w_1) as well as irrigation. This is a ‘gentler’ approach compared to the assumption of unlimited amount of water on irrigated land, as is sometimes assumed in modeling. The spatial variation in W_{irrg} represents a tropical vs. temperate regional difference. Unlike fertilizer/cultivar effects, no temporal changes are assumed because if a place is planted with crop, some water must be made available, no matter in which period of agricultural history. This assumption may underestimate increased irrigation in some regions, but is the simplest assumption to make in the absence of region-time specific data.

Planting is not prescribed, but allowed whenever the climate condition is suitable, for example, when temperature requirement is satisfied in temperate and cool regions. This captures much of the spring planting, but misses some other types of practice such as winter wheat which has an earlier growth and harvest, a limitation of our simple rule-based approach without using actual regional agricultural practice data. Crop is harvested when crop matures, determined by LAI growth rate slowing down to a threshold value. This combination of climate-determined planting and

harvest criteria automatically leads to double crops in some warm regions, but it may or may not agree with the actual practice there. Rather, the simulated results only suggest a cropping potential given the characteristics of our generic crop and climate. After harvest, grain goes into a harvest pool whereas the residue is sent to the metabolic carbon pool and decomposes rapidly. A key advancement in agriculture has been the use of high yield dwarf cultivar with more edible parts (grain) per unit total biomass, especially since the Green Revolution in the 1960s. This is represented by the Harvest Index (HI): the edible fraction of aboveground biomass. HI varies somewhat for different crops, and we use 0.45 for year 2000, a value typical of the three major crops: maize, rice, and wheat (Sinclair, 1998; Haberl et al., 2007). The temporal change is modeled as:

$$HI_{crop} = 0.45(1 + 0.6 \tanh(\frac{year - 2000}{70})) \quad (3)$$

so that at the beginning of the Green Revolution in 1961 HI_{crop} was 0.31, a difference of 0.14 from the 2000 value of 0.45, based on literature review (Sinclair, 1998). The parameter values above also imply $HI_{crop} = 0.18$ far back in time ($year = -\infty$), and $HI_{crop}=0.49$ in 2010 (Figure 2-10, lower panel).

The harvested crop is redistributed according to population density, resulting in the lateral transport of carbon. As a result, there is net carbon uptake in cropland areas and large release of CO₂ in urban areas. To the first-order approximation, the lateral transport is applied within each continent. Additional information of cross-region trade was also implemented for eight major world economic regions.

Validation of crop simulation

There is a general lack of relevant global data on the *change* in agriculture. A key data is the FAO global crop production statistics, spanning the period 1961-present. Additionally, we validate the model simulation with estimates of global crop NPP (Haberl et al., 2007), and flux measurement (fluxdata.org) at site level. Neither of the latter two offers information on long-term change, but is useful for validating model's crop simulation of present state.

FAO statistics Our modeled crop production increased from 0.6 PgC y⁻¹ in 1961 to 1.4 PgC y⁻¹ in 2010, somewhat slower than FAO statistics (from 0.5 to 1.5) (Figure 2-1 and Table 2-1). The general trends are very similar. FAO statistics has somewhat larger year to year variation, likely due to human factors influencing crop production other than climate variability, thus not represented in the model. Note that 'crop production' in the FAO parlance is only the edible parts (mostly grain, but also include other parts such as storage organs in potatoes), while the total biological NPP on cropland is called NPP_{crop}, including all edible or non-edible biomass above and below ground. Thus NPP_{crop}, not 'crop production', is the quantity that is directly relevant to carbon cycle. The Harvest Index is needed to relate them.

Human appropriated NPP The global total NPP on cropland NPP_{crop} of cropland area is 6.2 PgC y⁻¹ at 2010, within the range of statistics-based estimate of 6.05-8.18 PgC y⁻¹ (Haberl et al., 2007). Such agreement is encouraging given the simplicity in our model representation of agriculture and the uncertainties in the

statistics-based estimates. Because of the large increase in HI, the modeled 130% increase in crop production corresponds to a smaller increase in NPP_{crop} , from 4 PgC y^{-1} in 1961 to 6.2 PgC y^{-1} in 2010, a 55% increase (Table 2-1).

Sun-induced chlorophyll fluorescence (SIF) We compared remotely sensed chlorophyll fluorescence (Parazoo et al., 2013; Guanter et al., 2014) with 4 mechanistic carbon cycle models participating in the TRENDY intercomparison project (VEGAS, LPJ, Orchidee, LPJ-Guess), and a data-driven model MPI-BGC, shown in Figure 2-8. SIF is considered a direct measurement of GPP, as opposed to net carbon flux, thus offering high-resolution global coverage of GPP that is otherwise impractical to obtain with in-situ methods. While the SIF-GPP relationship may be complex, the spatial pattern can be a particularly meaningful comparison (Guanter et al., 2014). At the height of a NH growing season (July 2009), the highest GPPs, according to the satellite fluorescence measurements, are found in US and European agricultural region. Interestingly, 3 of the 4 models do not capture this pattern, instead showing highest GPP in boreal and partly temperate forest regions. The spatial pattern of VEGAS modeled GPP agrees reasonably well with satellite fluorescence, perhaps not surprisingly as VEGAS is the only model among these four to have a representation of the increased productivity due to agricultural Green Revolution.

FLUXNET site comparison We compared the NEE and its components GPP and R_e at Bondville, Illinois, a no-till maize-soybean site of the AmeriFlux/FLUXNET network (<http://www.fluxdata.org:8080/SitePages/siteInfo.aspx?US-Bo1>). The results are shown in Figure 2-11. Model simulated NEE, GPP and R_e

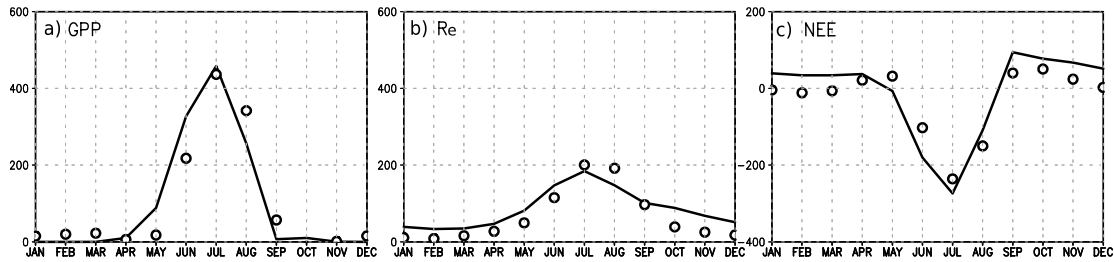


Figure 2-11: Model-Data site validation. Comparison of VEGAS model (line) and FLUXNET observations (circles) at an agricultural site Bondville, Illinois (88.290398W, 40.006199N). (a) GPP, (b) R_e (total ecosystem respiration), (c) NEE ($=R_e - GPP$; Net Ecosystem Exchange, i.e., net land-atmosphere carbon flux), in $\text{gC m}^{-2} \text{ month}^{-1}$. Shown are seasonal cycles averaged over the period 1996-2007.

are all in broad agreement with the measurements, with slightly larger seasonal amplitude in NEE. In fact, the level of agreement is somewhat surprising given the simplicity of the model. This may be in part due to the fact that our crop functional type has the characteristics that closely match this site. The carbon uptake occurs mostly during the short growing season of June-August, but at a very high rate with maximum GPP of 450 gC m^{-2} in July. This short-duration-high-growth feature can also be seen in Figure 2-1c inset, and is a major characteristic that has contributed to the increased seasonal amplitude.

Sensitivity experiment on land cover effects

There is a compounding factor of land cover change (conversions between land cover types such as cropland and natural vegetation) vs. change in land management practices (fertilizer, irrigation etc.). We inferred that the contribution to CO₂ seasonal amplitude trend is dominated by land management because of the 3-fold increase in crop production compared to only 20% cropland area change. To quantify this conjecture, we conducted an additional model sensitivity experiment in which only land cover is allowed to change but with land management fixed at 2000 value. The result is that land cover change alone would decrease the seasonal cycle amplitude of F_{TA} by 0.06% per year, compared to 0.3% per year increase in the ALL experiment (Table 2-2). Thus, the land cover change effect alone would reduce the trend (with all forcings) by 17% ($0.06/(0.3+0.06)$; assuming linearity). This is certainly a nontrivial effect, though the 2000 values for management intensities likely lead to overestimation. The fact that it decreases the seasonal amplitude against the increasing trend may be a bit surprising. This is because the overall increase in cropland area occurred mostly in the Tropics while regions north of 30N actually has seen decrease in cropland area (due to a variety of factors: cropland abandonment, reforestation, urbanization, etc.) where the seasonal cycle is most profound.

Availability of data and model output

The standard VEGAS model output analyzed here is provided through the international TRENDY project (<http://dgvn.ceh.ac.uk>) as used in the Global Carbon Project annual carbon budget analysis (Le Quéré et al., 2013) and the NACP MsTMIP project (<http://nacp.ornl.gov/MsTMIP.shtml>), downloadable from either

site. The model output and the processed data are also available directly from the authors. The use of the data is subject to fair use and the acknowledgement of the providers.

Supplementary Information

Experiments were conducted to assess a ‘parametric’ uncertainty. We asked the question “How would model simulated trend in seasonal amplitude differ if key parameters in management intensity have a given error?”. For this, we obtained a preliminary version of FAO data-based spatially-varying crop NPP estimates from T. West. We took the difference between our modeled crop NPP and this observationally-based NPP. We then used this difference to infer an ‘error bar’ of our model parameter uncertainty in management intensity (Equation 1 in Methods). We then conducted two simulations to bracket the range of resulting F_{TA} seasonal amplitude. The results are shown in Figure 2-12 below. The resulting trend has an uncertainty range of 0.311 ± 0.027 (% y^{-1}). The relative error in trend is thus 8.5% ($0.027/0.311$), which is smaller than the uncertainty associated with interannual variability which we used to indicate uncertainty (Figure 2-2).

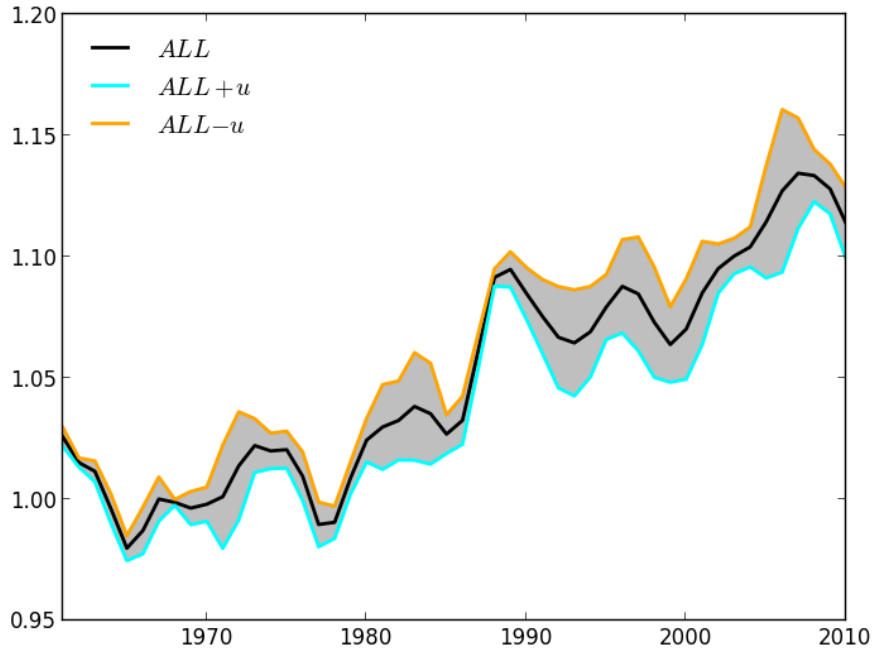


Figure 2-12: Uncertainty due to model parametric errors in representing agricultural NPP.

Acknowledgement

The authors are grateful for all data providers, especially the NOAA CO₂ and CarbonTracker team, and the Jena inversion team. M. Heimann suggested the flux data site comparison. The anonymous reviewers suggested the land cover sensitivity experiment and uncertainty analysis. This research was supported by NOAA (NA10OAR4310248 and NA09NES4400006) and NSF (AGS-1129088).

Author contributions

NZ designed the research and all authors contributed to the ideas. NZ and FZ conducted the simulations and data analysis. LG analyzed the TRENDY models and satellite SIF data. NZ wrote the paper with input from all others.

Chapter 3: Attributing the role of CO₂, climate and land use in regulating the seasonal carbon fluxes in terrestrial ecosystems: a multimodal analysis

Preface

Fang Zhao¹, Ning Zeng¹, Rashid Rafique², Ghassam Asrar², Eugenia Kalnay¹, Stephen Sitch³, Pierre Friedlingstein³, Charles D. Koven⁴, Atul Jain⁵, Shijie Shu⁵, Andy Wiltshire⁶, Ben Poulter⁷, Beni Stocker⁸, Sonke Zaehle⁹, Nicolas Viovy¹⁰, Etsushi Kato¹¹, Ito Akihiko¹²

¹Department of Atmospheric and Oceanic Science and Earth System Science Interdisciplinary Center, University of Maryland, College Park, MD 20742, USA

²Joint Global Change Research Institute, Pacific Northwest National Laboratory, College Park, MD 20742, USA

³University of Exeter, Exeter EX4 4QF, UK

⁴Earth Sciences Division, Lawrence Berkeley National Laboratory, Berkeley, CA 94720, USA

⁵Department of Atmospheric Sciences, University of Illinois, Urbana, IL 61801, USA

⁶Met Office Hadley Centre, Exeter EX1 3PB, United Kingdom;

⁷Institute on Ecosystems and Department of Ecology, Montana State University, Bozeman, MT 59717, USA

⁸Climate and Environmental Physics, Physics Institute, University of Bern, 3012 Bern, Switzerland

⁹Biogeochemical Integration Department, Max Planck Institute for Biogeochemistry,
P.O. Box 10 01 64, 07701 Jena, Germany

¹⁰Laboratoire des Sciences du Climat et de l'Environnement, CEA CNRS UVSQ,
91191 Gif-sur-Yvette, France

¹¹Global Environment Program Research & Development Division, the Institute of
Applied Energy (IAE), 105-0003 Japan

¹²Center for Global Environmental Research, National Institute for Environmental
Studies, 305-0053 Tsukuba, Japan

Expect to submit soon

Abstract

Seasonal amplitude increase in atmospheric CO₂ directly reflects the dynamics of terrestrial ecosystems. Several studies have tried to explain the amplitude increase with different controlling factors, but the precise understanding on their relative contribution is still lacking. In this study, the net terrestrial carbon flux to the atmosphere (F_{TA}) simulated by nine models from the TRENDY dynamic global vegetation model project during 1961-2012 are examined for its mean seasonal cycle and amplitude trend. While some models exhibit similar phase and amplitude compared to atmospheric inversions, with spring-early summer drawdown and late summer-autumn rebound, some other models tend to rebound too early in mid-summer. The increasing trend of global F_{TA} amplitude (19%) and its decadal variability for 1961-2012 from the model ensemble generally agrees with surface observations. However, models' ensemble mean underestimates the magnitude of the

seasonal cycle by 40% compared to atmospheric inversions. For the increase in global F_{TA} amplitude, factorial experiments attribute $83 \pm 56\%$, $-3 \pm 74\%$ and $20 \pm 30\%$ to rising CO_2 , climate change and land use/cover change, respectively. Seven out of the nine models suggest that CO_2 fertilization effect is a stronger control over the F_{TA} amplitude increase—with the notable exception of VEGAS, which attributes approximately equally to the three factors. Generally, all models display an enhanced seasonality over the boreal region in response to high-latitude warming, but a negative climate contribution from part of the Northern Hemisphere temperate region, and the net result is a divergence over the effect of climate change. Six of the nine models show positive land-use effect, but the spatial patterns are substantially different. In general, models with a larger amplitude increase tend to have a larger gain in land carbon sink ($R^2=0.61$). Our results suggest that understanding the regional difference in the effect of rising CO_2 , climate and land use/cover changes is crucial in improving model representation of global carbon cycle.

Introduction

The amplitude of CO_2 seasonal cycle, largely controlled by vegetation dynamics in Northern Hemisphere (NH) (Hall et al., 1975; Pearman and Hyson, 1980; Bacastow et al., 1985), is a good indicator of terrestrial ecosystem activities. Since 1958, atmospheric CO_2 measurements at Mauna Loa, Hawaii have tracked a 15% rise in the peak-to-trough amplitude of the detrended CO_2 seasonal cycle, suggesting an enhanced ecosystem activity due to changes in ecosystem production or respiration strength or due to a shift in the relative timing of their phases (Randerson et al., 1997). In addition, some evidence suggests a latitudinal gradient in CO_2 amplitude

increase in the NH, with larger increase at Pt. Barrow, Alaska ($0.6\% \text{ y}^{-1}$) than at Mauna Loa ($0.32\% \text{ y}^{-1}$) (Randerson et al., 1999; Graven et al., 2013). Previous studies have attempted to attribute the long-term CO_2 amplitude increase to stimulated vegetation growth under rising CO_2 and increasing nitrogen deposition (Bacastow et al., 1985; Sillen and Dieleman, 2012; Reich and Hobbie, 2013). Another possible explanation offered is the effect of warmer climate, especially in boreal and temperate regions, on the lengthening of growing season, enhanced plant growth (Keeling et al., 1996; Keenan et al., 2014), vegetation phenology (Thompson, 2011), ecosystem composition and structure (Graven et al., 2013). The agricultural green revolution due to widespread irrigation, increasing management intensity and high-yield crop selection, could also contribute to the dynamics of the CO_2 seasonal amplitude (Zeng et al., 2014; Gray et al., 2014). Even though these studies are helpful in understanding the role of CO_2 , climate and land use/cover changes, the detailed understanding of the relative contribution of these factors still remains unclear.

Dynamic vegetation models are useful tools not only in understanding the contribution of various mechanisms but also offering insights on how terrestrial ecosystems respond to external changes. There are a few studies that have tried to examine the CO_2 amplitude increase. For example, in a unique modeling study conducted by McGuire et al. (2001), both CO_2 fertilization and land use/cover changes were found to contribute to CO_2 amplitude increase at Mauna Loa, but the four models disagreed on the role of climate and the relative importance of the factors they studied. Using a four-box diffusing model, Thompson (2011) found that a shift springtime phenology of terrestrial biomes is the dominant factor contributing to CO_2

amplitude increase. Similarly, by analyzing data from aircraft campaigns, Graven et al. (2013) suggested that strong climate effect altering ecosystem structure could possibly be the leading cause of observed amplitude increase over Northern mid-high latitudes. They also found that models underestimate significantly the amplitude increase compared to observations north of 45N obtained at 3-6 kilometer altitude(Graven et al., 2013), even though the models seem to be able to simulate the amplitude increase measured at the Mauna Loa and Point Barrow surface stations (Zhao and Zeng, 2014). In addition to aforementioned reasons, agricultural intensification could be of similar importance in regulating the CO₂ amplitude increase (Zeng et al. 2014). Based on these and other reported studies, it is difficult to determine independent and relative contribution and importance of each of these factors. Since the published work by McGuire et al. (2001), no specific study has explored the reliability of models' simulation of seasonal carbon cycle and quantified the relative contribution of various factors affecting it. Recent simulations from models participating the TRENDY model intercomparison project provide an opportunity to evaluate how well these models simulate the seasonal cycle of carbon flux (global and large latitudinal band) and investigate the importance of various model factors in controlling the amplitude increase in global carbon cycle.

An important trait of the three main factors we consider in this study (i.e. CO₂, climate and land use/cover change) is their different regional influence. Rising CO₂ would likely enhance productivity in all ecosystems at both regional and global levels. Climate warming may affect high latitude ecosystems more than tropical and subtropical vegetation, and droughts would severely affect plant growth in water-

limited regions. Similarly, the effect of land use/cover change may be confined to agricultural fields and places with land conversion, mostly in mid latitude regions. Therefore, it is necessary to investigate the regional patterns of seasonal cycle change of carbon flux. A number of recent studies have addressed different aspects of the seasonal amplitude. For example, Peng et al. (2015) performed extensive evaluation on the first synthesis of TRENDY models (Sitch et al., 2015), comparing the seasonal cycle of modeled carbon flux against site measurements; however, they did not explore the increase of seasonal amplitude. Based on another model intercomparison project—MsTMIP (Huntzinger et al., 2013; Wei et al., 2014), Ito et al. (2015) focused on examining the relative contribution of CO₂, climate and land use/cover changes, but little model evaluation was performed. In order to further explore and understand the seasonal fluctuation of carbon fluxes, a more comprehensive study including both the model evaluation and factorial analysis is needed.

Using both the latest TRENDY models simulations and observations, in this study we aim to achieve two main goals: 1) Assess how well the models simulate the climatological seasonal cycle and seasonal amplitude change of the carbon flux against a number of observational based datasets (CO₂ observations and atmospheric inversions); 2) Analyze the relative contribution from the three main factors (CO₂ fertilization, climate and land use/cover change) to the seasonal amplitude increase, both at the global and regional level.

Methods

Terrestrial Ecosystem Models

Monthly net biosphere production (NBP) simulations for 1961-2012 from nine TRENDY models participating in the Global Carbon Project (GCP2012, <http://www.globalcarbonproject.org>) are examined (Table 3-1). We primarily evaluated

Table 3-1: Basic information for the nine TRENDY models used in this study.

Model Name	Abbreviation	Spatial Resolution	Nitrogen Cycle	Reference
Community Land Model 4.5	CLM4.5BGC	1.25 ° × 0.94 °	yes	Oleson et al. (2013)
ISAM	ISAM	0.5 ° × 0.5 °	yes	Jain et al. (2013)
Joint UK Land Environment Simulator	JULES	1.875 ° × 1.25 °	no	Clark et al. (2011)
Lund-Potsdam-Jena	LPJ	0.5 ° × 0.5 °	no	Sitch et al. (2003)
LPX-Bern	LPX-Bern	0.5 ° × 0.5 °	yes	Stocker et al. (2014)
ORCHIDEE-CN	OCN	0.5 ° × 0.5 °	yes	Zaehle and Friend (2010)
ORCHIDEE	ORCHIDEE	2 ° × 2 °	no	Krinner et al. (2005)
VEGAS	VEGAS	0.5 ° × 0.5 °	no	Zeng et al. (2005)
VISIT	VISIT	0.5 ° × 0.5 °	no	Kato et al. (2013)

results from the most realistic S3 experiment, where the models are driven by time-varying CO₂, climate and land use/cover data (Appendix A). In addition, we also used results from the S1 (time-varying CO₂ only, with repeated or randomized or fixed climate cycles and constant 1860 land use) and S2 (time-varying CO₂ and climate, but constant 1860 land use) experiments.

Observations and observational based estimates

One of the most important reasons for the large uncertainty associated with the terrestrial ecosystem models is the lack of observation constraints. This is especially true for long-time continuous CO₂ records extending back to the 1960s. Nevertheless, we believe it is still valuable to first evaluate the spread of the models, and whether they are able to capture the features of CO₂ seasonal cycle. Although not a direct comparison (terrestrial carbon fluxes contribute about 90% to the seasonal cycle of CO₂, as indicated by Randerson et al., 1997 and Graven et al., 2013), monthly Mauna Loa record from 1961 to 2012 and a global monthly CO₂ index for the period of 1981-2012 are employed, both retrieved from NOAA's *ESRL* (www.esrl.noaa.gov/gmd/ccgg/trends/). Details on the derivation of the global CO₂ index can be found in Thoning et al. (1989) and Masarie and Tans (1995).

A more direct comparison with fluxes from the process-based models are monthly gridded fluxes from atmospheric inversions, which combine measured atmospheric CO₂ concentration at multiple sites across the globe with atmospheric tracer transport driven by meteorological data. Two representative inversions, Jena (Jena81 and Jena99, Rodenbeck et al., 2003) and the CarbonTracker (Peters et al.,

2007), are included for comparison (Appendix B). For an exhaustive intercomparison of the atmospheric inversions, see Peylin et al. (2013).

Calculating the mean seasonal cycle and its amplitude change

All monthly NBP and inversion derived fluxes are first resampled to a uniform $0.5^\circ \times 0.5^\circ$ global grid in unit of $\text{kgC m}^{-2} \text{y}^{-1}$. For the TRENDY model simulations, we further define net carbon flux from terrestrial to the atmosphere (F_{TA}), which simply reverses the sign of NBP, so that positive F_{TA} indicates net carbon release to the atmosphere, and negative indicate net carbon uptake. F_{TA} represents the sum of residual land sink and land use emission, including fluxes from ecosystem production and respiration, fire, harvest, etc., although some model may not simulate all the processes. Changes in global atmospheric CO_2 concentration then equal to F_{TA} plus ocean-atmosphere flux and fossil fuel emission. For inversion-derived fluxes, only terrestrial ecosystem fluxes are used (bio optimized flux plus fire flux for carbon tracker), which are conceptually similar to F_{TA} except that atmospheric transport is included. Atmospheric transport can significantly affect local carbon fluxes (Randerson et al., 1997), however, the impact is limited on global and large zonal band totals.

Consistent with previous studies (Buermann et al., 2007; Graven et al., 2013), the seasonal amplitude of Mauna Loa Observatory or global CO_2 growth rate and fluxes from model simulations and inversions are computed with the CCGCRV package from NOAA/ESRL (<http://www.esrl.noaa.gov/gmd/ccgg/mbi/crvfit/crvfit.ht>

[ml](#)). This package first filtered out the high-frequency signals with a series of internal steps involving polynomial and harmonic fitting, detrending and band-pass filtering, and then the amplitude is defined as the difference between each year's maximum and minimum. For the latitudinal plots only, we simply use maximum and minimum of each year as seasonal amplitude without first filtering the data. Previous studies (Randerson et al., 1997; Graven et al., 2013) have established that F_{TA} accounts for most of seasonal amplitude change from atmospheric CO_2 , and Mauna Loa CO_2 record is considered to represent the evolution of global mean CO_2 well (Kaminski et al., 1996). Therefore, similar to our earlier work (Zeng et al., 2014), we evaluated the amplitude change of modeled F_{TA} with Mauna Loa CO_2 , ESRL's global CO_2 and the atmospheric inversions, to assess whether the models are able to capture both the global trend and latitudinal patterns. For relative amplitude changes, we compute the multi-model ensemble mean after deriving the time series (relative to their 1961-1970 mean) from individual model simulations, so that models with large amplitude change would not have a huge effect on the ensemble mean. Additionally, global and regional mean seasonal cycles between the models and inversions are compared. We further compared the seasonal amplitude of zonally averaged F_{TA} from TRENDY and atmospheric inversions. To smooth out minor variations but ensure similar phase in aggregation, we first resampled F_{TA} into 2.5° resolution, then summed over latitude bands for the 2001-2010 mean F_{TA} seasonal cycle.

Factorial analyses

A major part of this study is to determine the relative contribution to F_{TA} seasonal amplitude from the three factors: CO_2 fertilization, climate change, and land

use/cover change. Firstly, relative amplitude for 1961-2012 (relative to 1961-1970 mean seasonal amplitude) from the experiments S1, S2 and S3, respectively, are calculated using the CCGCRV for each model, and a linear trend (in % y^{-1}) is determined for that period. We assume that models simulate these three main effects fairly linear, and the use of relative amplitude for percentage change would minimize impacts of some differing implementation choices like climate data in S1 (CO_2) among the models. Therefore, the S2 (CO_2 +Climate) results would show a trend that is the sum of CO_2 and climate effects, and the S3 (CO_2 +Climate+Land Use/Cover) simulations would include trends from time-varying CO_2 , climate and land use/cover change (abbreviated as LandUse for text and figures). With this linear assumption, effect of CO_2 , climate and land use/cover are quantified as the trend for S1, trend of S2 minus S1 trend, and trend of S3 minus S2 trend, respectively.

Spatial attribution

Spatial attribution of global F_{TA} amplitude change can be complicated due to the phase difference at various latitudes. For example, the two amplitude peaks at Northern and Southern subtropics caused by monsoon movements are largely out of phase, and the net contribution to global F_{TA} amplitude increase after their cancelation is small (Zeng et al., 2014). For the purpose of quantifying latitudinal and spatial contributions for each model, we define a unique quantity—“max-min difference”—as the difference between each model’s global F_{TA} maximum and minimum of its 2001-2010 mean seasonal cycle summarized in Table 3-2. For example, for VEGAS, this “max-min difference” is F_{TA} in November minus F_{TA} in July in each year. For another model, the months of F_{TA} maximum/minimum (Table

3-2), therefore its defined “max-min difference” could be different. Then, for all three experiments conducted by all models, trends of this “two-month difference” over 1961-2012 are computed at every latitude band. The spatial aggregation of the resulting latitudinal-dependent trends would then approximately equal to trend of global F_{TA} maximum-minus-minimum seasonal amplitude.

Results

Mean seasonal cycle of F_{TA}

Four of the nine models (CLM4.5BGC, LPX-Bern, ORCHIDEE and VEGAS) simulate a mean global F_{TA} seasonal cycle of similar amplitude and phase compared with the Jena99 and CarbonTracker inversions (Figure 3-1, Table 3-2). The other five

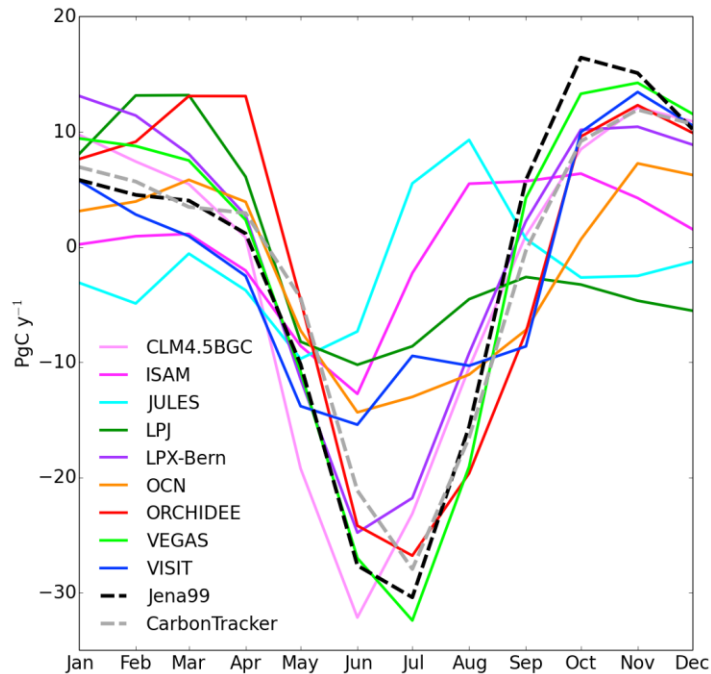


Figure 3-1: Mean seasonal cycle of global net carbon flux from nine TRENDY models (S3 experiment) and two inversions, Jena99 and CarbonTracker, averaged over 2001-2010.

models have much smaller seasonal amplitude than inversions, and the shape of the mean seasonal cycle is also notably different. As a result, models' ensemble global F_{TA} has seasonal amplitude of 26.1 PgC y^{-1} during 2001-2010, about 40% smaller than the inversions (Table 3-2). The model's ensemble annual mean F_{TA} (residual land sink plus land use emission) is -1.1 PgC y^{-1} for 2001-2010, 30% smaller than the inversions (Table 3-2). With the exception of ORCHIDEE and VEGAS,

Table 3-2: Global mean net land carbon flux, seasonal amplitude, the maximum and minimum months of F_{TA} for the nine TRENDY models and their ensemble mean during 1961-1970 and 2001-2010 periods. For the later period, characteristics of the atmosphere inversions Jena99 and CarbonTracker are also listed.

Model	F_{TA} (PgC y^{-1})		Seasonal Amplitude (PgC y^{-1})		F_{TA} Minimum	F_{TA} Maximum
	1961-1970	2001-2010	1961-1970	2001-2010	2001-2010	2001-2010
CLM4.5BGC	0.1	-2.4	38.4	44.3	Jun	Nov
ISAM	0.7	0.0	17.6	19.1	Jun	Oct
JULES	-0.2	-1.7	15.1	19.0	May	Aug
LPJ	1.3	-0.6	18.6	23.4	Jun	Mar
LPX-Bern	0.6	0.0	33.0	37.9	Jun	Jan
OCN	0.9	-1.8	16.1	21.6	Jun	Nov
ORCHIDEE	0.1	-0.7	35.7	39.9	Jul	Mar
VEGAS	-0.4	-1.5	40.7	46.7	Jul	Nov
VISIT	0.2	-1.4	25.3	28.9	Jun	Nov
Ensemble	0.4	-1.1	22.4	26.1	Jun	Nov
Jena99		-1.7		46.8	Jul	Oct
CarbonTrack		-1.6		39.9	Jul	Nov

maximum CO₂ drawdown simulated by the models is one to two months earlier than inversions (Table 3-2). In some models (ISAM, JULES, and LPJ to a lesser extent) F_{TA} rebounds back quickly, resulting in a late summer F_{TA} maximum. A likely cause is the strong exponential response of soil respiration to temperature increase, which may lead to heterotopic respiration higher than NPP in summer. For example, the HadCM3LC that employs TRIFFID, an earlier version of JULES3.2 used in this study, is found to have a large mid-summer peak carbon release over temperate North America (Cadule et al., 2012). Another possibility is carbon release from crop harvest. However, such effect may be limited, as the annual harvested carbon flux in several models including LPJ is spread over 12 months to minimize the rapid flux (Poulter 2015, personal communication).

TRENDY models and inversions agree best over the boreal region (Figure 3-2). While underestimating the global seasonal cycle, LPJ and VISIT both simulate similar boreal F_{TA} amplitude as inversions. In addition to ORCHIDEE and VEGAS, LPJ and LPX-Bern also simulate maximum CO₂ drawdown in July for the boreal region, same as the inversions, while the other five models have the F_{TA} minimum in June. Large model spread is present for the Northern temperate region especially in summer. Both inversions and models agree marginally over the phase of the F_{TA} seasonal cycle in the tropics. The Northern and Southern tropics show mean seasonal cycles that are largely out of phase except for LPJ. The Southern extra-tropics exhibit even smaller F_{TA} amplitude due to its small biomass, and most models and inversions indicate a maximum F_{TA} in the NH summer, opposite in phase to its NH counterpart.

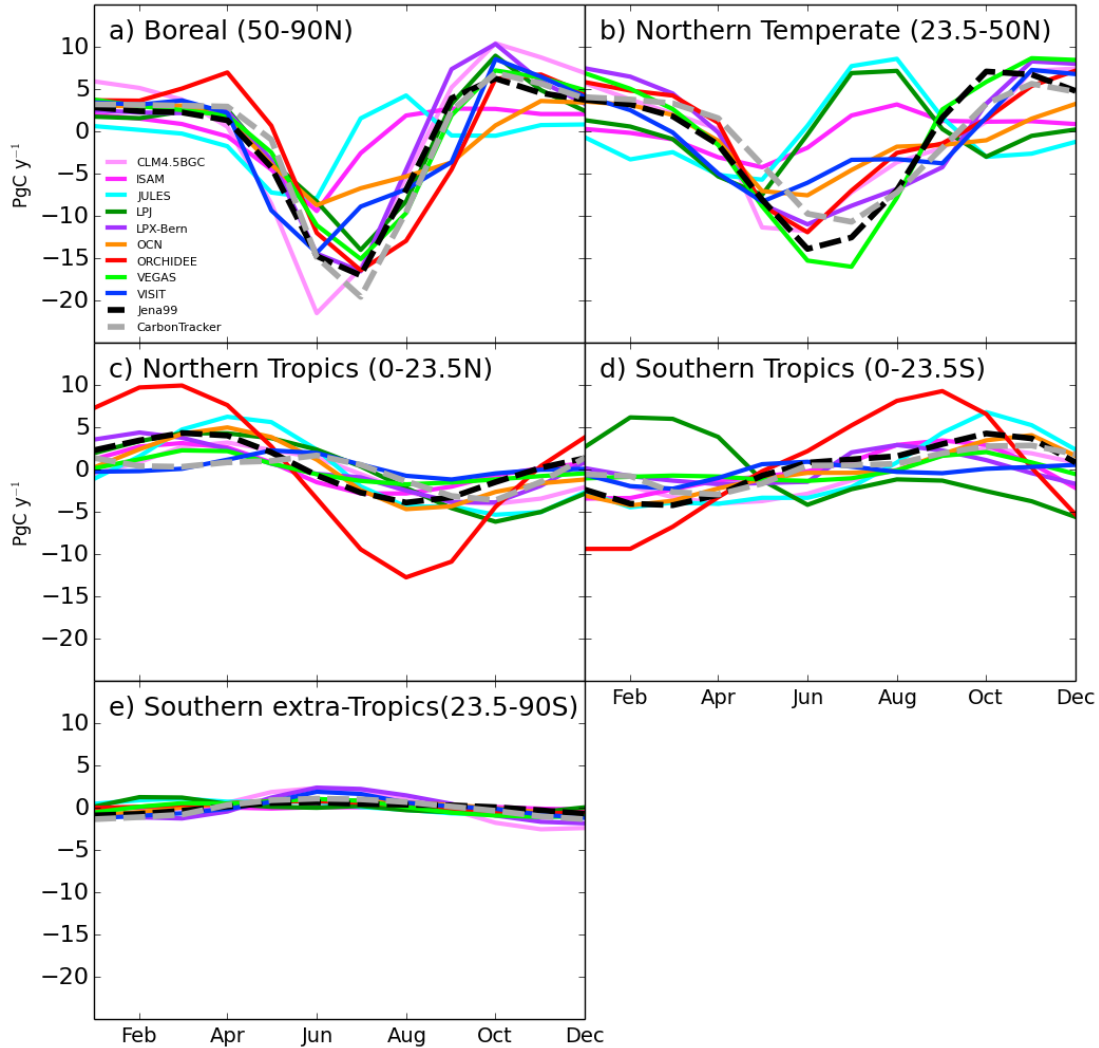


Figure 3-2: Mean seasonal cycle of net carbon flux totals over boreal (50-90N), Northern temperate (23.5-50N), Northern tropics (0-23.5N), Southern tropics (0-23.5S) and Southern extra-tropics (23.5-90S) from nine TRENDY models and two inversions, Jena99 and CarbonTracker, averaged over 2001-2010.

The latitudinal pattern of the multi-model median F_{TA} amplitude is remarkably similar to the inversions (Figure 3-3). A notable feature is the large seasonality over NH mid-high latitude region driven by temperature contrast between winter and summer. The model median also captures the two subtropical maxima around 10N and 15S that are caused by tropical monsoon movement. The main difference

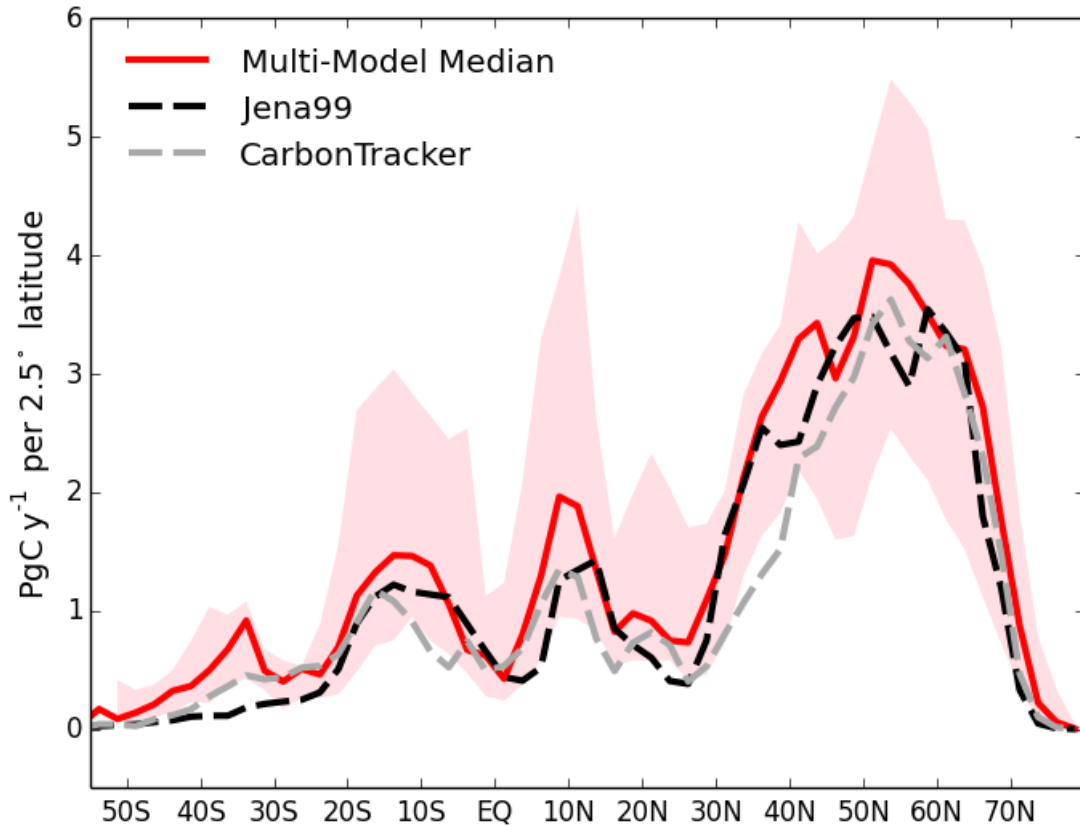


Figure 3-3: Latitude dependence of the seasonal amplitude of land-atmosphere carbon flux from the TRENDY multi-model median (red line, and the pink shade indicates 10 to 90 percentile range of model spread) and two atmospheric CO₂ inversions Jena99 and CarbonTracker. Fluxes are first resampled to 2.5° × 2.5° grids, then summed over each 2.5° latitude bands (PgC y⁻¹ per 2.5° latitude) for the TRENDY ensemble and inversions.

between the TRENDY models and the two inversions is in the tropics and SH, with the models showing higher amplitude and large spread in the tropics, mostly from the ORCHIDEE model (Figure 3-4). Seasonal amplitude over 37-45N and 53-60N is also larger from TRENDY models than the inversions. A majority of the models display larger amplitude in the tropics and Northern temperate regions (Figure 3-4). Only three models (ISAM, JULES and OCN) exhibit underestimation of seasonal amplitude in the north of 45N. Because of phase difference among the models and at

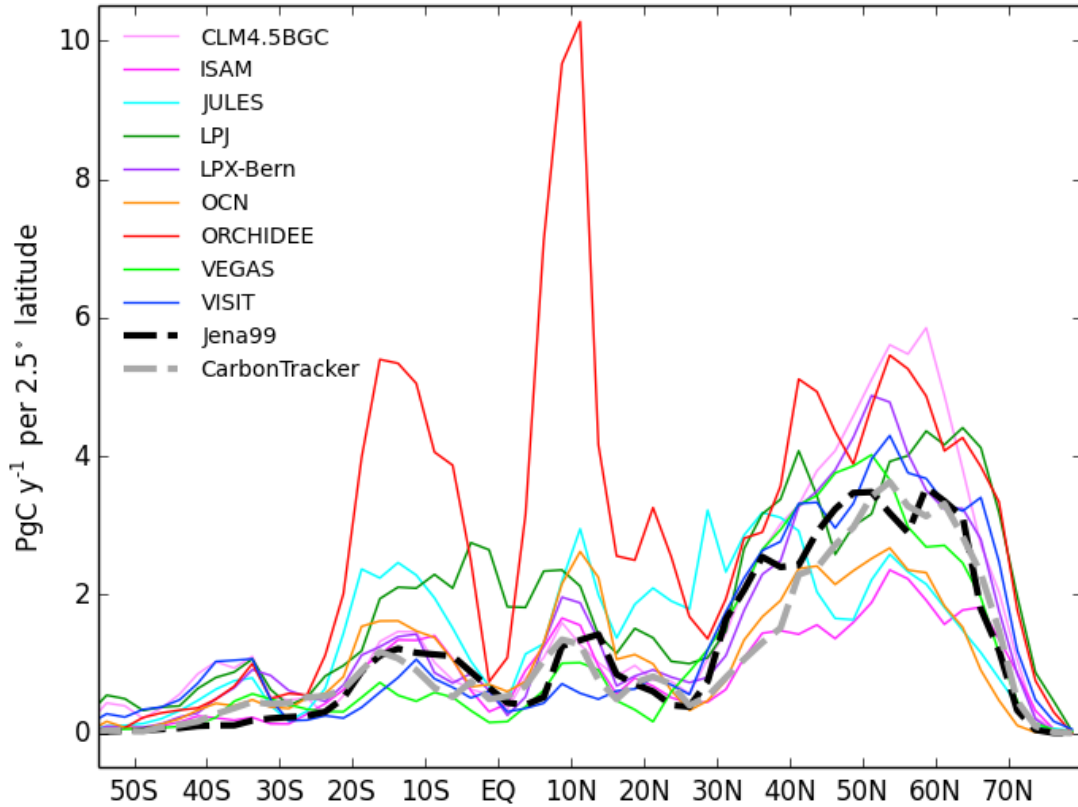


Figure 3-4: Latitude dependence of the seasonal amplitude of land-atmosphere carbon flux from each TRENDY model and two atmospheric CO₂ inversions Jena99 (black dashed) and the CarbonTracker (grey dashed). Fluxes are first resampled to $2.5 \times 2.5^\circ$ grids, then summed over each 2.5° latitude bands (PgC y^{-1} per 2.5° latitude) for the TRENDY ensemble and inversions.

different latitudinal bands, for spatial and cross-model aggregated carbon fluxes, the seasonal amplitude is reduced. Similarly, analyses by Peng et al. (2015) with an earlier set of TRENDY models (Sitch et al., 2015) show approximately equal number of models overestimating and underestimating carbon flux compared to flux sites north of 35N. However, once the carbon fluxes of different phases are transported and mixed, seven out of nine models underestimate the CO₂ seasonal amplitude compared to CO₂ site measurements (Peng et al., 2015). Note that even at the same latitude

band, factors like monsoons, droughts, and spring snow melt, etc. could lead to longitudinal difference in the phase of seasonal cycle (Figures 3-5 and 3-6).

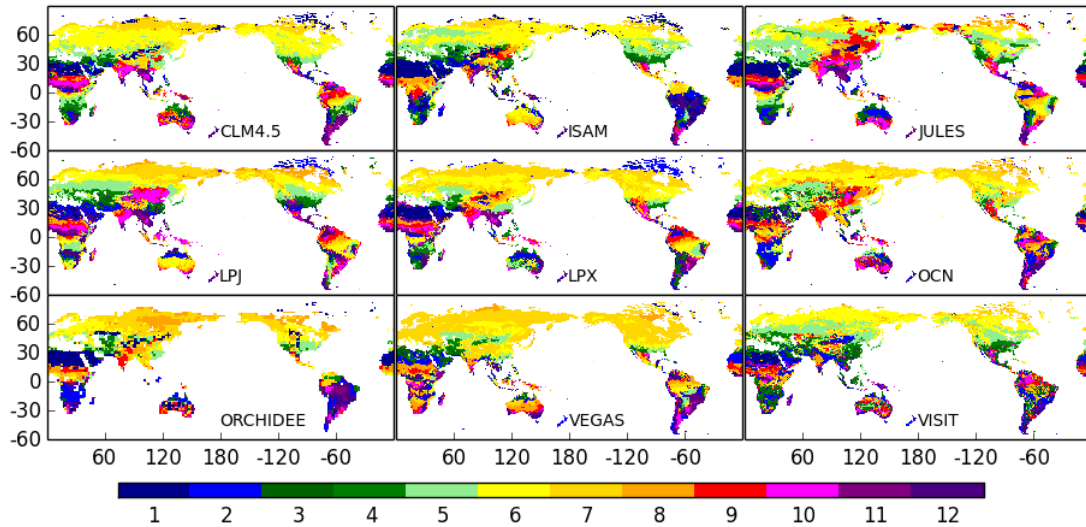


Figure 3-5: The F_{TA} minimum (peak carbon uptake) month for the 2001-2010 average for each spatial grid based on the S3 experiment results from the nine TRENDY models.

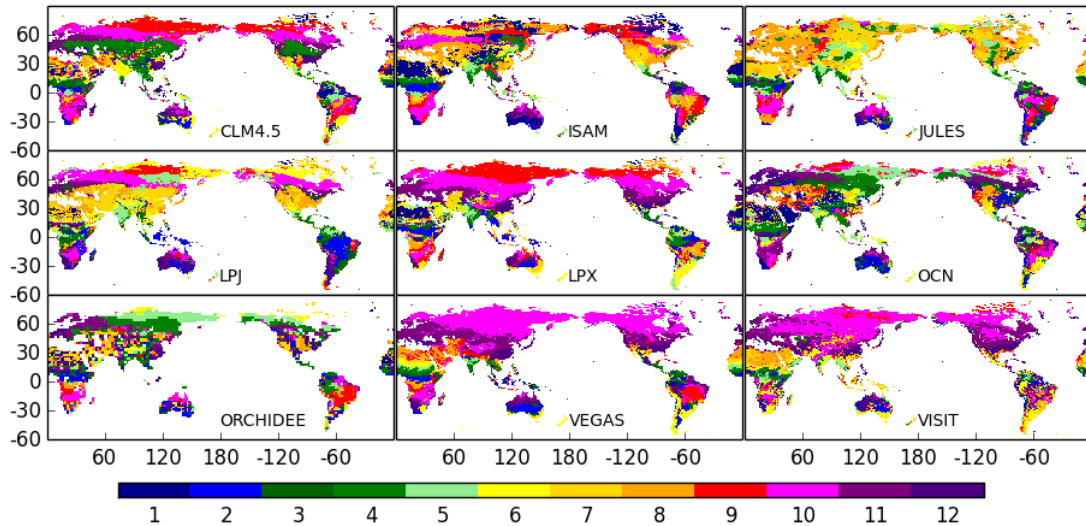


Figure 3-6: The F_{TA} maximum (peak carbon release) month for the 2001-2010 average for each spatial grid based on the S3 experiment results from the nine TRENDY models.

Temporal evolution of FTA seasonal amplitude

During 1961-2012, the seasonal amplitude of Mauna Loa CO₂ observations has increased by 0.85 ± 0.18 ppm—an increase of $15 \pm 3\%$ over 52 years (Figure 3-7).

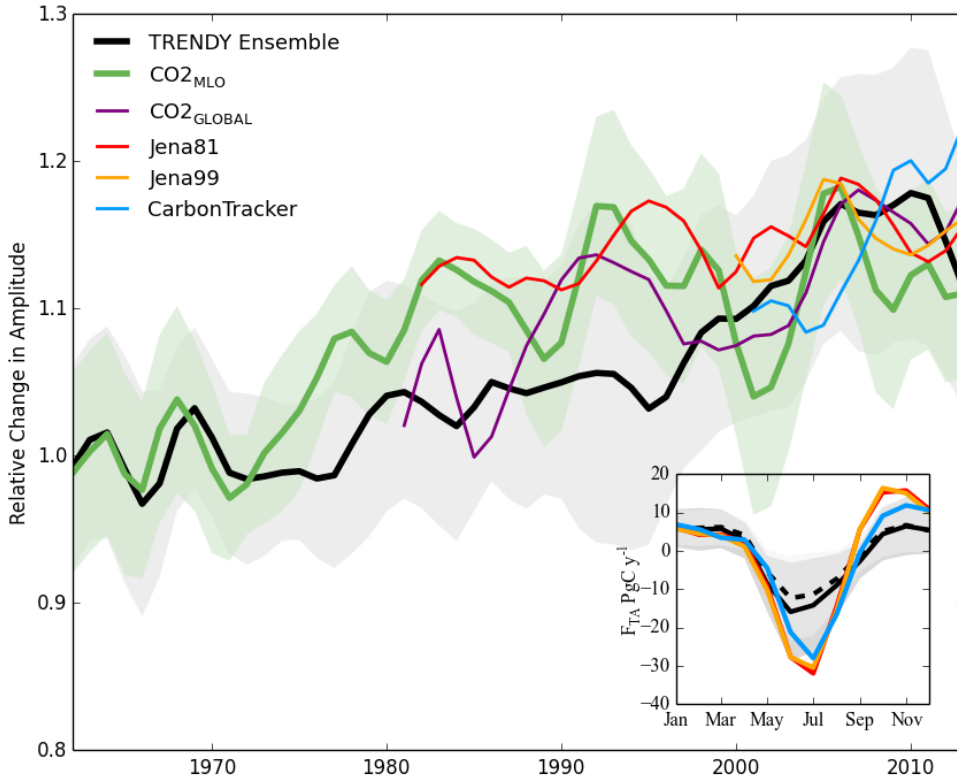


Figure 3-7: Trends for seasonal amplitude of TRENDY simulated multi-model ensemble mean land-atmosphere carbon flux F_{TA} (black), of MLO CO₂ mixing ratio (CO_{2MLO} , green) and global CO₂ mixing ratio ($CO_{2GLOBAL}$, purple), and of F_{TA} from atmospheric inversions of Jena81 (red), Jena99 (orange), and CarbonTracker (blue). The trends are relative to the 1961-70 mean for the TRENDY ensemble and Mauna Loa CO₂, and the other time series are offset to have the same mean as the TRENDY ensemble for the last ten years (2003-2012). A 9-year Gaussian smoothing (Harris, 1978) removes inter-annual variability for all time series, and its 1- σ standard deviation is shown for CO_{2MLO} (green shading). Note that the grey shading here instead indicates 1- σ models' spread, which is generally larger than the standard deviation of TRENDY ensemble's decadal variability. Inset: average seasonal cycles of models' ensemble mean F_{TA} ($PgC\ y^{-1}$) for the two periods: 1961-1970 (dashed, lighter grey shade indicates 1- σ model spread) and 2001-2010 (solid, darker grey shade indicates 1- σ model spread), revealing enhanced CO₂ uptake during spring/summer growing season. Mean seasonal cycles global F_{TA} from the atmospheric inversions for 2001-2010 are also shown (same color as the main figure) for comparison.

Similarly, the seasonal amplitude of global total F_{TA} simulated by TRENDY models shows an increasing trend of $19 \pm 8\%$ for the same period. This amplitude increase appears mostly as an earlier and deeper drawdown during the spring and summer growing season, mostly in June and July (Figure 3-7 inset). Changes in peak carbon uptake contribute to $91 \pm 10\%$ of the amplitude increase, while increase in respiration contributes to $9 \pm 10\%$ of the amplitude increase. Gurney and Eckels (2011) suggest trend in respiration increase is more important, but they averaged all months instead of maxima and minima in their amplitude definition. The multi-model ensemble mean tracks some characteristics of the decadal variability reflected by the Mauna Loa record: stable in the 1960s, rise in the 1970-1980s, rapid rise in the early 2000s, and decrease in most recent 10 years. One notable mismatch is during the 1990s: a declining trend is found for Mauna Loa CO₂'s seasonal amplitude, which may be related a decadal shift of atmospheric transport (Buermann et al., 2007), while the model ensemble shows a continued increasing trend in global FTA amplitude. Nevertheless, about half of the models do mirror the decreasing trend in the 1990s (Figure 3-8). Details on models' FTA global and regional amplitude changes in 2001-2010 compared to 1961-1970 are listed in Table 3-3.

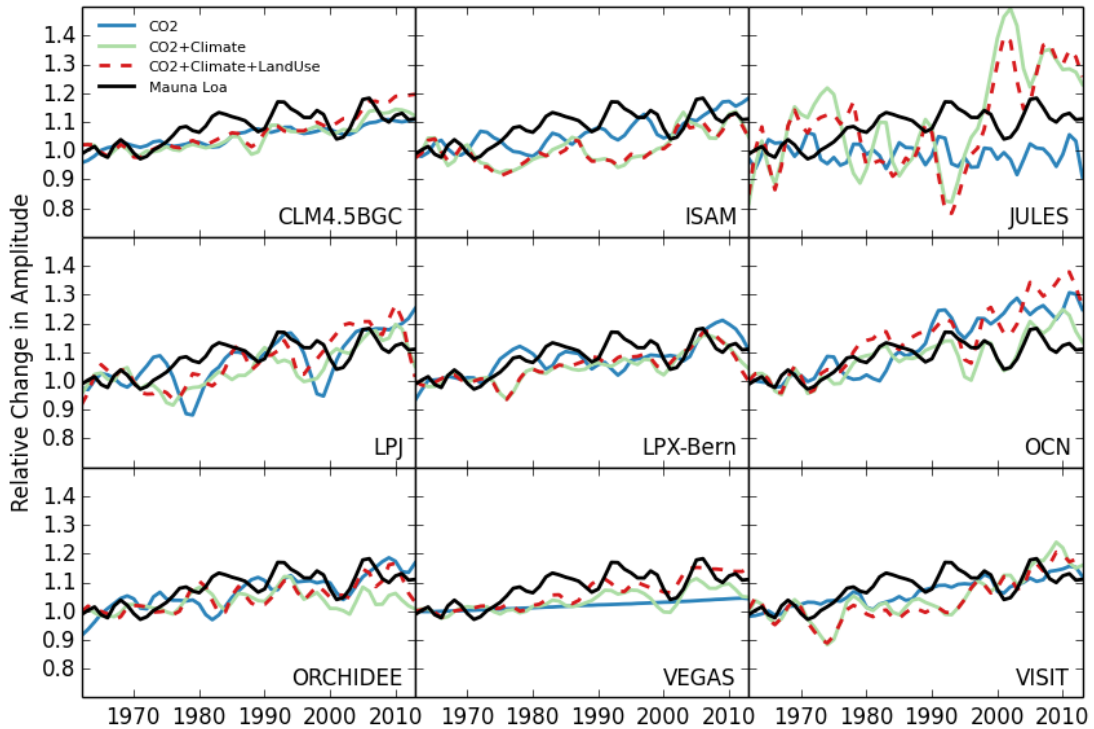


Figure 3-8: Trends for seasonal amplitude of global total net carbon fluxes from S1 (CO₂ only), S2 (CO₂+Climate) and S3 (CO₂+Climate+Land Use/Cover) for each individual TRENDY model. Mauna Loa CO₂ seasonal amplitude is shown for comparison purpose. All amplitude time series are relative to their own 1961-1970 mean amplitude.

Table 3-3: The seasonal amplitude (maximum minus minimum, in PgC y⁻¹) of mean net carbon flux for 2001-2010 relative to the 1961-1970 period, according to the nine TRENDY models (values are listed as percentage change in brackets, for both regions and the entire globe). The four large latitudinal regions are the same as in Figure 3: boreal (50-90N), temperate (23.5-50N), Northern tropics (0-23.5N), Southern tropics (0-23.5S), and Southern extra-tropics (23.5-90S). Values from the two inversions Jena99 and CarbonTracker are also listed for comparison.

Model	Global	Boreal	Northern Temperate	Northern Tropics	Southern Tropics	Southern extra-Tropics
CLM4.5BGC	44.3(15%)	31.9(17%)	19.2(15%)	7.2 (22%)	6.5 (-2%)	4.9(4%)
ISAM	19.1 (9%)	12.1(11%)	7.4(13%)	6.0(1%)	6.9 (-8%)	0.4(4%)
JULES	19.0(26%)	12.2(24%)	14.3(9%)	11.6(0%)	11.3(11%)	2.2(-24%)
LPJ	23.4(26%)	23.0(18%)	14.7(11%)	10.5(9%)	11.8(16%)	2.0(-12%)
LPX-Bern	37.9(15%)	26.9(10%)	19.3(6%)	8.3(9%)	4.6 (-6%)	4.2(15%)
OCN	21.6(34%)	12.3(33%)	11.1(23%)	9.7 (17%)	8.3(3%)	2.0(14%)
ORCHIDEE	39.9(12%)	23.4(14%)	19.1(5%)	22.7(9%)	18.7(2%)	1.4(37%)
VEGAS	46.7(15%)	22.3(17%)	24.7(10%)	4.0 (11%)	3.4 (12%)	2.1(6%)
VISIT	28.9(14%)	22.9(12%)	15.6(8%)	3.4(9%)	3.2(1%)	3.1(18%)
Ensemble	26.1(17%)	18.0(19%)	12.4(15%)	8.0(8%)	4.9(-3%)	2.1(13%)
Jena99	46.8	23.3	21	8.2	8.5	1.5
CarbonTracker	39.9	26.5	16.3	5.3	5.8	2.4

=Attribution of global and regional FTA seasonal amplitude

Similar to the Mauna Loa CO₂ observations, models agree on increase of global F_{TA} seasonal amplitude during 1961-2012 (Figure 3-9). By computing the ratios between amplitude trends from rising CO₂, climate change and land use/cover change with the total trend for each model, we find the effect of varying CO₂, climate and land use/cover contribute to 83±56%, -3±74% and 20±30% to the simulated

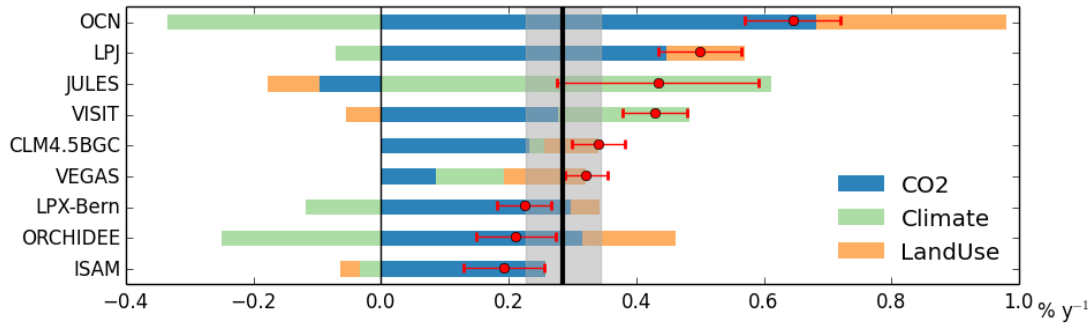


Figure 3-9: Attribution of the seasonal amplitude trend of global net land carbon flux for the period 1961-2012 to three key factors of CO₂, climate and land use/cover. The red dots represent models' global amplitude increase of F_{TA} from the S3 experiment, and error bars indicate 1-σ standard deviation. The increasing seasonal amplitude of F_{TA} is decomposed into the influence of time varying atmospheric CO₂ (blue), climate (light green), and land use/cover change (gold). Also shown is the trend of Mauna Loa CO₂ seasonal amplitude (thick black line) and its 1-σ standard deviation (grey shade) for the same period.

global F_{TA} amplitude increase. All models simulate increasing amplitude for total F_{TA} in the boreal (50-90N) and Northern temperate (23.5-50N) regions, and most models also indicate amplitude increase in the Northern (0-23.5N) and Southern tropics (0-23.5S) (Figure 3-10). There is a less agreement on the sign of amplitude change among the models in the Southern extra-tropics (23.5-90S). Individual model's global and regional trends of F_{TA} amplitude attributable to the three factors (CO₂, climate and land use/cover) are listed in Table 3-4. For most models, latitudinal contribution to global F_{TA} amplitude (computed by the "two-month difference" method) show that the pronounced mid-high latitude maxima in the NH dominate the simulated amplitude increase over 1961-2012 (Figure 3-11, red dashed line for S3 results). All models also indicate a negative contribution from at least part of the Northern temperate region.

Table 3-4: Global and regional attribution of CO₂, climate change and land use/cover change effects on the relative amplitude changes of F_{TA} simulated by the TRENDY models, and the ensemble mean of the relative changes during 1961-2012 period (% y⁻¹). The models are listed in the order of simulated S3 global relative amplitude increase for this period (most to least).

Model	Global				Boreal				Northern Temperate				Northern Tropics				Southern Tropics				Southern extra-Tropics			
	CO ₂	CLIM	LU	ALL	CO ₂	CLIM	LU	ALL	CO ₂	CLIM	LU	ALL	CO ₂	CLIM	LU	ALL	CO ₂	CLIM	LU	ALL	CO ₂	CLIM	LU	ALL
OCN	0.68	-0.33	0.30	0.65	0.50	0.16	0.12	0.78	0.52	-0.18	0.32	0.65	0.16	0.12	0.05	0.34	0.24	0.00	-0.07	0.17	0.52	-0.17	-0.09	0.26
LPJ	0.45	-0.07	0.12	0.50	0.33	-0.04	0.02	0.32	0.02	0.26	0.01	0.29	0.17	0.01	0.00	0.19	0.21	-0.24	0.39	0.36	0.02	-0.05	-0.16	-0.18
JULES	-0.10	0.61	-0.08	0.43	-0.02	0.49	-0.02	0.45	0.09	0.40	-0.17	0.32	0.02	-0.02	-0.07	-0.08	0.12	0.06	0.02	0.20	0.06	-0.30	0.05	-0.19
VISIT	0.28	0.21	-0.05	0.43	0.24	0.16	-0.07	0.33	0.27	-0.06	0.04	0.25	0.27	-0.07	-0.08	0.12	0.02	0.15	-0.06	0.11	0.31	-0.06	0.19	0.44
CLM4.5BGC	0.23	0.02	0.08	0.34	0.16	0.14	0.08	0.38	0.23	-0.03	0.18	0.37	0.22	0.19	0.10	0.50	0.35	-0.28	0.01	0.08	0.07	0.01	0.06	0.14
VEGAS	0.09	0.11	0.13	0.32	0.07	0.19	0.11	0.38	0.11	-0.08	0.22	0.25	0.22	0.27	-0.26	0.23	0.24	0.58	-0.35	0.47	0.11	-0.25	0.23	0.09
LPX-Bern	0.30	-0.12	0.05	0.22	0.20	0.06	0.02	0.28	0.33	-0.25	0.05	0.12	0.19	0.06	0.00	0.24	0.19	0.00	-0.09	0.10	0.23	-0.11	0.20	0.32
ORCHIDEE	0.32	-0.25	0.15	0.21	0.29	-0.12	0.09	0.27	0.31	-0.18	-0.02	0.11	0.18	-0.01	0.09	0.26	0.24	-0.05	-0.10	0.08	0.20	0.42	-0.02	0.60
ISAM	0.26	-0.03	-0.03	0.19	0.32	-0.02	0.00	0.30	0.24	-0.01	-0.01	0.22	0.24	-0.10	-0.06	0.08	0.28	-0.24	-0.11	-0.08	0.22	-0.01	-0.52	-0.31
Ensemble	0.28	0.02	0.07	0.37	0.23	0.11	0.04	0.39	0.24	-0.01	0.07	0.29	0.19	0.05	-0.03	0.21	0.21	0.00	-0.04	0.17	0.19	-0.06	-0.01	0.13

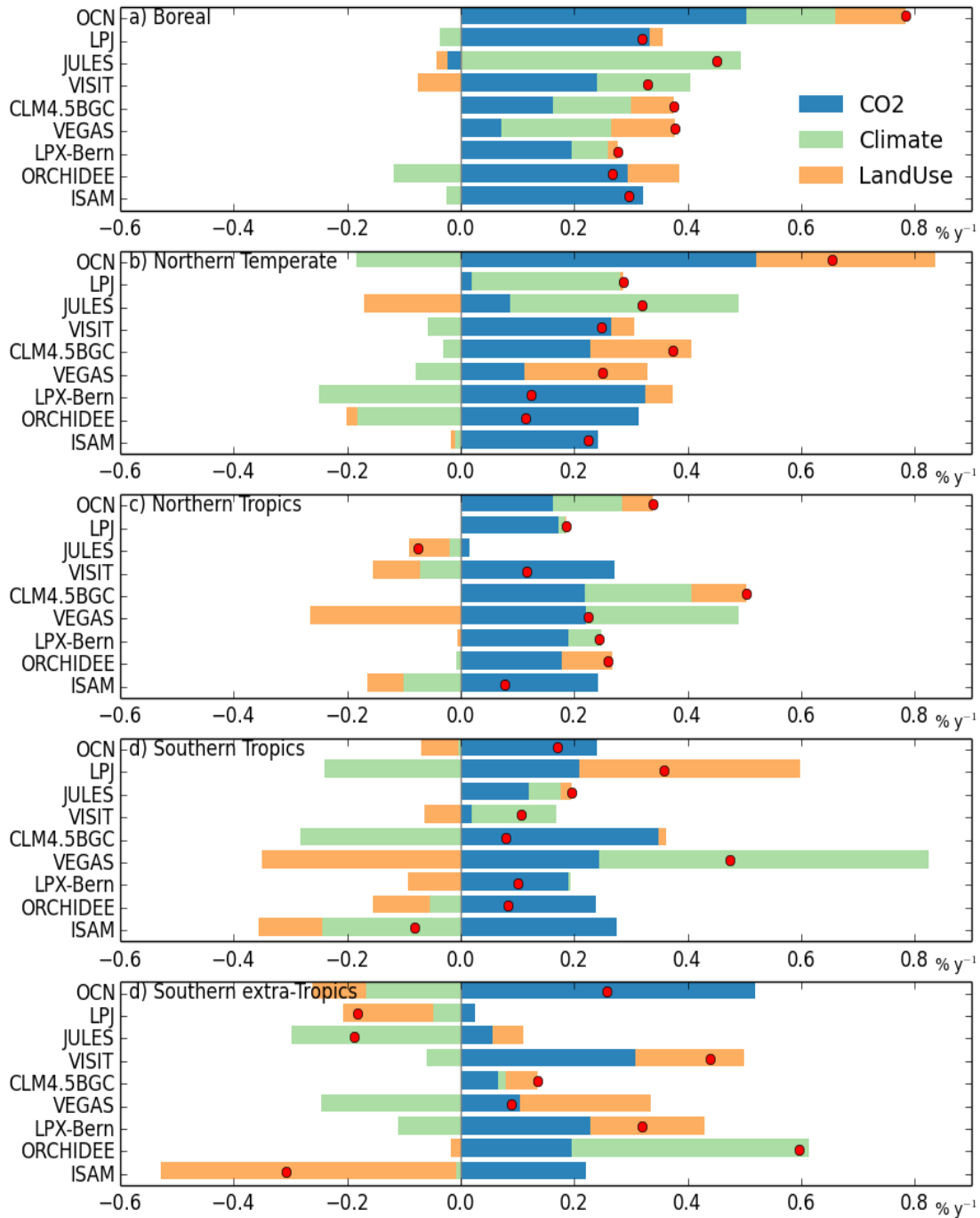


Figure 3-10: Attribution of the seasonal amplitude trend of regional (boreal (50-90N), Northern temperate (23.5-50N), Northern tropics (0-23.5N), Southern tropics (0-23.5S) and Southern extra-tropics (23.5-90S)) net land carbon flux for the period 1961-2012 to three key factors CO₂, climate and land use/cover. The red dots represent models' global amplitude increase of F_{TA} from the S3 experiment. The increasing seasonal amplitude of F_{TA} is decomposed into the influence of time varying atmospheric CO₂ (blue), climate (light green), and land use/cover change (gold).

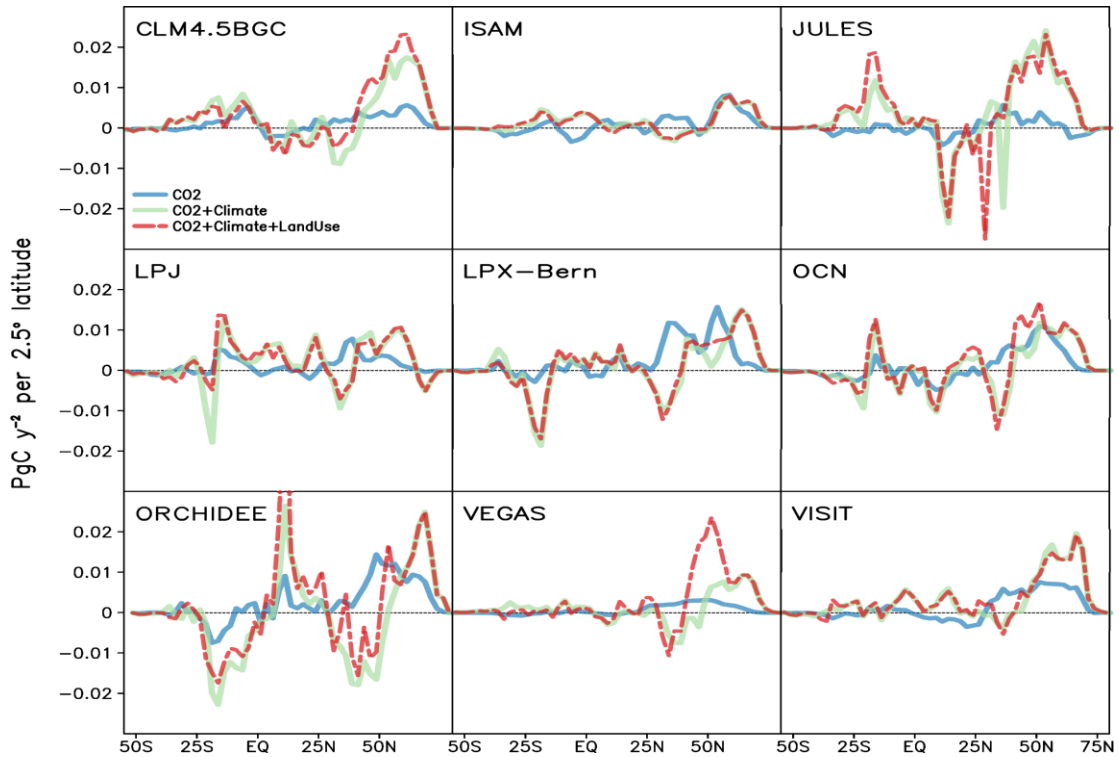


Figure 3-11: Latitudinal contribution of trends for seasonal amplitude of global land-atmosphere carbon flux from TRENDY models in the three sensitivity experiments. Fluxes are summed over each 2.5 ° latitude bands (PgC y^{-1} per 2.5 ° latitude) before computing the “max-min difference” (refer to Methodology section for definition). For each 2.5 ° latitude band, trend is calculated for the period 1961-2012.

The rising CO_2 factor

Seven of the nine models suggest that CO_2 fertilization effect is most responsible for the amplitude increase, while VEGAS attribute it to be approximately equal among the three factors (Figure 3-9). The CO_2 fertilization effect alone appears to cause most of the amplitude increase in a majority of models, with notable contribution from climate change and land use/cover change in CLM4.5BGC and VEGAS (Figure 3-8). The effect of rising CO_2 appears to be slightly negative for JULES, possibly reflecting uncertainty associated with experiment design

(randomized climate is used to drive JULES). For each model, rising CO₂ in the boreal, Northern temperate and the Southern extra-tropics leads to a similar trend (Figure 3-10). The magnitude of this trend may indicate each model's differing strength for CO₂ fertilization. This is possibly due to similar phases of F_{TA} seasonal cycle within the three regions that are mainly driven by climatological temperature contrast. The positive amplitude trend in the carbon flux of the Northern and Southern tropics from CO₂ fertilization is similar, and they likely would cancel out each other because their seasonal cycles are largely out of phase. Latitudinal contribution analyses reveal that trends in the Northern mid-high latitude is the main contributor to global F_{TA} amplitude increase when considering CO₂ fertilization effect alone (Figure 3-11, blue line).

The climate change factor

The effect of climate change on F_{TA} amplitude is mixed: five models (OCN, LPJ, LPX-Bern, ORCHIDEE and ISAM) attribute climate change as a negative factor for the F_{TA} amplitude increase, and four models (JULES, VISIT, CLM4.5BGC and VEGAS) suggest it is a positive effect (Figure 3-9). The high-latitude greening effect is evident in six out of nine models (Figure 3-10), contributing on average 29% of boreal amplitude increase. The latitudinal contribution analyses (Figure 3-11) also suggest that warming induced high latitude “greening” effect is present in all models, but this positive contribution only exhibits a wide range of influence in about half of the models (CLM4.5BGC, JULES, VEGAS and VISIT). The latitudinal patterns also reveal that, once climate change is considered, the contribution from the Northern temperate region around 40N shifts to negative in all models. In the Northern

temperate (23.5-50N) region, climate change alone would decrease the F_{TA} amplitude except for JULES and LPJ (Figure 3-10), possibly related to mid-latitude drought (Buermann et al., 2007). This is consistent with findings by (Schneising et al., 2014), who observed a negative relationship between temperature and seasonal amplitude of xCO_2 from both satellite measurements and CarbonTracker during 2003-2011 for the Northern temperate zone. The negative contribution from the temperate zone counteracts the positive boreal contribution, suggesting the net impact from climate change on F_{TA} amplitude may not be as significant as previously suggested. With changing climate introduced, some models' global F_{TA} amplitude generally mirror the decadal variability in the amplitude of Mauna Loa CO_2 observations, including the decline in the 1990s (Figure 3-8). OCN and ORCHIDEE appear to be especially sensitive to the climate variations after the 1990s, resulting a decrease in F_{TA} amplitude. It is also apparent from the time series figure that the strong increasing trend of F_{TA} amplitude from climate change in JULES is mostly due to the sharp rise from early 1990s to early 2000s, suggesting some possible model artifact (Figure 8). The effect of climate change is more mixed in both tropics and the Southern extra-tropics.

The land use/cover change factor

Six of the nine models show that land use/cover change leads to increasing global F_{TA} amplitude (Figure 3-9). Land use/cover change appears to amplify F_{TA} seasonal cycle in boreal and Northern temperate regions for most models. For some models (VEGAS, CLM4.5BGC and OCN), this effect is especially pronounced in the Northern temperate region where most of the global crop production takes place

(Figure 3-10). Note that the effect of land use/cover change includes two parts: one is the change of land use practice without changing the land cover type; the other is the change of land cover, including crop abandonment etc. VEGAS simulates time-varying management intensity and crop harvest index, which is an example of significant contribution from land use change (Zeng et al., 2014). For many other models, land cover change is possibly the more important factor. During 1961-2012, large cropland areas were abandoned in the Eastern U.S. and central Europe, often followed by forest regrowth. New cropland expanded in the tropics and South America, Midwest U.S., East and central North Asia and the Middle East. How such change affect the global F_{TA} amplitude is determined by the productivity and seasonal phase of the old and new vegetation covers. For CLM4.5BGC, JULES, LPJ and ORCHIDEE, enhanced vegetation activity from growing forest in these regions contribute positively to global F_{TA} amplitude increase (Figure 3-12). In contrast, for LPX-Bern, VISIT, and VEGAS in the Eastern U.S., loss of cropland leads to decrease in the amplitude. Additional cropland in the Midwest U.S. and East and central North Asia contribute negatively to F_{TA} amplitude trend for JULES, LPJ and ORCHIDEE. These regions however, are major zones contributing the amplification of global F_{TA} for LPX-Bern, OCN, VEGAS and VISIT. One mechanism mentioned previously is agricultural intensification: in fact, CO_2 flux measurements over corn fields in the U.S. Midwest show much larger seasonal amplitude than over nearby natural vegetation (Miles et al., 2012). Another plausible mechanism is irrigation, which can alleviate adverse climate impact from droughts, and crops may have a stronger seasonal cycle than the natural vegetation they replace in these regions. The overall

effect of land use/cover change for each model therefore, is often the aggregated result over many regions that can only be revealed by spatially explicit patterns. When examining the latitudinal contribution only (Figure 3-11), CLM4.5BGC, LPX-Bern, OCN and VEGAS are quite similar, even though the spatial pattern reveal CLM4.5BGC is very different from the other three models (Figure 3-12). For JULES, LPJ and ORCHIDEE a significant part of land use/cover change contribution comes from the tropical zone (Figure 3-11).

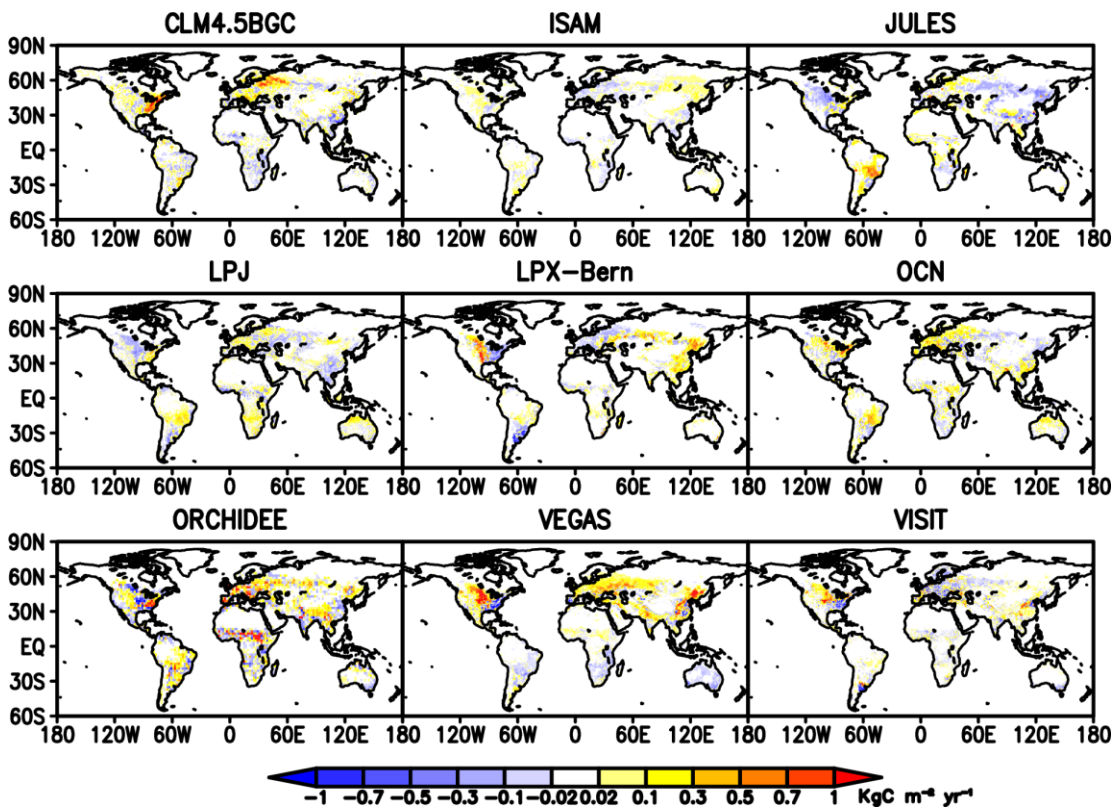


Figure 3-12: Contribution from land use/cover change on trends in the seasonal amplitude of global land-atmosphere carbon flux. For each spatial grid, the trend is computed as trends of the “max-min difference” (refer to Methodology section for definition) in the S2 experiment (changing CO₂ and climate) subtracted by trends in S1 (changing CO₂ only).

Discussion and conclusion

Our results show a robust increase of global and regional (especially over the boreal and Northern temperate regions) F_{TA} amplitude simulated by all TRENDY models. During 1961-2012, TRENDY models' ensemble mean global F_{TA} relative amplitude increase ($19 \pm 8\%$) is found to be comparable with the CO_2 amplitude increase ($15 \pm 3\%$) at Mauna Loa. Additionally, their decadal variability generally agrees well. This amplitude increase mostly reflects the earlier and deeper drawdown of CO_2 in the NH growing season. The models in general, especially the multi-model median, also simulate latitudinal patterns of F_{TA} mean amplitude that is similar with the atmospheric inversions results. Their latitudinal patterns capture the temperature driven seasonality from the NH mid-high latitude region and the two monsoon driven subtropical maxima, although the magnitude or extent vary. Despite the general agreements between the models' ensemble amplitude increases and the limited observation-based estimates, considerable model spread are noticeable. Five of the nine models considerably underestimate the global mean F_{TA} seasonal cycle compared to atmospheric inversions, and peak carbon uptake takes place one or two months too early in seven of the nine models. The seasonal amplitude of model ensemble global mean F_{TA} is 40% smaller than the amplitude of the atmosphere inversions. In contrast to the divergence in simulated seasonal carbon cycle, atmospheric inversions in Northern temperate and boreal regions are well constrained: 11 different inversions agree on July F_{TA} minimum in the Northern Hemisphere (25-90N), with no more than 20% difference in amplitude (Peylin et al., 2013).

The simulated amplitude increase is found to be due to a larger F_{TA} minimum associated with a stronger ecosystem growth. Over the historical period, global mean carbon sink is also increasing over time, suggesting a possible relationship between seasonal amplitude and the mean sink (Randerson et al., 1997; Zhao and Zeng, 2014; Ito et al., 2015). For the nine models, we found a moderate relationship between enhanced mean land carbon sink and the seasonal amplitude increase similar to reported results by in Zhao and Zeng (2014), with an R-squared value of 0.61 (Figure 3-13). However, no clear relationship is found between mean land carbon sink and F_{TA} seasonal amplitude. Models with a strong mean carbon sink (for example JULES and OCN) have relatively weak seasonal amplitude, and the LPX-Bern model shows no carbon sink despite having a strong F_{TA} seasonality. The 2014 Global Carbon Budget report (Le Quéré et al., 2015) estimated a total land carbon sink of 1.5 ± 0.6 PgC y^{-1} from carbon budget analyses (fossil fuel emission minus atmospheric growth rate minus ocean carbon sink), and only four models (JULES, OCN, VEGAS and VISIT) are within the uncertainty range of this budget-based analysis. In spite of their similar mean land carbon sink, the shape of their F_{TA} seasonal cycle differs. While VEGAS also shows a similar seasonal carbon cycle compared to inversions, the other three models exhibit an unrealistically long growing season with half the amplitude as the inversions. July and August are the only two months with net carbon release for JULES, whereas OCN and VISIT both have a long major growing season from May to September. Given that the mean F_{TA} seasonal cycle is relatively well constrained, insights gained from analyzing modeled seasonal amplitude of carbon flux may help to understand the considerable model spread found in the mean global carbon sink for

the historical period (Le Qu  r   et al., 2015), which is possibly due to varied model sensitivity to different mechanisms (Arora et al., 2013). Examining details of models' mechanical difference could also help to better assess the different future projections on both the magnitude and direction of global carbon flux (Friedlingstein et al., 2006, 2013).

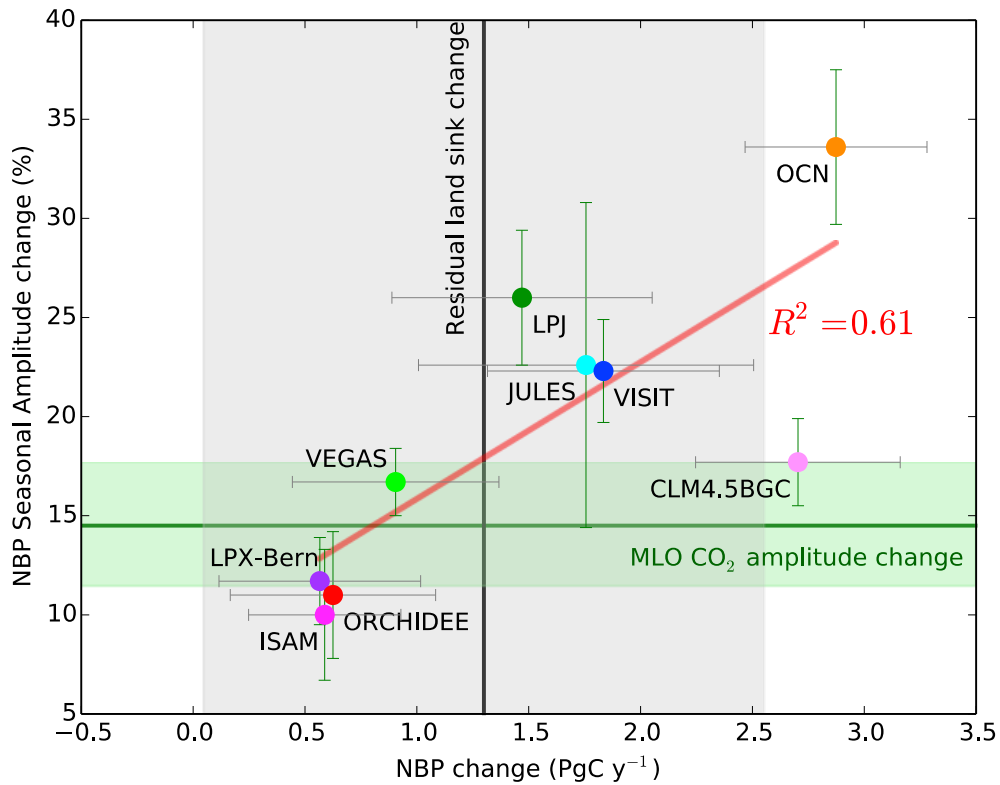


Figure 3-13: Relationship between the increase in net biosphere production (NBP, equal to $-F_{TA}$) and increase in NBP seasonal amplitude (as in Figure 4's red dots), for 1961-2012 period for nine TRENDY models. Error bars indicate the standard errors of the trend estimates. Amplitude increase and associated standard deviation in Mauna Loa CO₂ is plotted in green horizontal line and shade, respectively. Increase in residual land sink is estimated by taking the difference between two residual land sinks, over 2004-2013 and 1960-1969 (an interval of 44 years), as reported in Le Qu  r   et al. (2015). This difference is then scaled by 52/44 (to make it comparable with models' NBP change for this figure), which is displayed in black vertical line and shade (error add in quadrature, assuming Gaussian error for the two decadal residual land sinks, then also scaled). The cross-model correlation ($R^2=0.61$, $p < 0.05$) suggests that a model with a larger net carbon sink increase is likely to simulate a higher increase in NBP seasonal amplitude.

Compared to earlier studies, this study performed most detailed analyses of the TRENDY factorial experiments results to date. Unlike many previous studies that focused on comparing season cycle at individual CO₂ monitoring stations (Randerson et al., 1997; Peng et al., 2015), we studied the global and large latitudinal bands. Such quantities often demonstrate well-constrained seasonality that is relatively robust against uncertainty from atmospheric transport, fossil fuel emission, biomass burning etc.. We found greater uncertainty is found for the tropics and Southern extra-tropics regions where atmospheric CO₂ observations are relatively sparse. Tropical ecosystems are also heavily affected by biomass burning, however the models used in this study may have differently employed (or omitted) fire dynamics. For models that do have fire simulation/suppression, they may not be driven by observed fire data, making their results less comparable with observation-based estimates. These uncertainties however, are unlikely to affect our main conclusions because of limited contribution of tropics to global F_{TA} amplitude increase. Another possibly important factor is the impact from increased nitrogen deposition, which may have been include in the “CO₂ fertilization” effect for some models with full nitrogen cycle (Table 3-1), however this can only be explored in future studies, as the TRENDY experiment design does not separated out the nitrogen contribution.

Our factorial analyses highlight differential control from rising CO₂, climate change and land use/cover change among the models, with seven out of nine models indicating major contribution ($83 \pm 56\%$) to global F_{TA} amplitude increase from the CO₂ fertilization effect. The strength of CO₂ fertilization varies among models, but for each model its magnitude in the boreal, Northern temperate and Southern extra-

tropics regions is similar. Models are split regarding the role of climate change, as compared with the models ensemble mean ($-3 \pm 74\%$). Regional analyses show that climate change amplifies the boreal F_{TA} seasonal cycle but weakens the seasonal cycle for other regions according to most models. By examining latitudinal trends from the “max-min difference”, we found all models indicate a negative climate contribution over the mid-latitudes, where droughts might have reduced ecosystem productivity. This negative effect offsets the high latitude “greening” over high latitudes, which in some models result in a net negative climate change impact on global F_{TA} amplitude. Such mechanism cast doubt on whether climate change is the main driver of the global F_{TA} amplitude increase. Land use/cover change, according to a majority of the models, appears to amplify the global F_{TA} seasonal cycle ($20 \pm 30\%$), however the mechanisms seem to differ for different models. Conversion to/from cropland could either increase or decrease the seasonal amplitude, depending on how models simulate the seasonal cycle of cropland compared to natural vegetation it replaces/precedes. For the same pattern of increasing amplitude, the underlying causes could include irrigation that mitigates negative climate effect, agricultural management practices and other mechanisms.

Overall, F_{TA} seasonal cycle and its amplitude are effective indicators for diagnosing model sensitivity to various mechanisms in different regions. With limited observations, such detailed utilization can provide additional constraints for the terrestrial biosphere models, in addition to the residual land carbon sink and its interannual and decadal variabilities. Future efforts are required to improve the seasonal cycle simulation, by realistically representing the strength of relevant

mechanisms and incorporating the missing processes. Expanding observations from satellite, flight campaigns, flux towers and CO₂ monitoring stations provide increasing insights on seasonal characteristics of terrestrial ecosystems such as plant phenology. Large-scale campaigns like the Next-Generation Ecosystem Experiments (NGEE) in the arctic and tropics may hopefully reduce large uncertainty in understanding the role of ecosystems for these key regions. Progresses in model development, observational records and advanced analyses techniques would likely reduce uncertainty from the model ensemble and increase our confidence in their land carbon sink projections.

Supplementary figures

Similar to Figure 3-12, spatial patterns of S1, S2-S1 and S3 experiments are displayed here as supplementary figures, because the main features are similar to the latitudinal contribution figure 3-11, unlike the land use/cover change spatial plot. These figures are all computed using the “two-month difference” method.

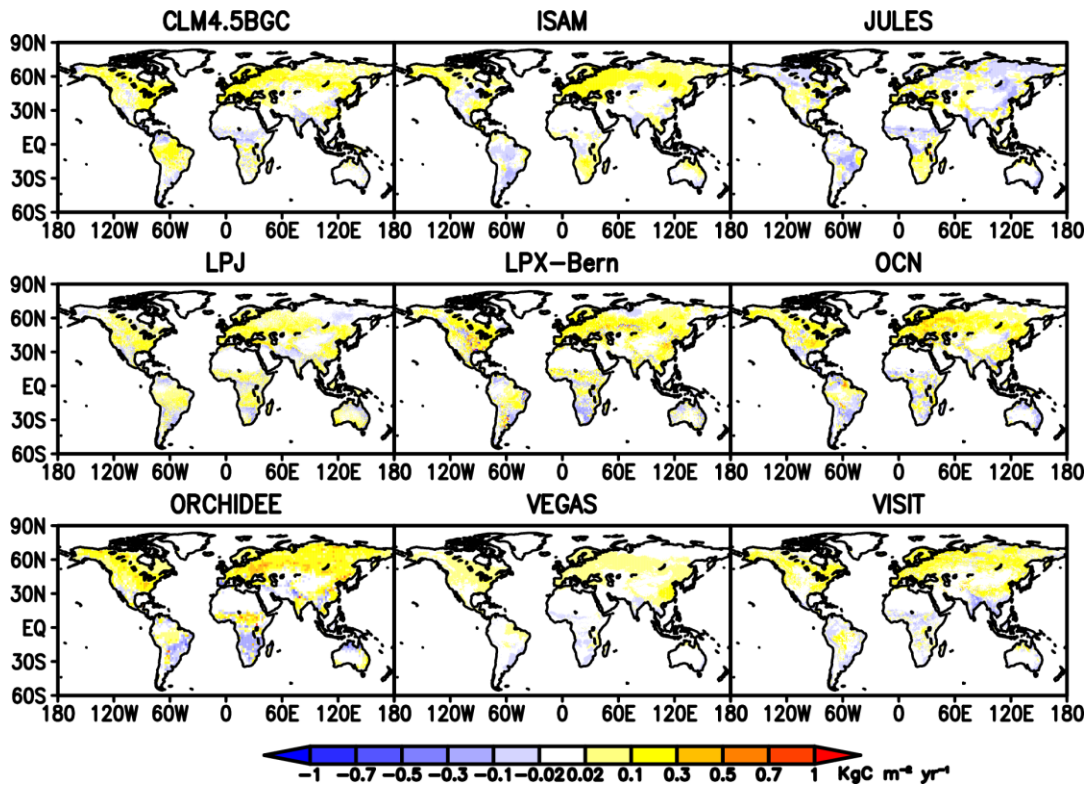


Figure 3-S1: Contribution of trends for seasonal amplitude of global land-atmosphere carbon flux for each TRENDY model in the S1 experiment (changing CO₂ only). Trends are calculated for the period 1961-2012 for the “two-month difference” (refer to Methodology section for definition).

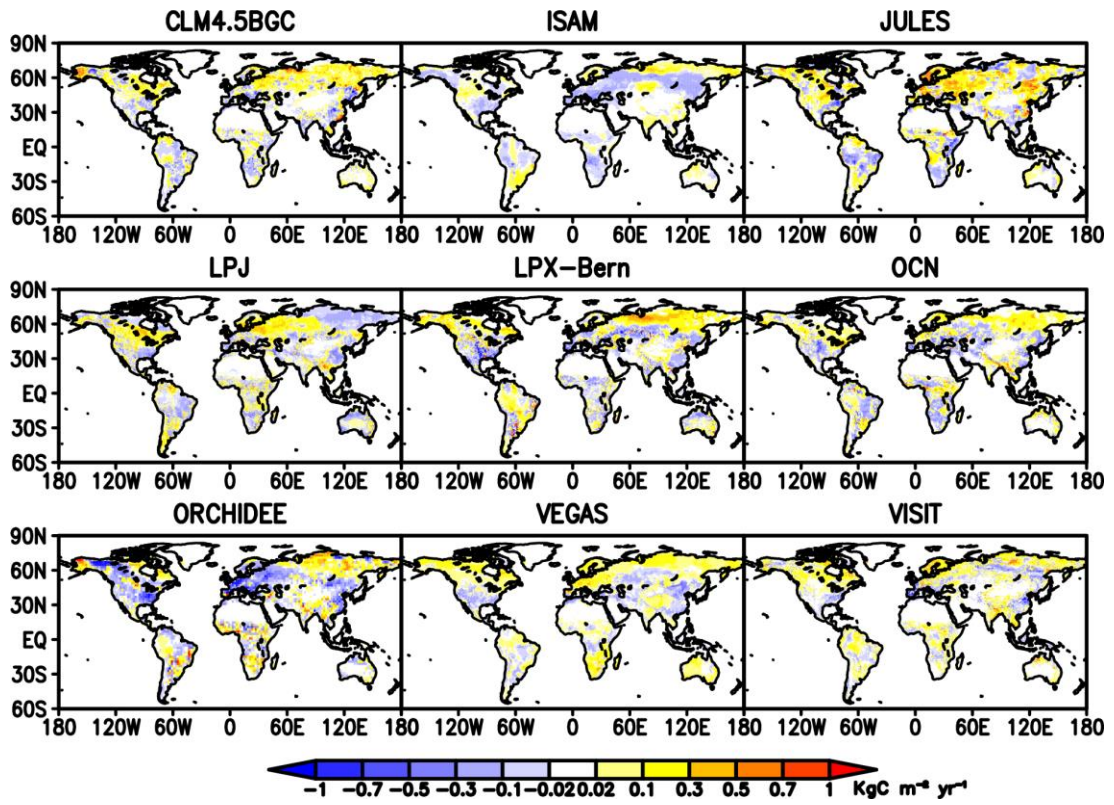


Figure 3-S2: Similar as Figure 3-S1, but for trends in the S2 experiment (changing CO₂ and climate) subtracting trends in S1, therefore representing effect of climate change with the linear assumption.

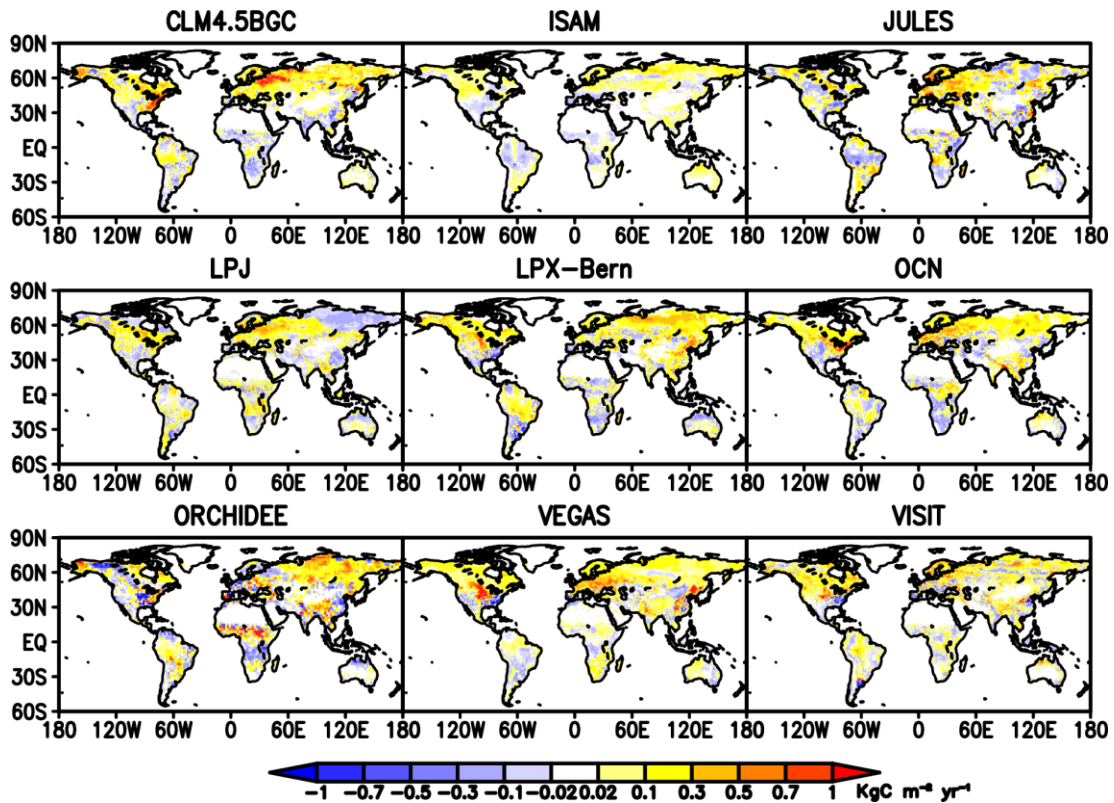


Figure 3-S3: Similar as Figure 3-S1, but for trends in the S3 experiment (changing CO₂, climate and land use/cover).

Appendix

A. Environmental drivers for TRENDY

For observed rising atmospheric CO₂ concentration, the models use a single global annual (1860-2012) time series from ice core (before 1958: Joos and Spahni, 2008) and the National Oceanic and Atmospheric Administration (NOAA)'s *Earth System Research Laboratory* (after 1958: monthly average from Mauna Loa and South Pole CO₂, south pole data is constructed from the 1976-2014 average if not available). For climate forcing, the models employ 1901-2012 global climate data from the Climate Research Unit (CRU, version TS3.21, <http://www.cru.uea.ac.uk>) at monthly (or interpolate to finer temporal resolution for individual models) temporal

resolution and $0.5^\circ \times 0.5^\circ$ spatial resolution. For land use/cover change history data, the models adopt either gridded yearly cropland and pasture fractional cover from the History Database of the Global Environment (HYDE) version 3.1 (<http://themasites.pbl.nl/tridion/en/themasites/hyde/>, Klein Goldewijk et al., 2011), or the dataset including land use history transitions from L. Chini based on the HYDE data.

B. Environmental drivers for TRENDY

The Jena inversion is from the Max Planck Institute of Biogeochemistry, v3.7 at $5^\circ \times 5^\circ$ spatial resolution (<http://www.bgc-jena.mpg.de/~christian.roedenbeck/download-CO2/>, Rodenbeck et al., 2003), including two datasets abbreviated as Jena81 for the period of 1981–2010 using CO₂ data from 15 stations, and Jena99 using 61 stations for 1999–2010. Another inversion-based dataset used is the CarbonTracker, version CT2013B from NOAA/ESRL at $1^\circ \times 1^\circ$ spatial resolution (<http://www.esrl.noaa.gov/gmd/ccgg/carbontracker/>, Peters et al., 2007) for the period of 2000–2010, which integrates flask samples from 81 stations, 13 continuous measurement stations and 9 flux towers, and the surface fluxes from land and ocean carbon models as prior fluxes. These two inversion-based datasets are vastly different in their approach in inversion algorithm, choice of atmospheric data, transport model and prior information (Peylin et al., 2013). For example, to minimize the spurious variability introduced by changes in availability of observations through examine period, the Jena inversion provides multiple versions with different record length, each only use records covering its full period (for example, Jena99 includes more

stations than Jena81, but with a shorter period). The CarbonTracker however, opt for assimilating all quality-controlled data (with outliers removed) favoring a higher spatial resolution in estimated carbon fluxes. Therefore, we chose these two inversions to capture to some extent the uncertainty in atmospheric inversions.

Acknowledgement

This study was funded by NOAA, NASA and NSF. Partial financial support for this study was also provided by a Pacific Northwest National Laboratory Directed Research and Development project. We thank the TRENDY coordinators and participating modeling teams, NOAA ESRL, and Jena/CarbonTracker inversion teams.

Chapter 4: Continued increase in atmospheric CO₂ seasonal amplitude in the 21st century projected by the CMIP5 Earth system models

Preface

Fang Zhao¹ and Ning Zeng^{1,2}

¹Department of Atmospheric and Oceanic Science, University of Maryland, USA

²Earth System Science Interdisciplinary Center, University of Maryland, USA

Published in:

Earth System Dynamics (2014) 5, 423-439

Abstract

In the Northern Hemisphere, atmospheric CO₂ concentration declines in spring and summer, and rises in fall and winter. Ground-based and aircraft-based observation records indicate that the amplitude of this seasonal cycle has increased in the past. Will this trend continue in the future? In this paper, we analyzed simulations for historical (1850-2005) and future (RCP8.5, 2006-2100) periods produced by 10 Earth System Models participating in the Fifth Phase of the Coupled Model Intercomparison Project (CMIP5). Our results present a model consensus that the increase of CO₂ seasonal amplitude continues throughout the 21st century. Multi-model ensemble relative amplitude of detrended global mean CO₂ seasonal cycle increases by $62 \pm 19\%$ in 2081-2090, compared to 1961-1970. This amplitude increase

corresponds to a $68 \pm 25\%$ increase in Net Biosphere Production (NBP). The results show that the increase of NBP amplitude mainly comes from enhanced ecosystem uptake during Northern Hemisphere growing season under future CO₂ and temperature conditions. Separate analyses on Net Primary Production (NPP) and respiration reveal that enhanced ecosystem carbon uptake contributes about 75% of the amplitude increase. Stimulated by higher CO₂ concentration and high-latitude warming, enhanced NPP likely outcompetes increased respiration at higher temperature, resulting in a higher net uptake during the Northern growing season. The zonal distribution and spatial pattern of NBP change suggest that regions north of 45 °N dominate the amplitude increase. Models that simulate a stronger carbon uptake also tend to show a larger increase of NBP seasonal amplitude, and the cross-model correlation is significant ($R=0.73$, $p<0.05$)

Introduction

Modern measurements at Mauna Loa, Hawaii (19.5 °N, 155.6 °W, 3400m altitude) have shown an increase in atmospheric CO₂ concentration from <320 ppm in 1958 to 400 ppm in 2013. There is also a mean seasonal cycle that is characterized with a 5-month decrease (minimum in October) and a 7-month increase (maximum in May). The peak-to-trough amplitude of this seasonal cycle is approximately 6.5 ppm, which represents a close average of a large portion of the Northern Hemisphere (NH) biosphere (Kaminski et al., 1996) where the amplitude ranges from about 3 ppm near the Equator to 17 ppm at Point Barrow, Alaska (71 °N). The seasonal variation of Mauna Loa (MLO) CO₂ reflects the imbalance of growth and decay of the NH

biosphere. Early studies have speculated that global primary production would decrease because of global changes such as acid rain and deforestation (Reiners, 1973; Whittaker and Likens, 1973). If this is the case, assuming changes in respiration are similar at peak and trough of the CO₂ seasonal cycle, we might observe a reduction of CO₂ seasonal amplitude. However, Hall et al. (1975) found no evidence of long-term amplitude change from 15 years of MLO CO₂ record (1958-1972). They concluded that either the biosphere is too big to be affected yet or the degradation of biosphere is balanced by enhanced CO₂ fertilization and increased use of fertilizers in agriculture.

In 1970s through 1980s, the metabolic activity of the biosphere seems getting stronger, as indicated by rapid increase in MLO CO₂ amplitude (Pearman and Hyson, 1981; Cleveland et al., 1983; Bacastow et al., 1985). Enhanced CO₂ fertilization was considered as a major factor, and climate change a possible cause (Bacastow et al., 1985). Keeling et al. (1996) linked the amplitude increase with climate change by showing the two-year phase lag relationship between trends of CO₂ amplitude and 30-80 °N mean land temperature. Unlike CO₂ fertilization, the combined effect of climate (temperature, precipitation, etc.) introduces strong interannual variability to the CO₂ amplitude change. In the early 1990s, despite of the continuing rise of 30-80 °N mean land temperature, CO₂ seasonal amplitude at MLO has declined. Buermann et al. (2007) attributed this decline to the severe drought in North America during 1998-2003.

In late 1990s, the increasing trend resumed at MLO. The latest analysis shows a 0.32% yr⁻¹ increase in MLO amplitude and a 0.60% yr⁻¹ increase in Point Barrow

(BRW) amplitude (Figure 1A in Graven et al., 2013). This trend (over 50 years) corresponds to an increase of 16% in MLO, and 30% in BRW CO₂ seasonal amplitude, respectively. Graven et al. (2013) also compared aircraft measurements taken at 500hPa and 700hPa heights in 1958–1961 and 2009–2011, suggesting an even larger (~50%) increase of CO₂ seasonal amplitude north of 45 °N. Furthermore, to infer the model-simulated CO₂ amplitude increase at 500hPa, they applied two atmospheric transport models to monthly Net Ecosystem Production (NEP) from the historical simulation (Exp3.2) results of eight CMIP5 models. Compared with aircraft data, they found the CMIP5 models simulated a much lower amplitude increase.

Surface CO₂ monitoring stations have two major limitations. First, they are sparse. For several decades, the Global Monitoring Division of NOAA/Earth System Research Laboratory (ESRL) has measured CO₂ from >100 surface monitoring sites (Conway et al., 1994). Only some have over 30 years of record. Similarly, Randerson et al. (1997) determined the CO₂ amplitude trend north of 55 °N by averaging flask data from five stations. Second, the surface CO₂ stations do not measure carbon exchange between the land/ocean and atmosphere directly. Atmospheric inversion models are capable of providing surface carbon fluxes with global coverage. However, the resolution and accuracy of these models are inherently limited due to a small number of stations used, and errors in atmospheric transport (Peylin et al., 2013).

Process-based Terrestrial Biosphere Models (TBMs) can generate surface fluxes over the past for longer period, usually with a spatial resolution of half to three degrees. Thus, they offer opportunities to understand the mechanisms of CO₂

amplitude increase better. McGuire et al. (2001) calculated amplitude trends of total land-atmosphere carbon flux (north of 30 °N) from four TBMs. Compared to Mauna Loa CO₂, they found the trend was overestimated by one of the four models and underestimated by the other three. They suggest the observed trend may be a consequence of the combined effects of rising CO₂, climate variability and land use changes, which has also been recognized in previous studies (Kohlmaier et al., 1989; Keeling et al., 1995, 1996; Randerson et al., 1997, 1999; Zimov et al., 1999). Models show varied extent of amplitude increase, possibly due to their different sensitivities to CO₂ concentration and climate. Interestingly, Graven et al. (2013) found that CMIP5 models underestimate the CO₂ amplitude increase in the mid-troposphere at latitudes north of 45 °N. However, previous observations indicated that the models might overestimate CO₂ fertilization effect (Piao et al., 2013), suggesting that our understanding of the amplitude trend is still limited.

In the future, we do not know if the CO₂ amplitude will increase or decrease. With temperature rise and CO₂ increase, we may see a further increase of CO₂ amplitude. On the other hand, the frequency and/or duration of heat waves are very likely to increase over most land areas, and the increases in intensity and/or duration of drought and flood are likely (International Panel on Climate Change, 2013). As a result, the ecosystem productivity may decrease, which may reduce the CO₂ amplitude. In this study, we analyzed the fully coupled CMIP5 earth system model runs as part of the Fifth Assessment Report (AR5) of the United Nations' Intergovernmental Panel on Climate Change (IPCC). Specifically, we looked into the emission-driven simulations, which include many of the aforementioned processes

and feedbacks. Our specific questions are: 1). How do the CMIP5 models predict the amplitude and phase changes of CO₂ seasonal cycle in the future? 2). Are the changes mostly driven by changes in ecosystem production or respiration? 3). Where do the models predict the largest CO₂ amplitude changes will occur?

Method

Model descriptions

We analyzed historical and future emission-driven simulation results from 10 CMIP5 ESMs. The historical simulations, referred to as experiment 5.2 or ESM historical 1850-2005 run (Taylor et al., 2012), were forced with gridded CO₂ emissions reconstructed from fossil fuel consumption estimates (Andres et al., 2011). The future simulations, referred to as experiment 5.3 or ESM RCP8.5 2006-2100 run, were forced with projected CO₂ emissions, following only one scenario—RCP8.5 (Moss et al., 2010). We chose the emission-driven runs because the fully coupled ESMs in these runs have interactive carbon cycle component. Global atmospheric CO₂ concentrations are simulated prognostically, therefore they reflect the total effect of all the physical, chemical, and biological processes on Earth, and their interactions and feedbacks with the climate system. We obtained model output primarily from the Earth System Grid Federation (ESGF), an international network of distributed climate data servers (Williams et al., 2011). For the GFDL model, we retrieved results from its Data Portal (<http://nomads.gfdl.noaa.gov:8080/DataPortal/cmip5.jsp>). The main characteristics of the 10 models are listed in Table 4-1.

Table 4-1: List of Models used and their characteristics

Models	Modeling Center	Land Component	Resolution (Lon × Lat)	Reference
BNU-ESM	Beijing Normal University, China	CoLM3	2.8125° × 2.8125°	Ji et al. (2014)
CanESM2	Canadian Centre for Climate Modeling and Analysis, Canada	CTEM	2.8125° × 2.8125°	Arora et al. (2011)
CESM1-BGC	Community Earth System Model Contributors, NSF-DOE-NCAR, USA	CLM4	1.25° × 0.9°	Long et al. (2013)
GFDL-ESM2m	NOAA Geophysical Fluid Dynamics Laboratory, USA	LM3	2.5° × 2°	Dunne et al. (2013)
INM-CM4	Institute for Numerical Mathematics, Russia		2° × 1.5°	Volodin et al. (2010)
IPSL-CM5A-LR	Institut Pierre-Simon Laplace, France	ORCHIDEE	3.75° × 1.875°	Dufresne et al. (2013)
MIROC-ESM	Japan Agency for Marine-Earth Science and Technology, Atmosphere and Ocean Research Institute (University of Tokyo), and National Institute for Environmental Studies, Japan	MATSIRO + SEIB-DGVM	2.8125° × 2.8125°	Watanabe et al. (2011)
MPI-ESM-LR	Max Planck Institute for Meteorology, Germany	JSBACH	2.8125° × 2.8125°	Ilyina et al. (2013)
MRI-ESM1	Meteorological Research Institute, Japan	HAL	1.125° × 1.125°	Yukimoto et al. (2011)
NorESM1-ME	Norwegian Climate Centre, Norway	CLM4	2.5° × 1.875°	Tjiputra et al. (2013)

Analysis procedure

We first analyzed the monthly output of prognostic atmospheric CO₂ concentrations to evaluate the change of CO₂ seasonal amplitude (defined as maximum minus minimum of detrended seasonal cycle) from 1961 to 2099.

Atmospheric CO₂ was obtained primarily as the area- and pressure-weighted mean of CO₂ across all vertical levels—a better representation of atmospheric carbon content than surface CO₂. The INM-CM4 model does not provide CO₂ concentration, so we converted its total atmospheric mass of CO₂ to mole fraction. We excluded the IPSL model from analyses in Section 3.1 and 3.2 because its CO₂ output is not available. Only CanESM2 provides three different realizations for both historical and future runs, and we simply use its first realization in our comparison. We believe this choice would lead to a more representative result than including all realizations of CanESM2 in multi-model averaging.

To extract the CO₂ seasonal cycle from the monthly records, we applied the curve-fitting procedures using the CCGCRV software developed at the National Oceanic and Atmospheric Administration Climate Monitoring and Diagnostics Laboratory (Thoning et al., 1989; <http://www.esrl.noaa.gov/gmd/ccgg/mbl/crvfit/crvfit.html>). This algorithm first fits the long-term variations and the seasonal component in the monthly CO₂ record with a combination of a trend function and a series of annual harmonics. Then the residuals are filtered with fast Fourier transform and transformed back to the real domain. Specifically, we followed the default setup of a quadratic polynomial for the trend function, a four-yearly harmonics for the seasonal component, and long/short-term cutoff values of 667 days/80 days for the filtering in our analyses. We examined the phase change of CO₂ detrended seasonal cycle by counting how frequent the maxima and minima occur in different months. We used two definitions of seasonal amplitude in our analyses that yield similar results: one directly comes from the CCGCRV package, and another definition is

simply maximum minus minimum of detrended seasonal cycle in each year. For each model's monthly global mean CO₂, we first computed the detrended CO₂ seasonal cycle as the annual harmonic part plus the filtered residue using the short-term cutoff value. Then we started to investigate the global carbon budget in each model:

$$\frac{dCO_2}{dt} = FFE - NBP + FOA \quad (1)$$

The left term is the change of CO₂ concentration (or CO₂ growth rate), which we simply computed as the difference between the current month and previous month's concentration—this leads to a half-month shift earlier than the results indicate. The right hand side (RHS) comprises of fossil fuel emission (FFE), net biosphere production (NBP, or net terrestrial-atmosphere carbon exchange, positive if land is a carbon sink) and net ocean-atmosphere flux (FOA, positive if ocean releases carbon). For each model, we checked and ensured that the sum of individual flux terms on the RHS of equation (1) equals to the CO₂ growth rate.

Previous studies have limited the impact of FFE and FOA on trends in CO₂ amplitude to less than a few percent change (Graven et al. 2013). Therefore we focused on examining the seasonal cycle of NBP in this study. To investigate whether the NBP amplitude change is mostly due to enhanced production or respiration, we inspected the seasonal cycle of NPP and respiration separately. The INM model does not provide NPP output, so it is excluded in this part of analyses. For respiration, one complication is that, even though NBP represents the net terrestrial-atmosphere carbon exchange in all models (thus allowing model comparison), its further breakdown varies. For example, the GFDL-ESM2M model's NBP has component fluxes including NPP, heterotrophic respiration (Rh), land use change (fLuc), fire

(fFire), harvest (fHarvest) and grazing (fGrazing). In contrast, NBP approximately equals to NPP minus Rh in CanESM2. Instead of directly adding all flux components such as Rh and fLuc for each model (which would be unnecessary and difficult since not all fluxes are provided), we defined R_h^* (dominated by Rh) such that

$$R_h^* = NPP - NBP \quad (2)$$

Additionally, we analyzed the spatial patterns of NBP change between future (2081-2090) and historical (1961-1970) period. We approximated NBP amplitude change as the difference between the peak seasons of carbon uptake and release by the biosphere, namely May-July and October-December averages, respectively. We chose three-month averages for multi-model ensemble, because not all models simulate peak uptake in June and peak release in October. Monthly output of NBP, NPP and R_h^* (derived from NBP and NPP) from all models were first resampled to $2^{\circ} \times 2^{\circ}$ grids. Then the spatial and zonal means for both May-July and October-December were computed.

Results

Changes of CO₂ and NBP seasonal amplitude

The CMIP5 models project that the increase of CO₂ seasonal amplitude continues in the future. Figure 4-1a shows detrended and globally averaged monthly column atmospheric CO₂ from 1961 to 2099, averaged over nine models (no IPSL).

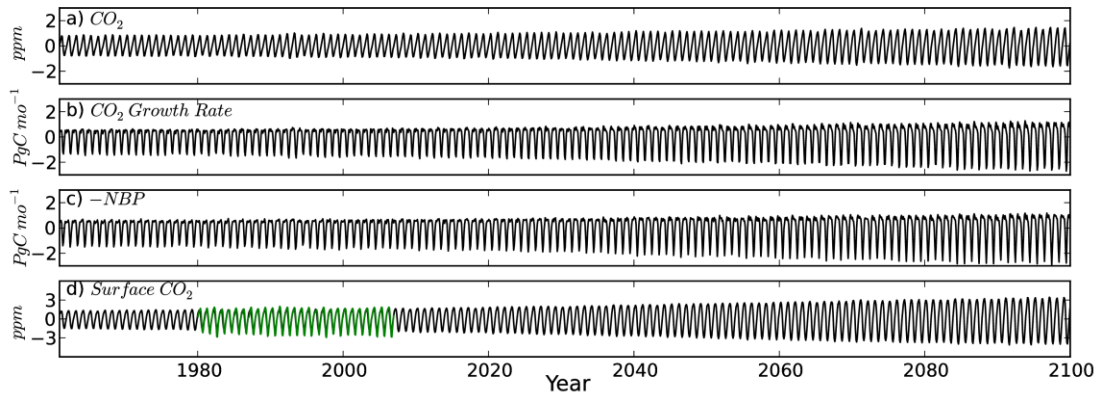


Figure 4-1: Nine-model (excluding IPSL) averaged monthly detrended a). Global mean CO₂ (ppm, column average); b). Global mean CO₂ growth rate (PgC Month⁻¹, using a conversion factor of 1 ppm = 2.12 PgC Month⁻¹); and c). Global total -NBP (PgC Month⁻¹) from 1961 to 2099. Panel d) presents eight-model (excluding IPSL and INM) averaged monthly detrended global mean CO₂ (ppm) at lowest model level and ESRL’s global mean detrended surface CO₂ observation (shown in green).

The models project an increase of CO₂ seasonal amplitude (defined as maximum minus minimum in each year) by about 70% over 120 years, from 1.6 ppm during 1961-1970 to 2.7 ppm in 2081-2090. The increase is faster in the future than in the historical period. Another feature is that the trend of minima (-0.63 ppm Century⁻¹) has a larger magnitude than the trend of maxima (0.41 ppm Century⁻¹), suggesting that enhanced vegetation growth contributes more to the amplitude increase than respiration increase. Gurney and Eckels (2011) found the trend of net flux in dormant season is larger than that of growing season. However, they applied a very different definition for amplitude, considering all months instead of maxima and minima, to analyze the atmospheric CO₂ inversion results from 1980-2008. Specifically, they defined growing season net flux (dormant season net flux) as the total of any month for which the net carbon flux is negative (positive), and amplitude as the difference of the two net fluxes. It is no surprise they reached a conclusion that seems to contradict ours, since growing season is much shorter than dormant season

at global scale. Figure 4-1b and 4-1c present detrended global mean CO₂ growth rate (1 ppm=2.12 PgC Month⁻¹ for unit conversion) and global total -NBP, two quantities showing very similar characteristics as expected. All models simulate an increase in amplitude, although considerable model spread is found (Table 4-2). In addition, we notice a phase advance of maxima and minima by counting their time of occurrence (data not shown). Excluding models above one standard deviation from the ensemble mean yields similar results.

Table 4-2: Amplitude (maximum minus minimum) of global mean column atmospheric CO₂, CO₂ growth rate (CO₂g) and global total NBP, averaged over 1961-1970 and 2081-2090 for the nine models, and their multi-model ensemble (MME) and standard deviation (SD).

Models	CO ₂ (ppm)		CO ₂ g (PgC Month ⁻¹)		-NBP (PgC Month ⁻¹)	
	1961-1970	2081-2090	1961-1970	2081-2090	1961-1970	2081-2090
BNU-ESM	1.54	2.96	2.2	4.91	1.88	4.42
CanESM2	0.9	1.53	1.12	2.05	1.2	1.83
CESM1-BGC	1.2	1.76	1.51	2.59	1.6	2.38
GFDL-ESM2m	2.37	3.81	3.42	5.93	3.52	6.24
INM-CM4	0.27	0.41	0.38	0.57	0.3	0.49
MIROC-ESM	2.55	3.92	3.93	5.98	3.77	5.37
MPI-ESM-LR	3.45	5.47	4.35	6.37	4.61	7.51
MRI-ESM1	1.97	4.04	2.37	5.21	2.63	5.7
NorESM1-ME	1.23	1.8	1.6	2.63	1.74	2.73
MME*	1.72	2.86	2.32	4.03	2.36	4.07
SD	0.97	1.59	1.34	2.09	1.38	2.33

*The multi-model ensemble (MME) here is a simple average over the nine models in the table. The values are slightly larger than given in text because of averaging method (in the main text, multi-model averaging of detrended variables are done first, then their amplitude are computed and mean amplitude changes are derived).

To illustrate how well the models reproduce the seasonal variations of CO₂, we compared the multi-model ensemble global CO₂ at the lowest model level—not equivalent to the height of surface CO₂ measurement, but relatively close—with ESRL’s global mean CO₂ over 1981-2005 (Figure 4-1d). The surface CO₂ seasonal amplitude estimated by the model ensemble is lower than that of ESRL’s global CO₂ estimate (Ed Dlugokencky and Pieter Tans, NOAA/ESRL, www.esrl.noaa.gov/gmd/ccgg/trends/), however the amplitude increases are similar (Table 4-3). This surface station-based global CO₂ estimate also indicates that the amplitude increase is dominated by the trend of minima.

Table 4-3: Amplitude increase (ppm) and trends of maxima/minima of surface CO₂ from eight models, their multi-model ensemble (MME), and ESRL’s Global mean CO₂ (CO₂GL).

Models	1981-1985 (ppm)	2001- 2005 (ppm)	Percent Change	Trend of Minima (ppm 10yr ⁻¹)	Trend of Maxima (ppm 10yr ⁻¹)
BNU-ESM	2.71	3.1	14.39%	-0.099	0.096
CanESM2	3.04	3.24	6.58%	-0.064	0.02
CESM1-BGC	2.05	2.18	6.34%	-0.032	0.044
GFDL-ESM2m	3.71	3.76	1.35%	-0.033	0.095
MIROC-ESM	3.39	3.61	6.49%	-0.078	0.045
MPI-ESM-LR	6.19	7.02	13.41%	-0.25	0.171
MRI-ESM1	3.69	3.85	4.34%	-0.095	0.031
NorESM1-ME	2.37	2.47	4.22%	-0.024	0.016
MME	3.1	3.37	8.71%	-0.084	0.065
CO₂GL	4.11	4.4	7.06%	-0.102	0.024

We further calculated the change of relative amplitude (relative to 1961-1970) for each model. The amplitude here is computed by the CCGCRV package. As

illustrated in Figure 4-2, all nine models show an increase in both global mean CO₂ and total NBP seasonal amplitude. CO₂ seasonal amplitude has increased by $62 \pm 19\%$

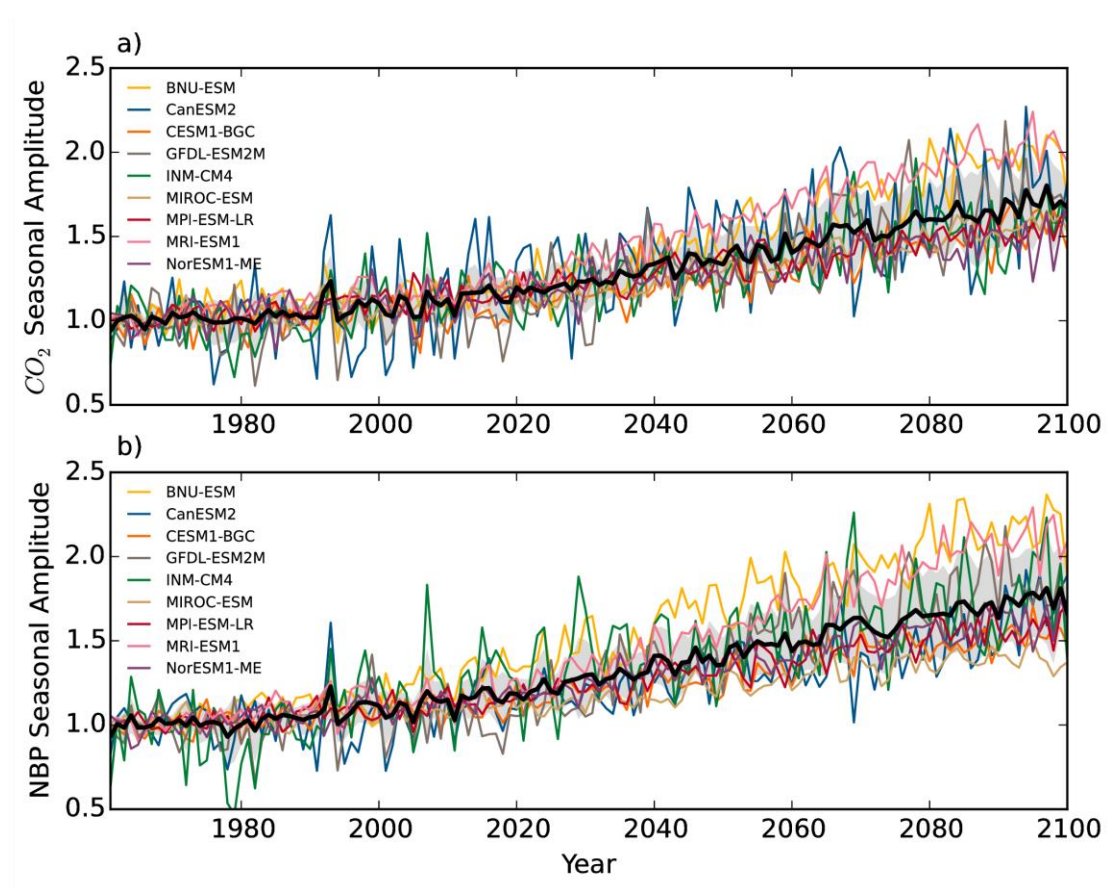


Figure 4-2: Time series of the relative seasonal amplitude (relative to 1961-1970 mean) of a). Global mean atmospheric CO₂; and b). Global total NBP from 1961 to 2099. Thick black line represents multi-model ensemble, and one standard deviation model spread is indicated by light grey shade.

in 2081-2090, compared to 1961-1970; whereas NBP seasonal amplitude has increased by $68 \pm 25\%$ over the same period (see Table 4-4 for details of individual models). The trend of increase is much higher in the future (CO₂/NBP: 0.70%/0.73% per year during 2006-2099) than in the historical period (0.25% and 0.28% per year

Table 4-4: Column atmospheric CO₂ and NBP amplitude (computed by CCGCRV, slightly different from max minus min) Increases of nine models by 2081-2090 relative to their 1961-1970 values and their multi-model ensemble (MME).

Models	CO ₂	NBP
BNU-ESM	93%	113%
CanESM2	65%	47%
CESM1-BGC	46%	47%
GFDL-ESM2m	57%	79%
INM-CM4	51%	67%
MIROC-ESM	52%	39%
MPI-ESM-LR	54%	58%
MRI-ESM1	99%	106%
NorESM1-ME	45%	58%
MME	62%	68%

during 1961-2005 for CO₂ and NBP), albeit the model spread also becomes larger in the future. When we applied the same procedure to the Northern Hemisphere (25-90 °N) mean CO₂ and total NBP for the eight models (excluding INM-CM4 which only has global CO₂ mass), we saw a higher amplitude increase and larger model spread: 81 ±46% and 77 ±43% for CO₂ and NBP, respectively.

Production vs. respiration

Our next major question is whether the amplitude increase of NBP is largely driven by NPP or respiration. We computed the mean seasonal cycle of detrended CO₂ growth rate, -NBP, -NPP (reverse signs so that negative values always indicate carbon uptake) and R_h^* in two periods: 1961-1970 (black) and 2081-2090 (red), for the nine models (for this and following analyses, we excluded INM which does not provide NPP, and included the IPSL model except for CO₂ growth rate). The seasonal cycle of -NBP resembles that of detrended CO₂ growth rate (Figure 4-3a-d),

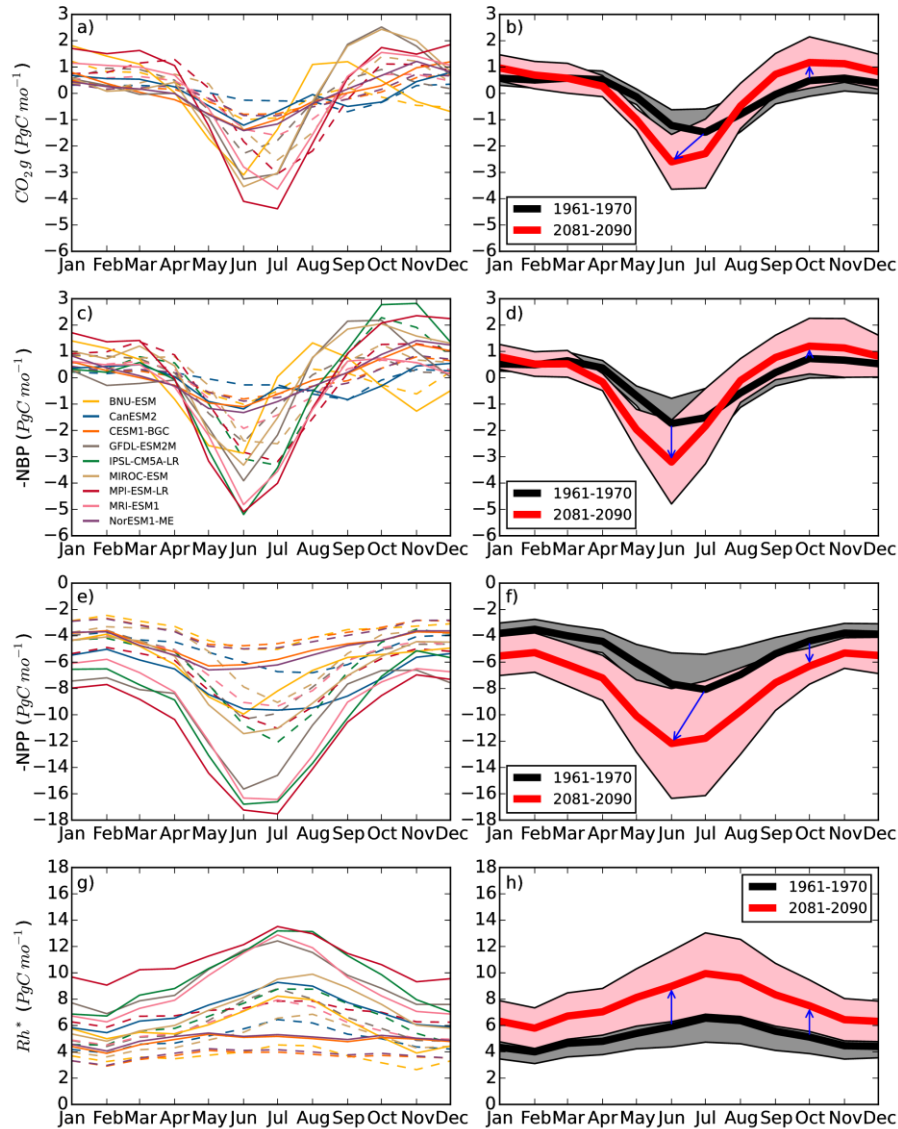


Figure 4-3: Seasonal cycle of detrended global mean CO_2 growth rate (a, b), global total $-\text{NBP}$ (c, d), global total $-\text{NPP}$ (e, f), and global total R_h^* (g, h, computed as NPP minus NBP), averaged over 1961-1970 and 2081-2090 for the CMIP5 models (excluding INM, also excluding IPSL for CO_2 growth rate). Seasonal cycles of individual models are presented in the left panel (dashed for 1961-1970, and solid for 2081-2090). Ensemble mean and one standard deviation model spread (black/grey for 1961-1970, red/pink for 2081-2090) are displayed in the right panels. Blue arrows mark the changes in June and October (NBP maxima and minima), except for CO_2 growth rate and $-\text{NPP}$, where arrows also indicate phase shifts of minima between the two periods. We show $-\text{NBP}$ and $-\text{NPP}$ so that the negative values represent carbon uptake by the biosphere, and positive values indicate carbon release from the biosphere. Note that $-\text{NBP}$ and its two components $-\text{NPP}$ and R_h^* are not detrended, so that the sum of panels f and h equals to panel d. Detrended $-\text{NBP}$ seasonal cycle (not shown) looks very similar to panel d, as its trend is small compared to the magnitude of seasonal cycle.

confirming that the activities of land ecosystem dominate the CO₂ seasonal cycle and its amplitude increase in the model simulations. Except for CanESM2 (also noted in Anav et al., 2013), and BNU-ESM (which simulates a second peak carbon uptake around November) to some extent, most models can reproduce the net uptake of carbon during spring and summer (when increasing NPP overcomes respiration) and the net carbon release during fall and winter at global scale: net carbon uptake peaks in June (five models) or July (three models) for the historical period, and exclusively in June for the future period. However, the model spread on amplitude is large: CESM1-BGC and NorESM1-ME, which has the same land model (CLM4) that features an interactive nitrogen cycle, are characterized by a small seasonal amplitude of $-NBP$ — merely 30% of those on the high end of the models (IPSL-CM5A-LR and MPI-ESM-LR). The seasonal amplitude of multi-model ensemble NBP, computed as maximum minus minimum (June-October), has increased from 2.7 PgC Month⁻¹ to 4.7 PgC Month⁻¹ (Figure 4-3d). This 2 PgC Month⁻¹ amplitude increase is the sum of enhanced net carbon uptake in June and higher net release in October, and the enhancement in uptake (1.4 PgC Month⁻¹) is nearly three times as large as the release increase (0.5 PgC Month⁻¹).

We then investigate the June and October changes of $-NPP$ and R_h^* , respectively. By definition, their sum should equal to the amplitude change of $-NBP$. NPP has increased in all months (Figure 4-3e, f), with much larger changes during the NH growing season. The amplitude of multi-model ensemble NPP has increased from 4.8 PgC Month⁻¹ to 7.1 PgC Month⁻¹, and an increase from 2.7 to 4.3 PgC Month⁻¹ is found for R_h^* . In June, NPP increase (4.5 PgC Month⁻¹) is larger than that of R_h^* (3.1

PgC Month⁻¹), resulting in enhanced net uptake. In October, NPP increase (1.9 PgC Month⁻¹) is smaller than that of R_h^* (2.4 PgC Month⁻¹), leading to enhanced net release. These results are consistent with trends of maxima and minima in Figure 4-1. The models also indicate a shift in peak NPP from July to June, consistent with the shift of CO₂ minima.

Spatial and latitudinal contributions

To further investigate the regional contribution to NBP amplitude increase, we plotted the 10-model mean $-NBP$ changes (Figure 4-4) over peak NH growing season (May-July, panel a) and dormant season (October-December, panel b). Because the models disagree on the time of maximum and minimum NBP (Figure 4-3), our choice of doing seasonal averages would be more representative of the models than averaging over one month. Note that the difference between the two seasonal averages is smaller than the peak-to-trough amplitude, but here we are only concerned with the spatial pattern. We saw stronger net carbon uptake in May-July almost everywhere north of 45°N, and also over the Tibetan Plateau and some places near equator. Net carbon uptake weakens over Western United States and Central America, South and Southeast Asia and Central South America. The change of net carbon release in October-December generally shows an opposite spatial pattern, with a noticeably smaller magnitude north of 45°N.

In addition, we calculated the corresponding zonal averages (panel c). The area-weighted totals of the zonal mean curves correspond to the future minus historical averages of global total $-NBP$ (Figure 4-3d), averaged over May-July and

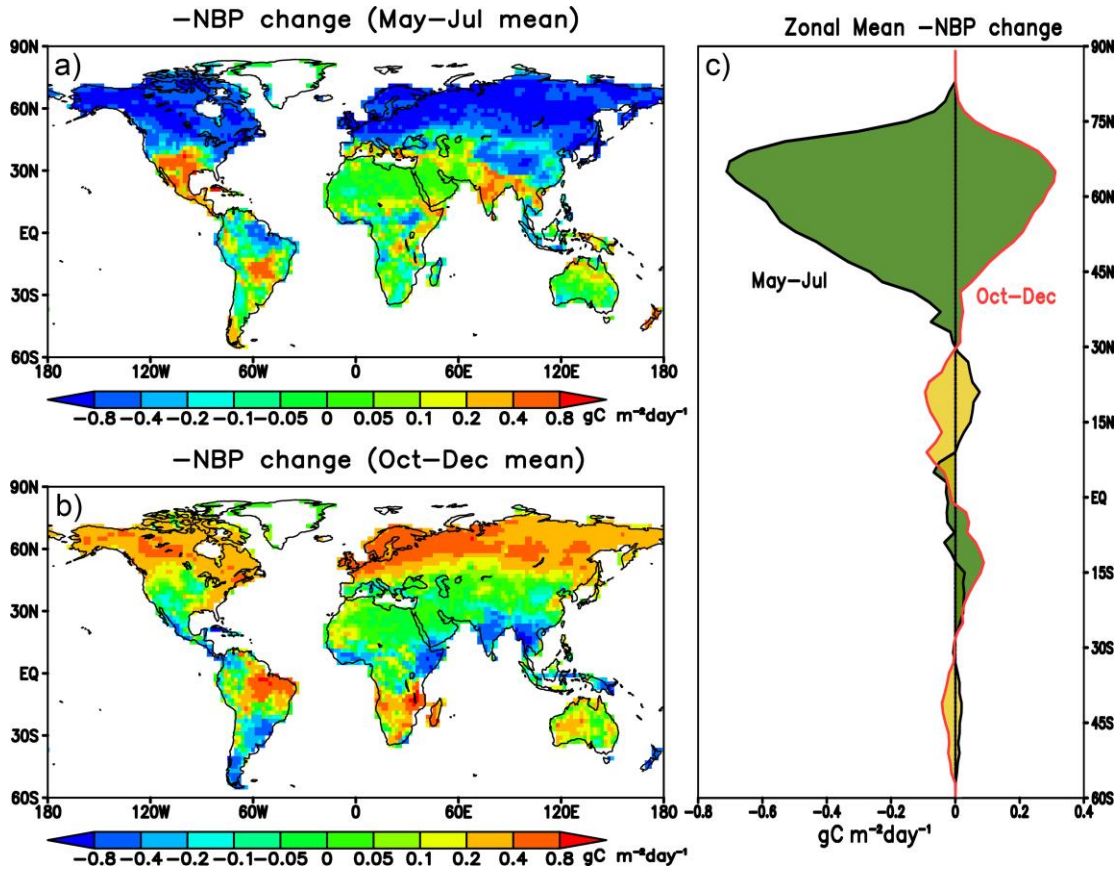


Figure 4-4: Spatial patterns and latitudinal distributions of 10-model mean $-NBP$ ($\text{gC m}^{-2} \text{day}^{-1}$) changes between 2081-2090 and 1961-1970, during mean a) peak growing season (May-July) and b) dormant season (October-December). Panel c aggregates the spatial patterns in panels a and b zonally, where the black curve corresponds to the $-NBP$ changes in May-July (panel a), and the red curve corresponds to the $-NBP$ changes in October-December (panel b). Further reduction of $-NBP$ in peak growing season—where the black curve falls on the left of the zero line, and increase of $-NBP$ in dormant season—where the red curve is on the right of the zero line, both contribute to amplitude increase. We shade those instances in green, and shade the reversed case (contribute negatively to global total $-NBP$ amplitude increase) in yellow. It is clear that the amplitude increase is dominated by the boreal regions, and by changes in peak growing season.

October-December, respectively. These two curves do not account for phase difference; instead, they approximate latitudinal contribution to the amplitude increase of global total $-NBP$. It is apparent that this increase is dominated by regions

north of 45 °N with a weak contribution from the Southern Hemisphere tropics (25 °S-0 °). The Northern subtropical region and Southern Hemisphere (10-30 °N, 55-35 °S) partly offset the amplitude increase. It is also clear that the amplitude increase is dominated by changes in peak growing season (the green shade is larger on the left of the zero line than on its right), consistent with our findings in the previous section.

Analogous to the cold-warm seasonality in the temperate/boreal region, the tropics has distinctive dry and wet seasons, and recently Wang et al. (2014) suggested the tropical ecosystem is becoming more sensitive to climate change. In our analyses on the multi-model ensemble patterns, the tropical region exhibits a small negative contribution to the seasonal amplitude increase of global total $-NBP$. This does not mean the net carbon flux in the tropics, which has a different seasonal cycle phase, would experience an amplitude decrease in the future. To illustrate the seasonal amplitude change at different latitudes, we show the zonal amplitude of NBP in the historical (black) and future (red) periods for all models (Figure 4-5). At every 2 ° band, we first calculated a ten-year mean seasonal cycle, then compute its amplitude (maximum minus minimum). Most models predict an increase in NBP seasonal amplitude at almost every latitude under the RCP85 emission scenario. Only two of the models, CanESM2 and MIROC-ESM, predict decreased seasonality for parts of the tropics and subtropics. Unlike in Figure 4-4c, an area-weighted integral cannot be performed due to different phases zonally. The Southern Hemisphere has an opposite phase from its Northern counterpart, but its magnitude is small due to its small land area. The two subtropical maxima around 10 °N and 10-15 °S reflect the wet-dry seasonal shift in the Inter-Tropical Convergence Zone (ITCZ) and monsoon

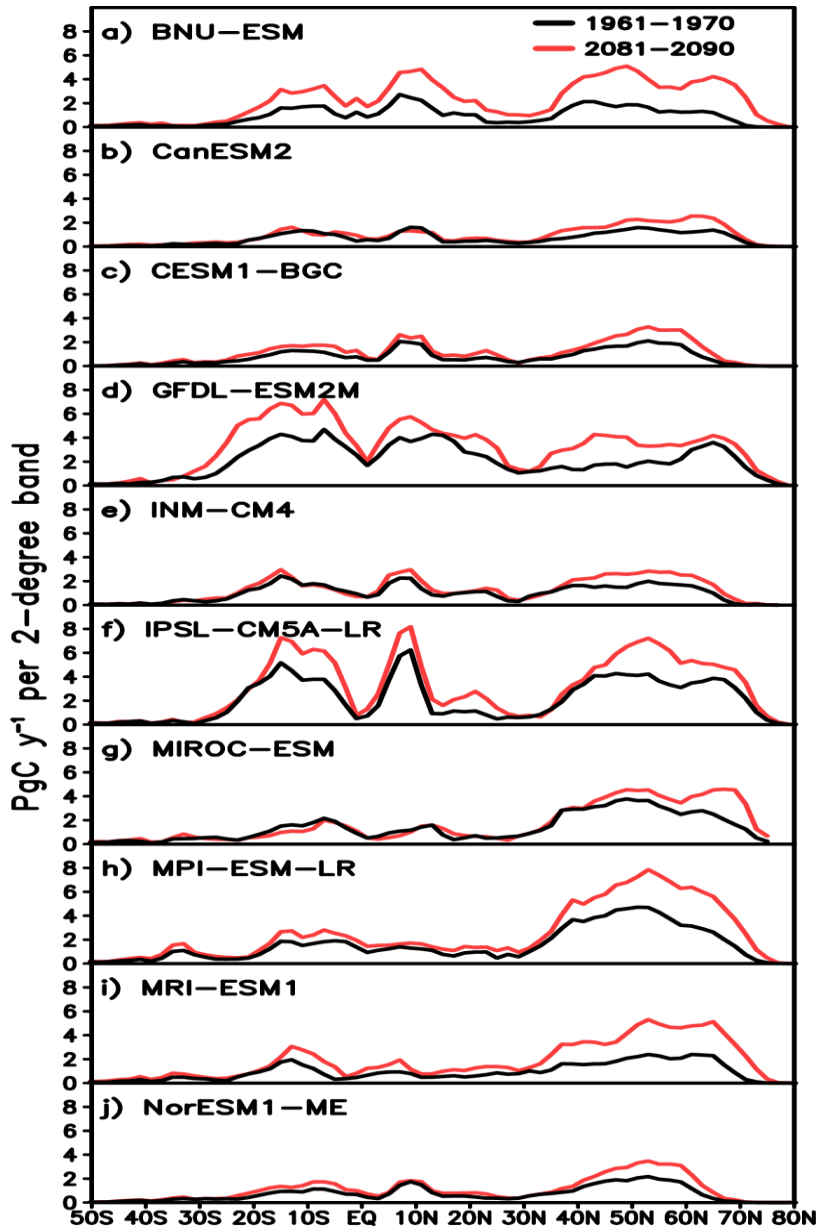


Figure 4-5: Zonal amplitude of NBP from the 10 CMIP5 models (PgC Month^{-1} per 2° band), averaged over 1961-1970 (black) and 2081-2090 (red). For each model, NBP is first regridded to a $2^\circ \times 2^\circ$ common grid. Monthly zonal totals are then computed for every 2° band, which determine the amplitude (maximum minus minimum) at every band. The Southern Hemisphere has an opposite phase from its northern counterpart, but its magnitude is small due to its small land area. The two subtropical maxima around 10°N and $10\text{--}15^\circ\text{S}$ reflect the wet-dry seasonal shift in the Inter-Tropical Convergence Zone (ITCZ) and monsoon movement. They have similar magnitude as the Northern Hemisphere maxima in about a third of the models, however their net contribution to global total NBP seasonal amplitude is small, because they are out of phase and largely cancel each other out.

movement. They are comparable to the NH maxima in terms of both amplitude and amplitude increase for about a third of the models, however they are out of phase and largely cancel each other out.

To further illustrate this cancelation effect, we aggregated monthly $-NBP$ over six large regions: the globe (90°S-90°N), Northern boreal (50-90°N), Northern temperate (25-50°N), Northern tropics (0-25°N), Southern tropics (25°S-0°) and Southern Hemisphere (90-25°S) (Figure 4-6). It is clear that the changes of global $-NBP$ seasonal cycle mostly come from the Northern boreal region; it partly comes from the Northern temperature region in a few models. The seasonal cycle of the Northern tropics is characterized by spring maxima and fall minima, and prominent increases of its seasonal amplitude are found for BNU-ESM, GFDL-ESM2M and IPSL-CM5A-LR. However, they are largely counterbalanced by the Southern tropics. For GFDL-ESM2M, changes in the Southern tropics are larger than its Northern counterpart, but even so, the net contribution of tropical regions to its global $-NBP$ seasonal amplitude (September maxima minus June minima) increase is limited to about 25%, the largest of all models.

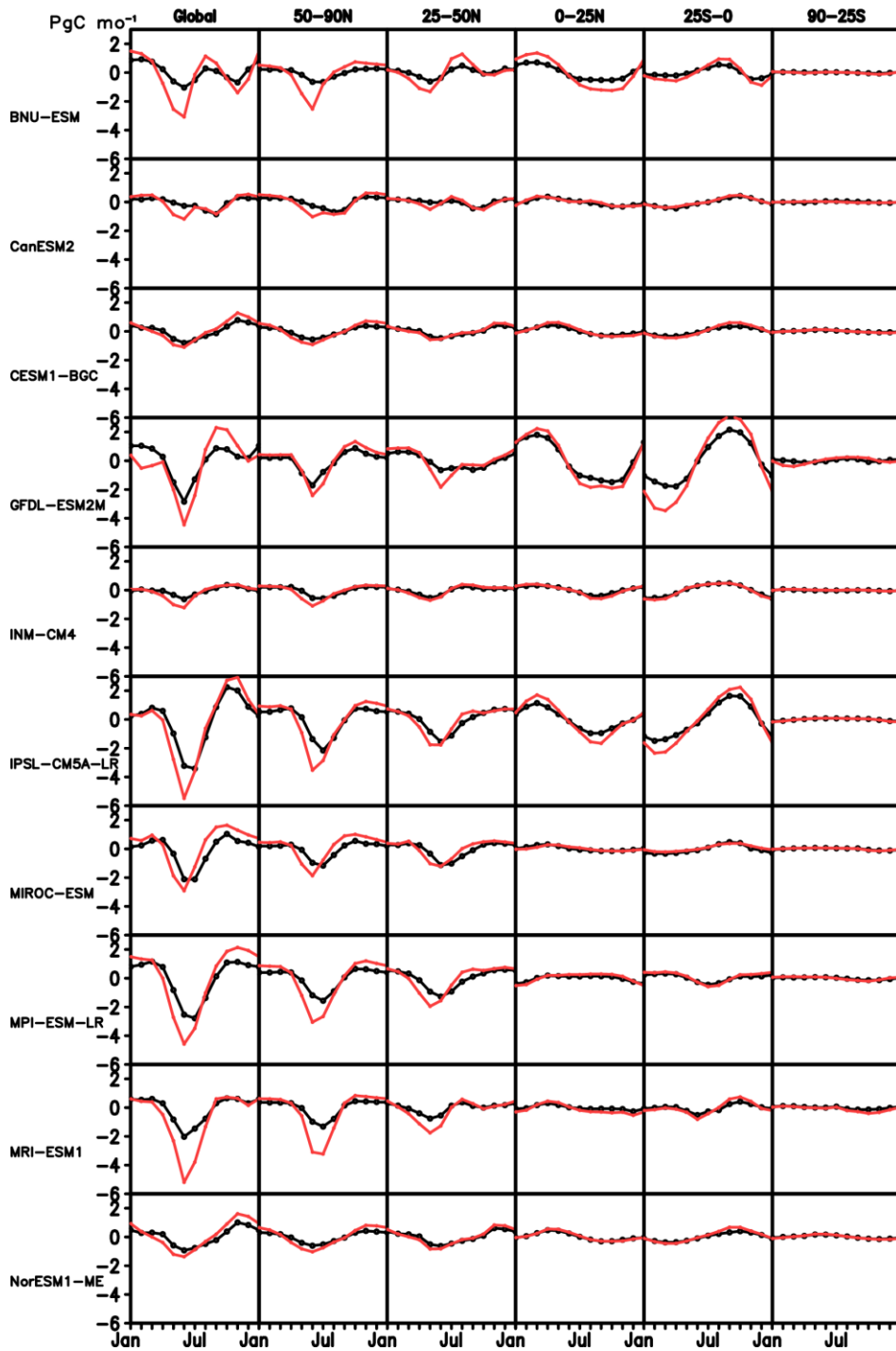


Figure 4-6: Seasonal cycles of global and regional total $-NBP$, averaged over 1961-1970 (black) and 2081-2090 (red). The last month of the year is repeated. The Northern and Southern subtropics are clearly out of phase and largely cancel each other out. GFDL-ESM2M represents the largest tropical contribution to its global $-NBP$ seasonal cycle (maxima in September and minima in June) of all models, accounting for about a quarter of the amplitude increase.

Mechanisms for amplitude increase

As discussed in Section 1, two major mechanisms for amplitude increase identified in previous literature are CO₂ fertilization effect and high latitudes “greening” in a warmer climate. Both mechanisms lead to enhanced ecosystem productivity during peak growing season, and consequently more biomass to decompose in dormant season, therefore increasing the amplitude of NBP seasonal cycle. Because models have different climate and CO₂ sensitivity (Arora et al., 2013), their relative importance may vary. In the case of CMIP5 ESMs, two additional sensitivity experiments are recommended: Fixed Feedback 2 (esmFdbk2) and Fixed Climate 2 (esmFixClim2). The former keeps CO₂ concentration fixed but allows physical climate change responding to increasing historical and future (RCP4.5) concentrations; the latter keeps climate fixed under preindustrial CO₂ condition but allows the carbon cycle to respond to historical and future (RCP4.5) CO₂ increase. This setup does not permit quantifying the contribution of CO₂ increase and climate change to NBP amplitude increase: one major difference is the use of RCP4.5 concentrations instead of RCP8.5 emissions. However, we can still make qualitative assessments by examining the spatial patterns. We will focus on the high latitude regions, which contribute most to amplitude increase of global total NBP.

Of the 10 models we studied, only CanESM2, GFDL-ESM2M and IPSL-CM5A-LR have submitted NBP output for these two experiments (MIROC submitted output for esmFixClim2 only). Here we display the spatial patterns of –NBP changes for GFDL-ESM2M (Figure 4-7) and IPSL-CM5A-LR (Figure 4-8). CanESM2 results

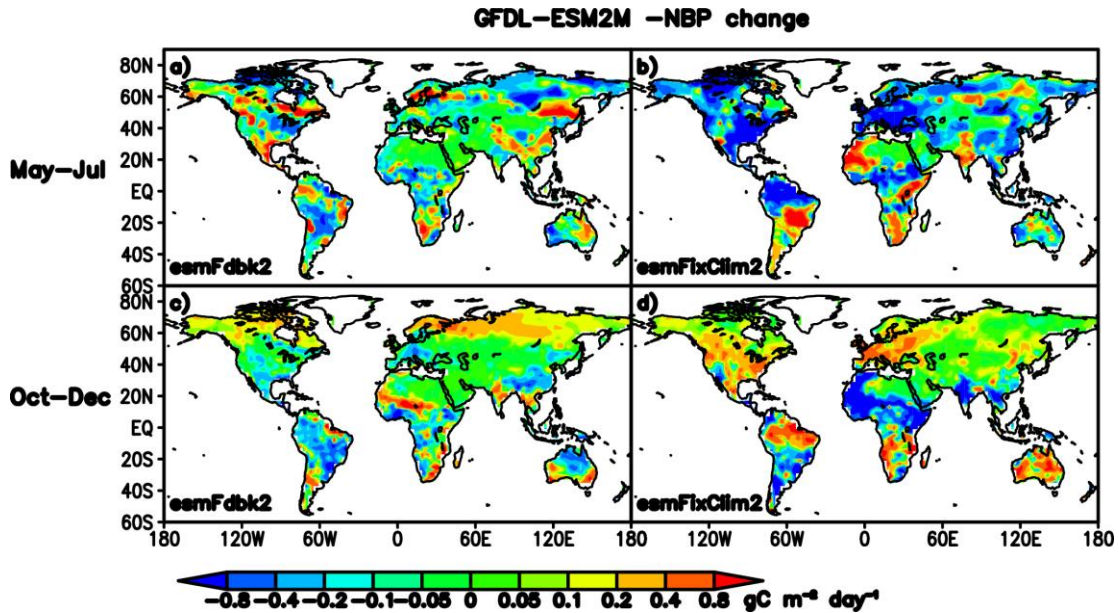


Figure 4-7: Spatial patterns of GFDL-ESM2M $-NBP$ ($\text{gC m}^{-2} \text{ day}^{-1}$) changes between 2081-2090 and 1961-1970, during mean peak growing season (May-July, first row) and dormant season (October-December, second row) for the *esmFdbk2* (first column, constant CO_2 fertilization and changing climate) and *esmFixClim2* (second column, constant climate and rising CO_2) experiments. The Northern high latitude regions show mixed response to climate change during peak growing season (panel a), and most of the Northern temperate and boreal regions see enhanced carbon uptake under elevated CO_2 (panel b). Net carbon release is increased both under climate change (panel c) and elevated CO_2 conditions (panel d), however they have different spatial patterns.

are not shown because it does not correctly reproduce the phase of global total NBP seasonal cycle. The changes of $-NBP$ for both models during peak growing season are clearly dominated by CO_2 fertilization effect (right panels). In contrast, climate change under fixed CO_2 fertilization conditions has mixed effects on high latitude regions. Northern high latitude net carbon release in October-December is increased both under climate change (Figure 4-7c) and elevated CO_2 conditions (Figure 4-7d) for GFDL-ESM2M, but over different regions. For IPSL-CM5A-LR however, net carbon release increase in regions north of 45°N is only obvious under elevated CO_2 condition.

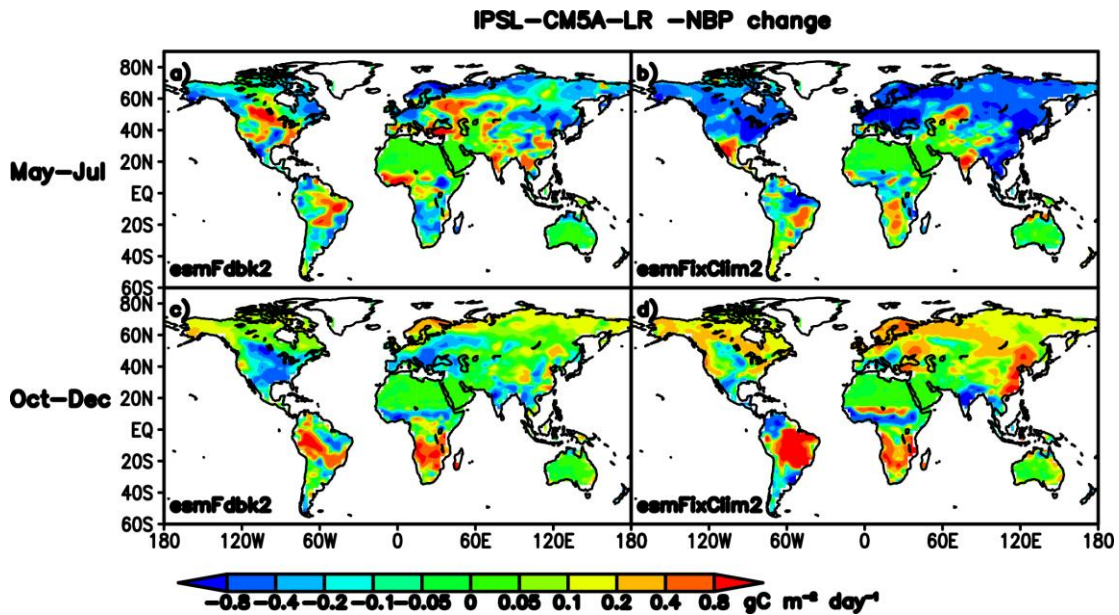


Figure 4-8: Same as figure 4-7, but for IPSL-CM5A-LR. Both the carbon uptake in peak growing season and net carbon release in dormant season are clearly dominated by changes in atmospheric CO₂ rather than climate for this model.

Our results only indicate CO₂ fertilization effect is the dominant factor for NBP seasonal amplitude increase in some models. For models with strong carbon-climate feedbacks and weak/moderate water constraints in Northern high latitude regions, climate change may be more important. However, we cannot find a clear example due to data availability. MIROC-ESM is known to have strong carbon-climate feedback (Arora et al., 2013). From its simulation under fixed climate (figure not shown), we found no obvious patterns of widespread net carbon release increase in dormant season, suggesting climate change may play a bigger role for this model. The HadGEM model is another possible candidate; it is also a particularly interesting model to analyze since one of its historical simulations represented the largest

increase in CO₂ amplitude in Graven et al. (2013). Unfortunately, for the ESM simulations, both CO₂ and NBP from HadGEM are not available on the ESGF servers.

Relationship with mean carbon sink

Our analyses above suggest CO₂ fertilization effect is a major mechanism causing the amplitude increase in some models. If it is important in most models, we expect to see models with a larger change in mean carbon sink simulate a higher increase in seasonal amplitude. By plotting the $-NBP$ change against NBP seasonal amplitude increase for all 10 models (Figure 4-9), we found there is indeed a negative cross-model correlation ($R=-0.73$, $p<0.05$), indicating models with a stronger net carbon uptake are likely to simulate a larger increase in NBP seasonal amplitude. Note that this result is based on the 10 models we analyzed; it is subject to large uncertainty and may change substantially with inclusion or exclusion of certain model(s). Again all models show an increase in NBP seasonal amplitude, even though they disagree on the direction of future NBP change. While our study hint at a possible relationship between mean carbon sink and NBP seasonal amplitude, it is

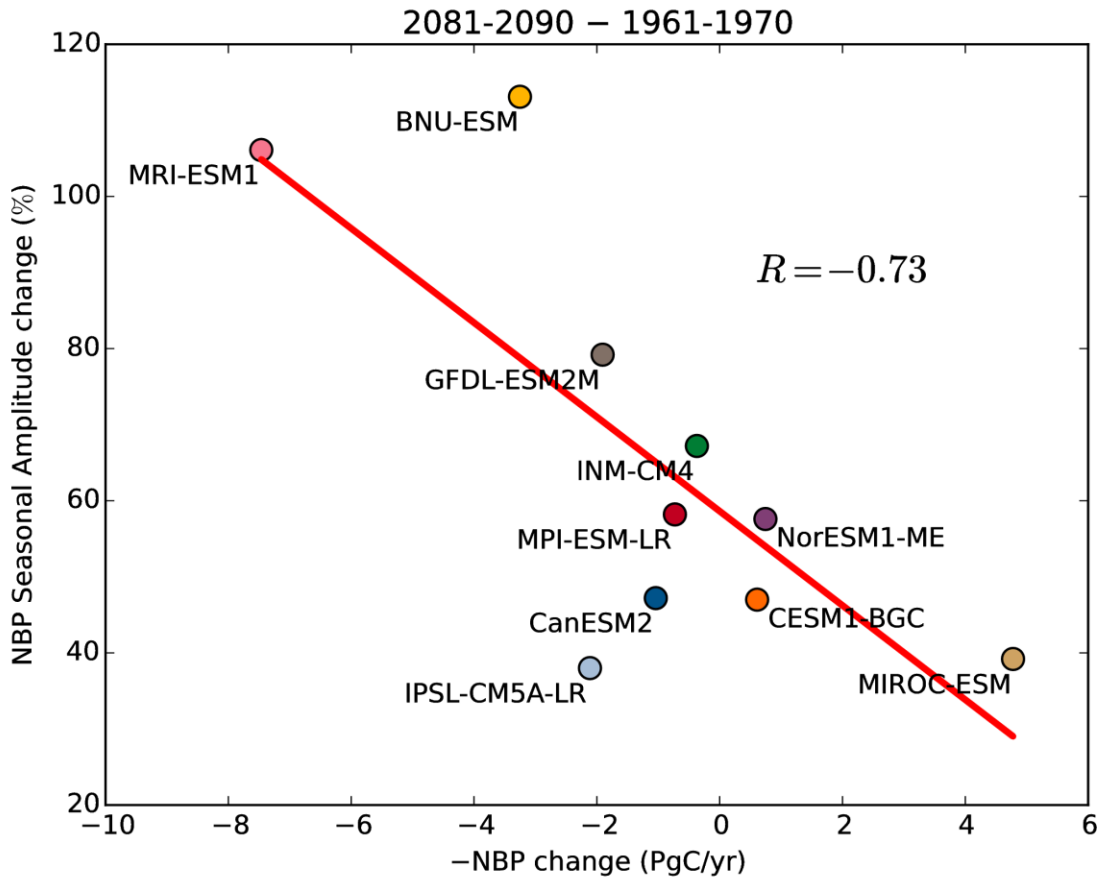


Figure 4-9: Relationship between $-NBP$ change and increase of NBP seasonal amplitude, calculated as the differences between 2081-2090 and 1961-1970 for 10 CMIP5 ESMs. The negative cross-model correlation ($R=-0.73$, $p<0.05$) suggests that a model with a larger net carbon sink increase is likely to simulate a higher increase in NBP seasonal amplitude.

beyond our scope to discuss further, or comment on why models show such different mean sink estimate. Interested readers may refer to the insightful discussion on this issue in Friedlingstein et al. (2013).

Discussion

We have primarily focused on model ensembles of aggregated quantities. Ensemble patterns are sometimes dominated by only a few models due to large seasonality variations among the models. However, the close examination of each individual model show that the spatial patterns of $-NBP$ change during peak growing season (May-July) are all dominated by high latitude regions (approximately north of $45^{\circ}N$). In CESM1-BGC and NorESM1-ME models, enhanced net carbon uptake are confined to some of the high latitude regions (Figure 4-10). Models differ on finer details. For example, about half of the models predict an obvious increase of net carbon uptake for the Tibetan Plateau. It is worth mentioning that the esmFixClim2 experiment of MIROC-ESM shows little change in NBP for this region under elevated CO_2 alone. High latitude regions also dominate the increase of net carbon release in October-December for most models (Figure 4-11). One exception is INM-CM4, which displays very small change in the dormant season, and most of its NBP amplitude increase comes from enhanced carbon uptake during peak growing season. BNU-ESM and CanESM2 have some limitations in reproducing the correct phase of global $-NBP$ seasonal cycle. Exclusion of these two models from ensemble mean calculation exhibits very similar spatial and zonal patterns as shown in Figure 4-4. Another caveat is the assumption of 1961-1970 as the historical condition and 2081-2090 as future condition. This choice is valid if the selected variables have roughly monotonic trends, and ten years is long enough to smooth out most of the interannual variability. Figure 4-2 suggests that this assumption is quite reasonable for model ensembles, and acceptable for individual models.

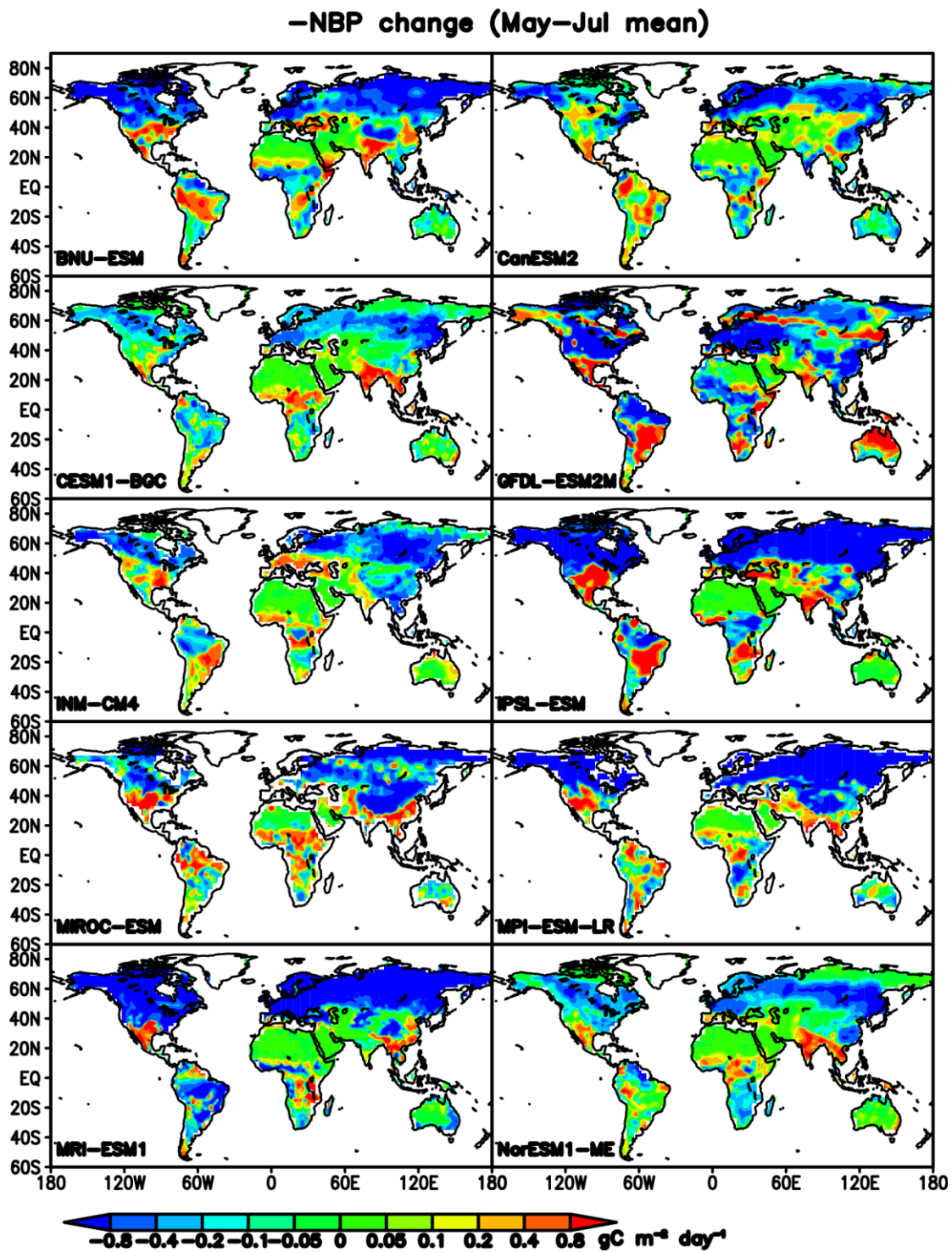


Figure 4-10: Spatial patterns of $-NBP$ ($\text{gC m}^{-2} \text{ day}^{-1}$) changes between 2081-2090 and 1961-1970, during peak growing season (May-July mean) for the 10 models.

-NBP change (Oct-Dec mean)

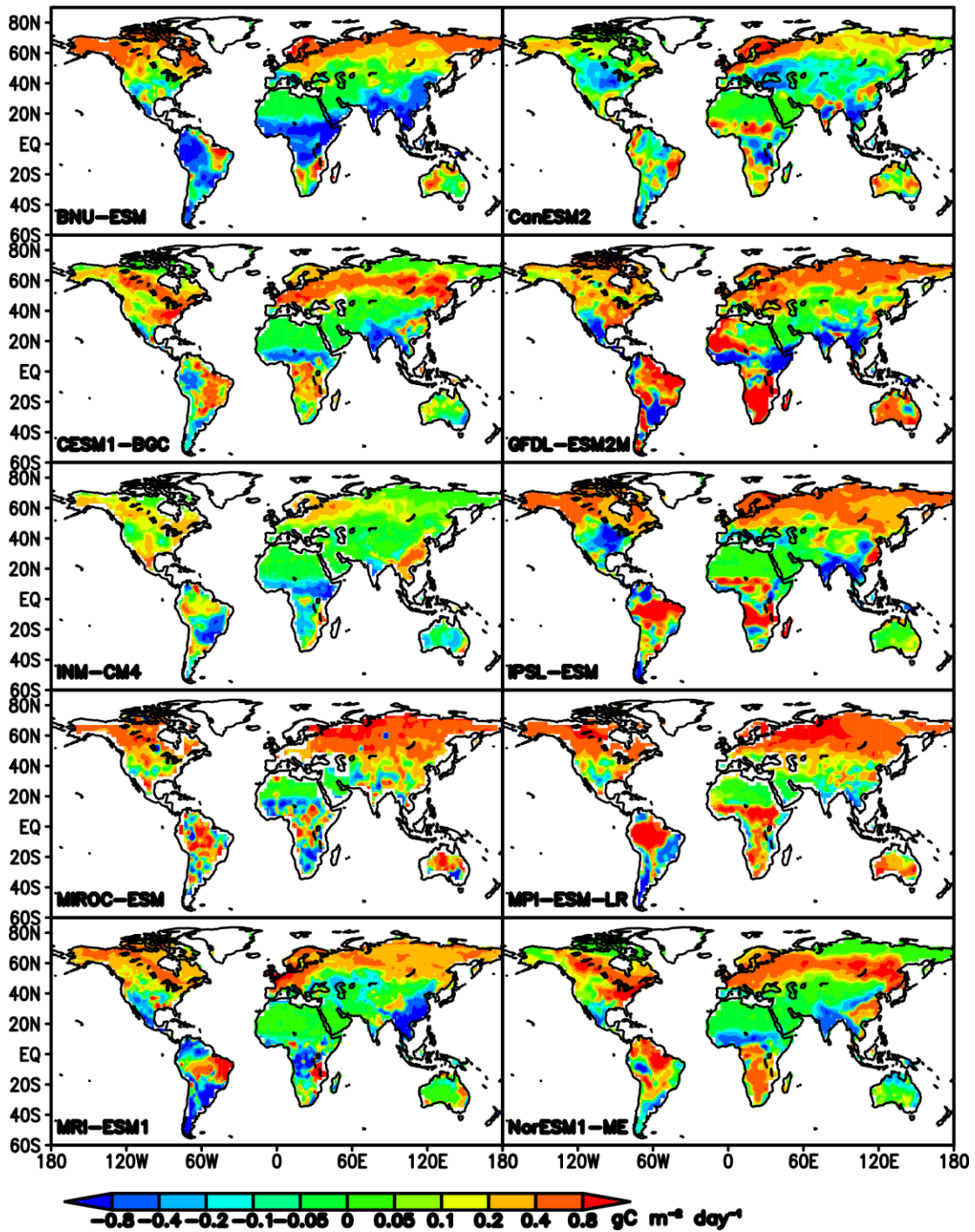


Figure 4-11: Spatial patterns of -NBP ($\text{gC m}^{-2} \text{ day}^{-1}$) changes between 2081-2090 and 1961-1970, during dormant season (October-December mean) for the 10 models.

We presented aggregated quantities due to large model uncertainty in space. We have largely omitted model evaluation against observations (due to limited observation during 1961-1970). However, this step can be helpful in model evaluation studies (Anav et al., 2013; Peng et al., 2015). One concern is to examine whether the models can reproduce observed CO₂ seasonal amplitude increase at the two stations with longest observation records—Mauna Loa, Hawaii and Point Barrow, Alaska. To address this issue, we extracted simulated CO₂ concentration from eight models at their model grid that is closest to Mauna Loa in the three-dimensional space (similar procedure for Point Barrow). The results of this comparison at one model grid can reflect multiple sources of model uncertainties (such as uncertainties in the atmospheric tracer transport and mixing simulations). For example, GFDL-ESM2M is known to simulate a damped CO₂ gradient (Dunne et al., 2013) which has long been identified as a deficit in models of the atmospheric CO₂ cycle (Fung et al., 1987).

Figure 4-12 (and Figure 4-13 for more details) presents the changes of CO₂ seasonal amplitude at Mauna Loa for the models and observation. CO₂ seasonal amplitude is underestimated by a factor of 2 in three quarters of the models. However, the amplitude increase from ensemble model estimate ($0.36 \pm 0.24\%$ per year, error range represents one standard deviation model spread) is much closer to observation ($0.34 \pm 0.07\%$ per year, error range represents one standard error of the least-squared trend calculation). MPI-ESM-LR reproduces both the magnitude and trend of Mauna

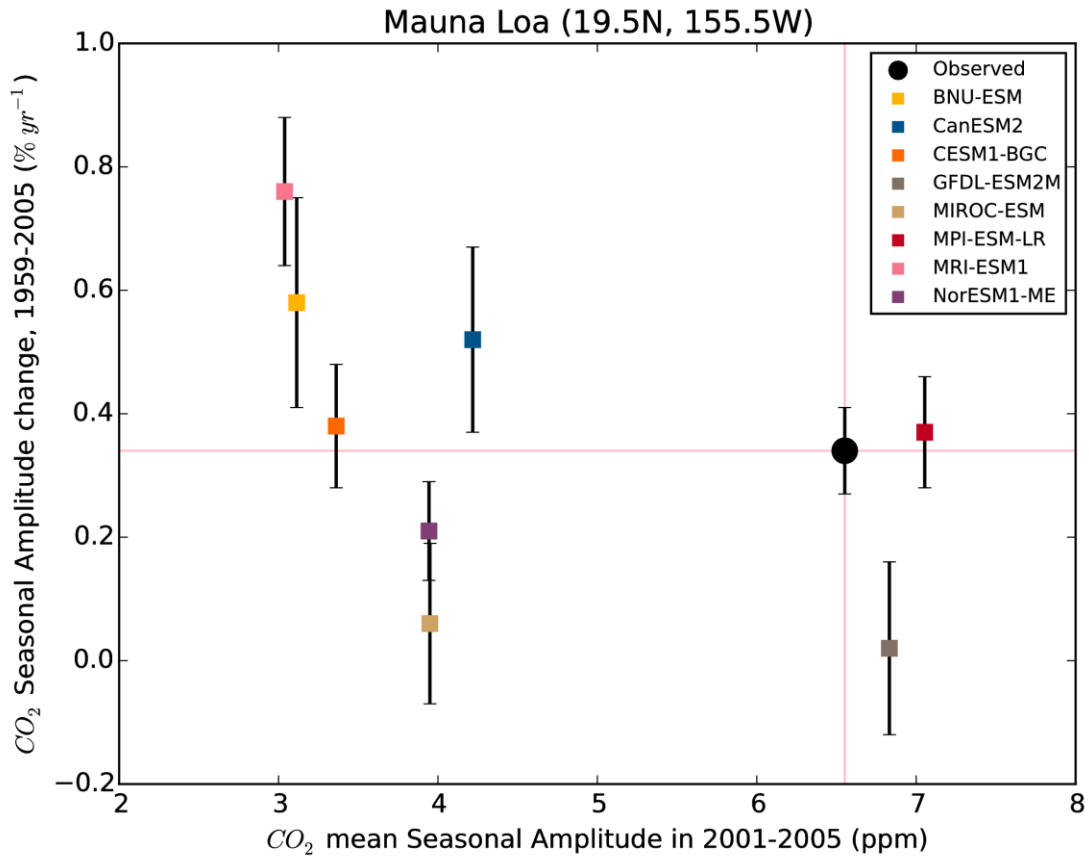


Figure 4-12: CO₂ mean seasonal amplitude (ppm) during 2001-2005 and increase in CO₂ seasonal amplitude at Mauna Loa during 1959-2005 (% yr⁻¹, linear trend) from eight CMIP5 models and observation. The big black circle represent surface CO₂ observation at Mauna Loa, Hawaii (19.5 N, 155.6 W; 3400m above sea level). The colored squares represent the 700 hPa (close to the altitude of Mauna Loa station surface) CO₂ output at the original grid that covers Mauna Loa from each of the eight models. Error bars indicate ± 1 standard error in the trend calculation. Compared to the surface observation, only MPI-ESM-LR and GFDL-ESM2M overestimate CO₂ mean seasonal amplitude at Mauna Loa, while the other models underestimate this amplitude. Models split between overestimating and underestimating the CO₂ seasonal amplitude increase at Mauna Loa.

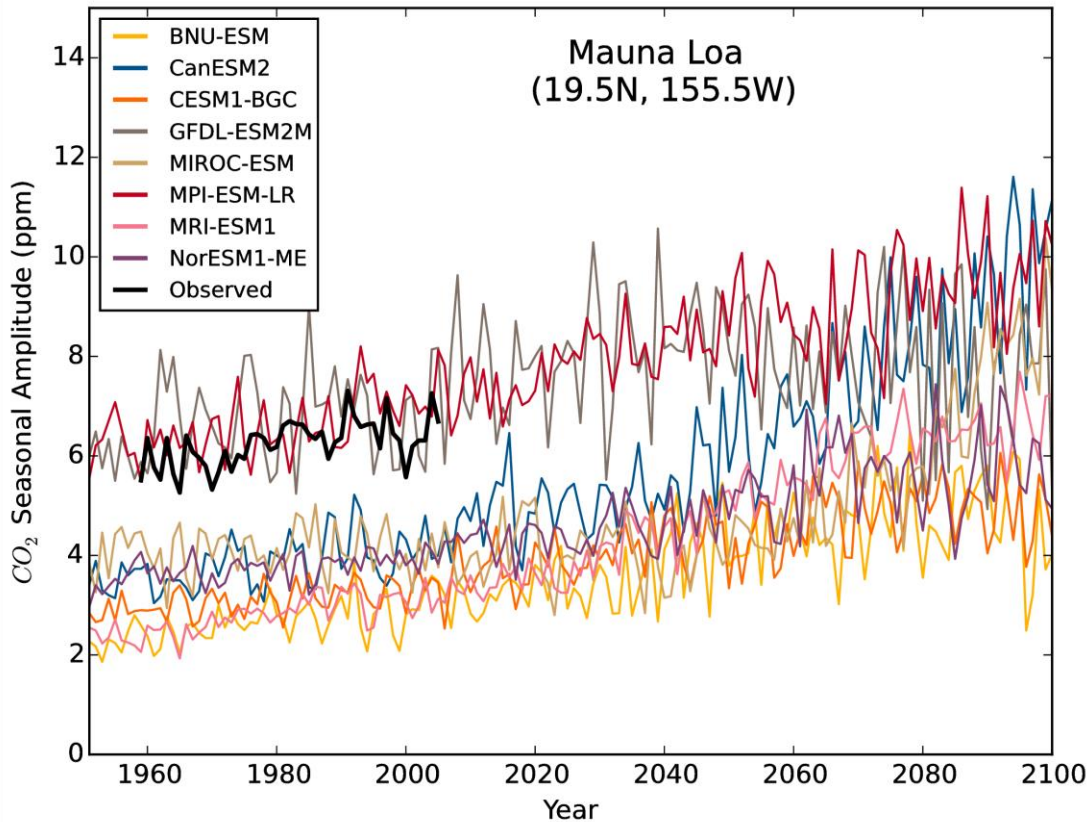


Figure 4-13: CO₂ seasonal amplitude (1951-2100) from eight models (excluding INM and IPSL) at the model grid that covers Mauna Loa, Hawaii (19.5 °N, 155.6 °W) at 700hPa. The thick black line represents seasonal amplitude of observed Mauna Loa CO₂ records during 1959-2005. All curves are computed by the CCGCRV package. Note that 1951-2005 model data are from esmHistorical, and 2006-2100 data are from esmRCP85.

Loa CO₂ seasonal amplitude reasonably well. For Point Barrow (Figures 4-14 and Figure 4-15), MPI-ESM-LR also simulates a similar amplitude increase to observation, but the magnitude of amplitude is much larger (almost twice). All other models underestimate the amplitude, but for the amplitude increase, the model ensemble ($0.46 \pm 0.21\%$ per year) again is similar to observation ($0.43 \pm 0.10\%$ per year). MRI-ESM1 is found to reproduce both the magnitude and increase of Point Barrow CO₂ amplitude quite well.

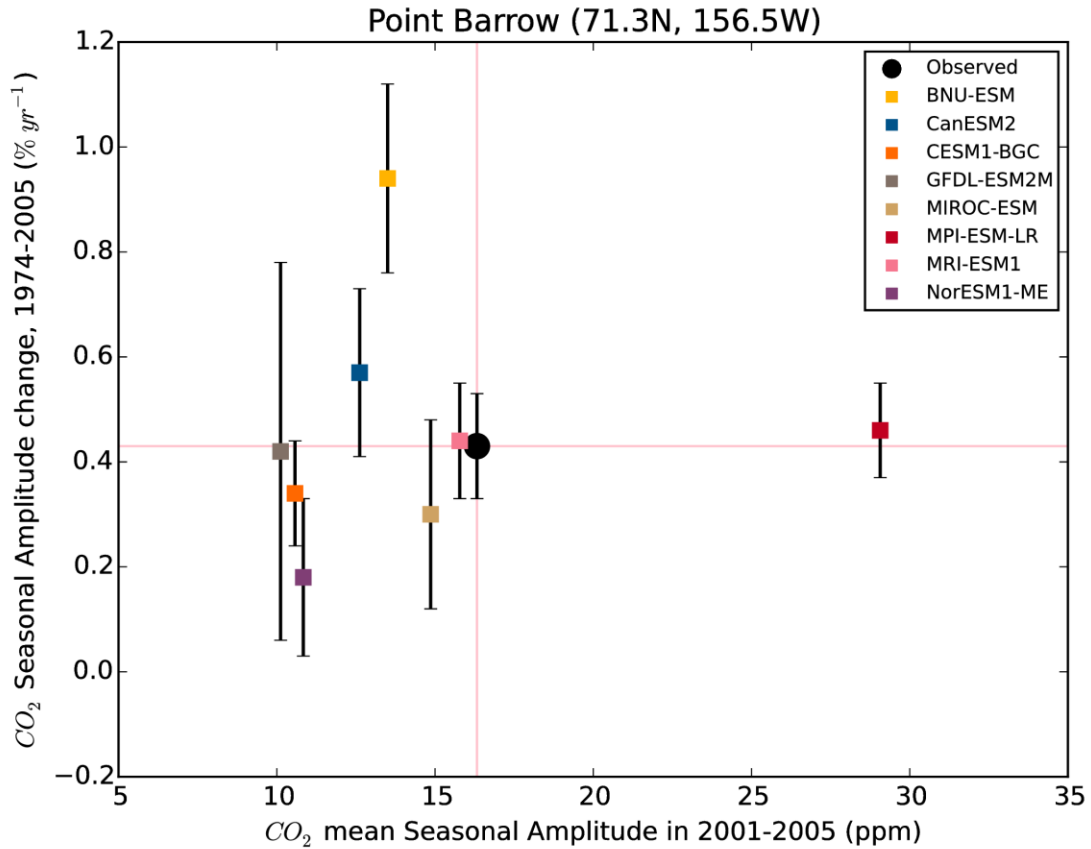


Figure 4-14: CO₂ mean seasonal amplitude (ppm) during 2001-2005 and increase in CO₂ seasonal amplitude at Pt. Barrow during 1974-2005 (% yr⁻¹, linear trend) from eight CMIP5 ESMs and observation. The big black circle represent surface CO₂ observation at Point Barrow, Alaska (71.3 N, 156.5 W; 11m above sea level). The colored squares represent the CO₂ output at lowest model level (four models at 1000 hPa, and four at 925 hPa) at the original grid that covers Point Barrow from each of the eight models. Error bars indicate ± 1 standard error in the trend calculation. Compared to the surface observation, only MPI-ESM-LR overestimate the CO₂ mean seasonal amplitude at Point Barrow, while the other models underestimate this amplitude. Models split between overestimating and underestimating the CO₂ seasonal amplitude increase at Point Barrow.

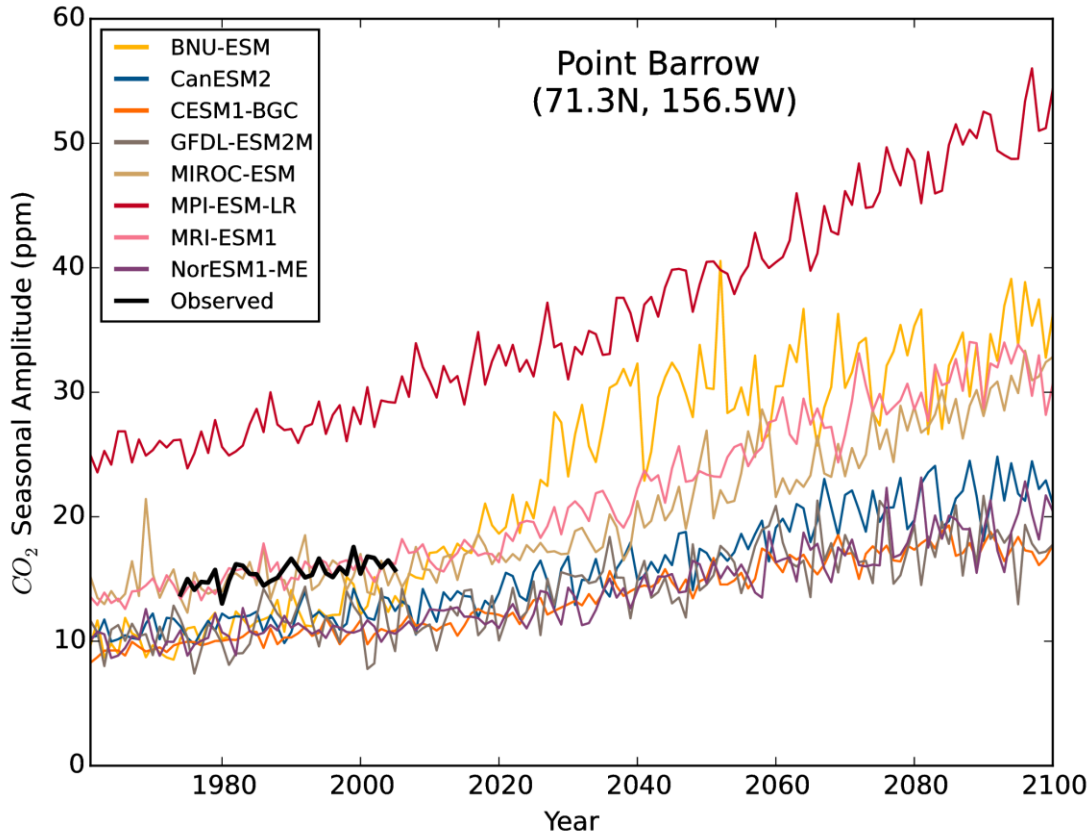


Figure 4-15: CO₂ seasonal amplitude (1951-2100) from 8 models (excluding INM and IPSL) at the model grid that covers Point Barrow, Alaska (71.3N, 156.5W) at lowest level (four models at 1000hPa, and four others at 925hPa). The thick black line represents seasonal amplitude of observed Point Barrow CO₂ records during 1974-2005. All curves are computed by the CCGCRV package. Note that 1951-2005 model data are from esmHistorical, and 2006-2100 data are from esmRCP85.

Graven et al. (2013) found the CMIP5 models substantially underestimate the amplitude increase of CO₂ north of 45°N at altitude of 3 to 6 km. However, we did not find the models underestimate Point Barrow CO₂ amplitude increase at surface level. One big difference is the observational data used for comparison. During the 1974-2005 period, CO₂ seasonal amplitude increases by 0.43% yr⁻¹, or 21.5% over 50 years at the Point Barrow station. This is much lower than the ~50% amplitude increase found between the two aircraft campaigns during 1958-1961 and 2009-2011

(Graven et al., 2013). This difference might be attributed to mechanisms controlling the vertical profile of CO₂ concentration. It is also not clear to what extent the large interannual variability of CO₂ seasonal amplitude affects the trend estimation of observed CO₂ amplitude increase.

Under the RCP8.5 emission scenario, CMIP5 showed a $62 \pm 19\%$ increase of CO₂ seasonal cycle globally from 1961-1970 to 2081-2090. The increase is $85 \pm 48\%$ at Mauna Loa (range indicates one standard deviation model spread), and $110 \pm 42\%$ at Point Barrow. Even though the CMIP5 models are able to reproduce the increase of CO₂ seasonal amplitude at the two locations, some of the models rely heavily on the CO₂ fertilization mechanism, which may be too strong compared to observational evidence. Previous research suggest it should explain no more than 25% of the observation at a high fertilization effect permitted by lab experiments (Kohlmaier et al., 1989). Similarly, Randerson et al. (1997) found the linear factor of CO₂ fertilization has to be 4 to 6 times greater than the mean of the experimental values, in order to explain the $0.66\% \text{ yr}^{-1}$ amplitude increase (north of 55 °N) during 1981-1995. Recent studies have indicated that some important mechanisms, such as changes in ecosystem structure and distribution (Graven et al., 2013) and land use intensification (Zeng et al., 2014), are missing in the current CMIP5 models. Yet another main source of uncertainty is future CO₂ emissions. The RCP8.5 scenario used to drive the ESMs is on the high side of future scenarios. Also, the emission-driven runs simulate higher CO₂ than observed over the historical period, and such biases are likely to accumulate over time as the increase of atmospheric CO₂ growth rate accelerates (Hoffman et al., 2014).

The models do not have the same strength of carbon-climate feedback, but even if they do, their response to climate change may vary significantly simply because they simulate very different climate change. To briefly address this issue, we present soil moisture (Figure 4-16 and 4-17) and near-surface temperature (Figure 4-18 and 4-19)

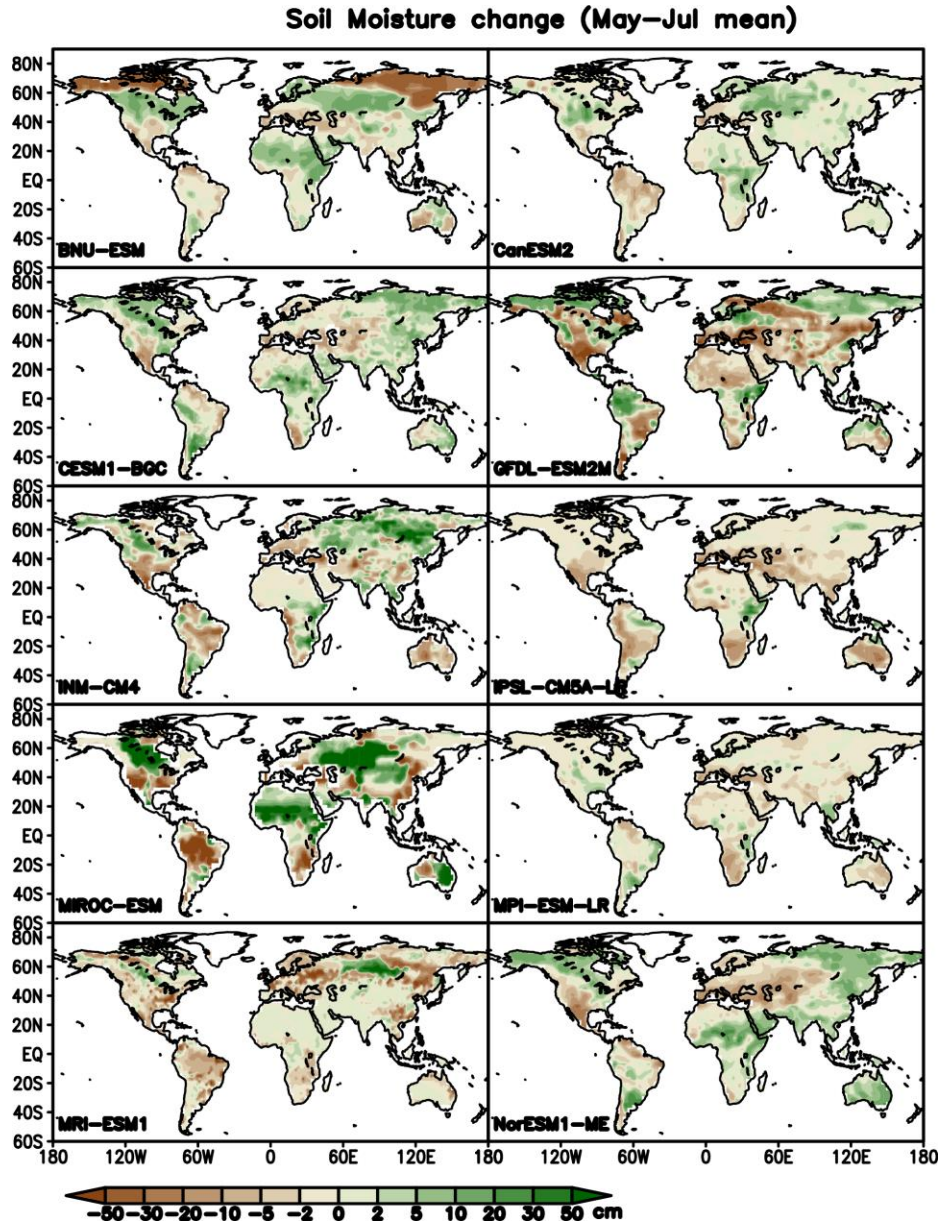


Figure 4-16: Spatial patterns of soil moisture (cm) changes between 2081-2090 and 1961-1970, during peak growing season (May-July mean) for the 10 models.

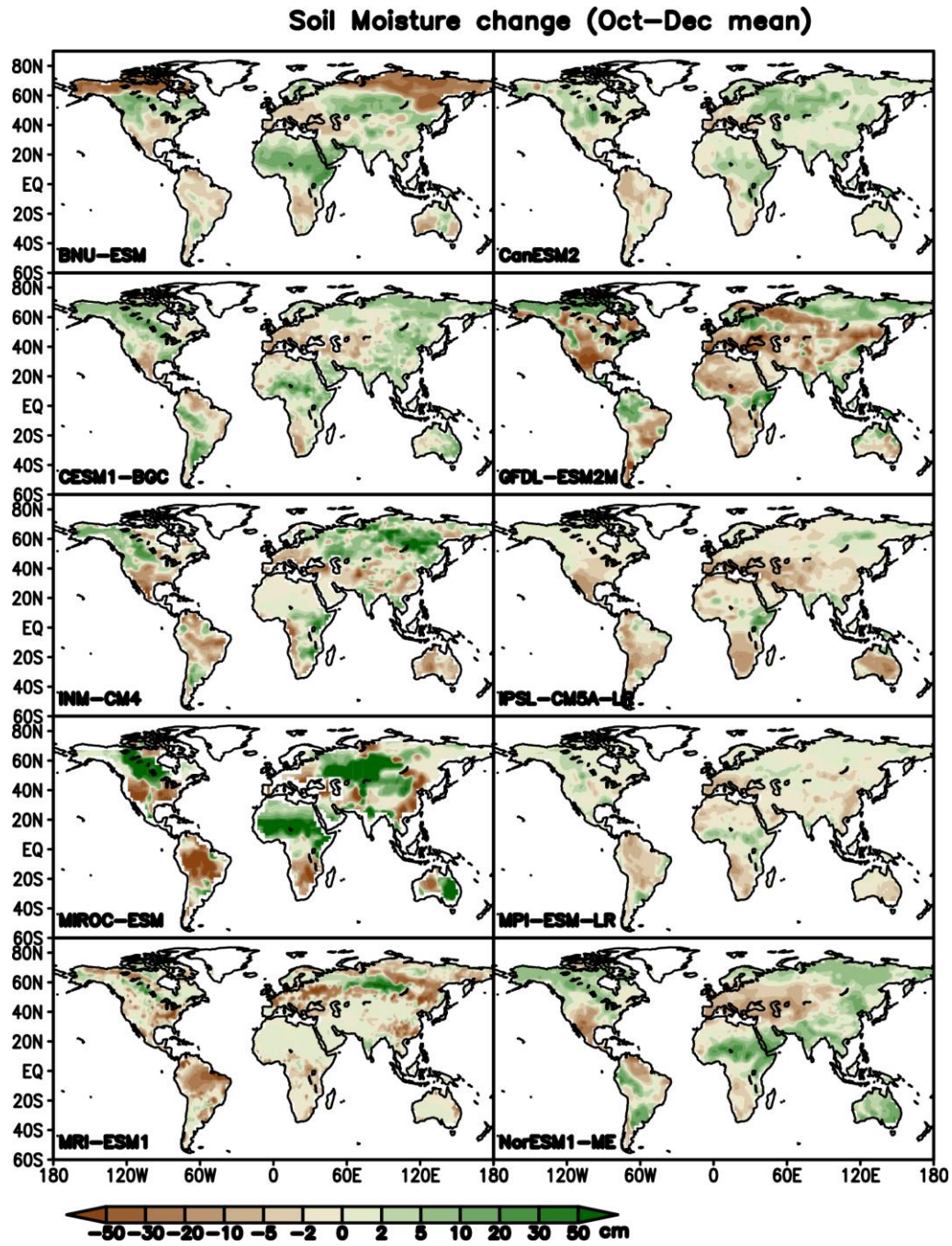


Figure 4-17: Spatial patterns of soil moisture (cm) changes between 2081-2090 and 1961-1970, during dormant season (October-December mean) for the 10 models.

Near-Surface Soil Temperature change (May–Jul mean)

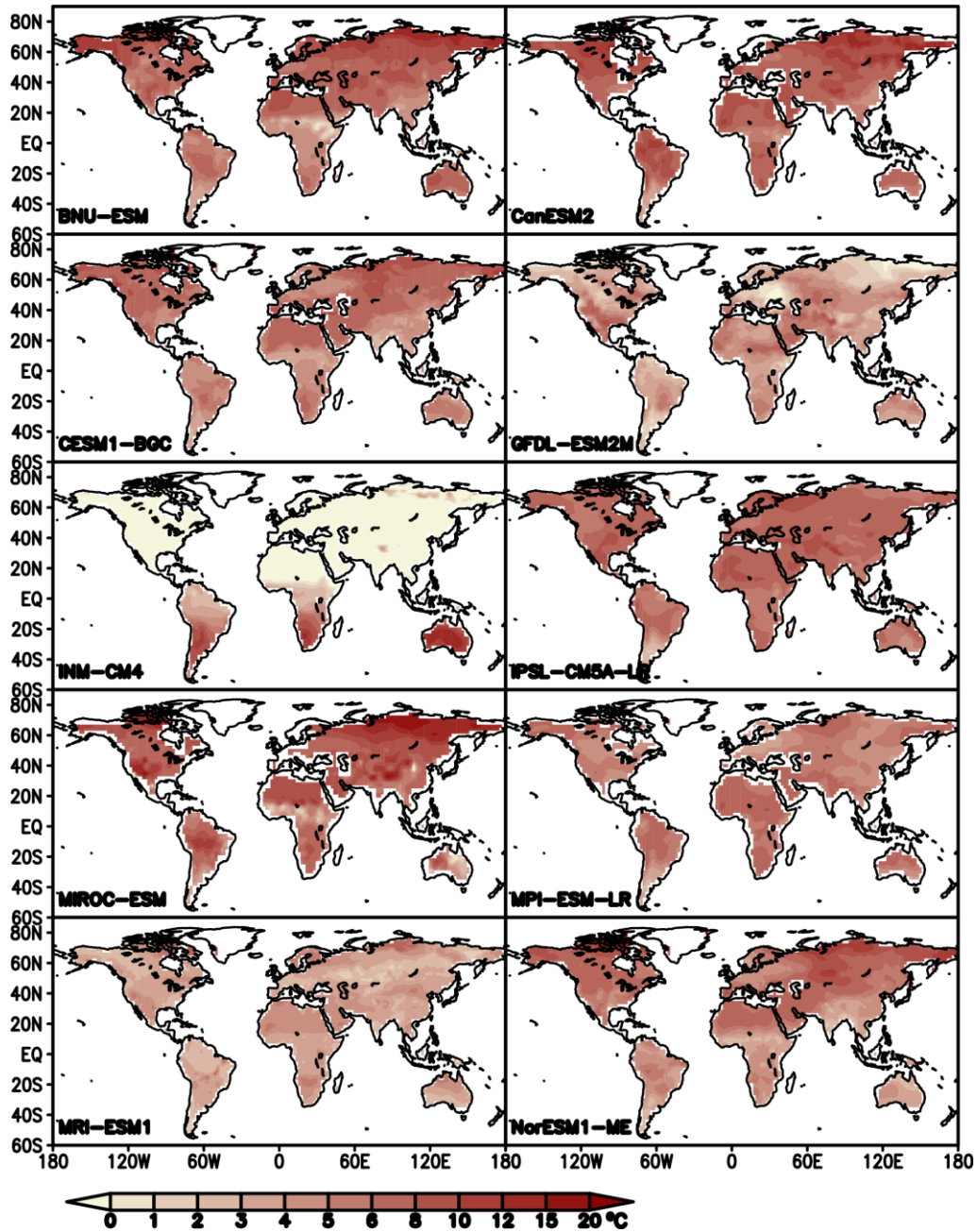


Figure 4-18: Spatial patterns of near-surface soil temperature (°C) changes between 2081-2090 and 1961-1970, during peak growing season (May-July mean) for the 10 models.

Near-Surface Soil Temperature change (Oct-Dec mean)

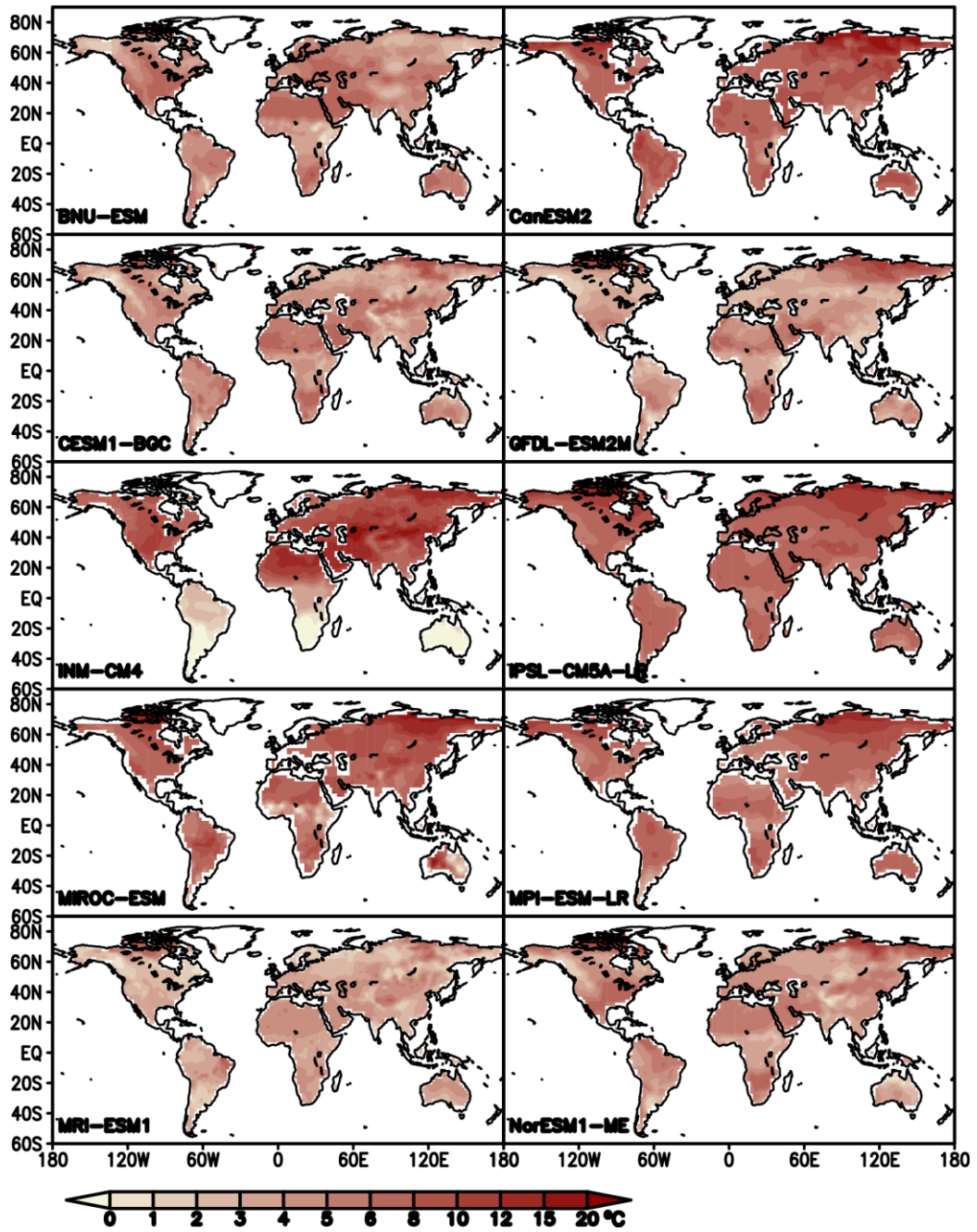


Figure 4-19: Spatial patterns of near-surface soil temperature ($^{\circ}\text{C}$) changes between 2081-2090 and 1961-1970, during dormant season (October-December mean) for the 10 models.

changes for all models. All the models show temperature increase, but in different ranges. The more prominent difference was observed in the spatial pattern of soil moisture changes predicted by models. The combined effect of soil moisture regimes, temperature change and PFT specifications could cause diverse behaviors of models over same regions. Such are important caveats that highlight the importance of sensitivity experiments and warrant more in-depth future studies.

The combined effect of climate and CO₂ changes not only alters the balance between production and respiration for existing ecosystems, but also lead to changes of ecosystem types. For example, Figure 4-20 shows that the tree fraction has increased over wide areas of the Northern high latitude regions for MPI-ESM-LR and INM-CM4. Figure 4-21 reveals notable natural grass increase over the Northern high latitude regions for BNU-ESM. Such widespread vegetation change has not been observed during the satellite era, and it is possibly yet another highly uncertain mechanism contributing to amplitude increase in some CMIP5 models.

Tree cover fraction change (2081–2090 – 1961–1970)

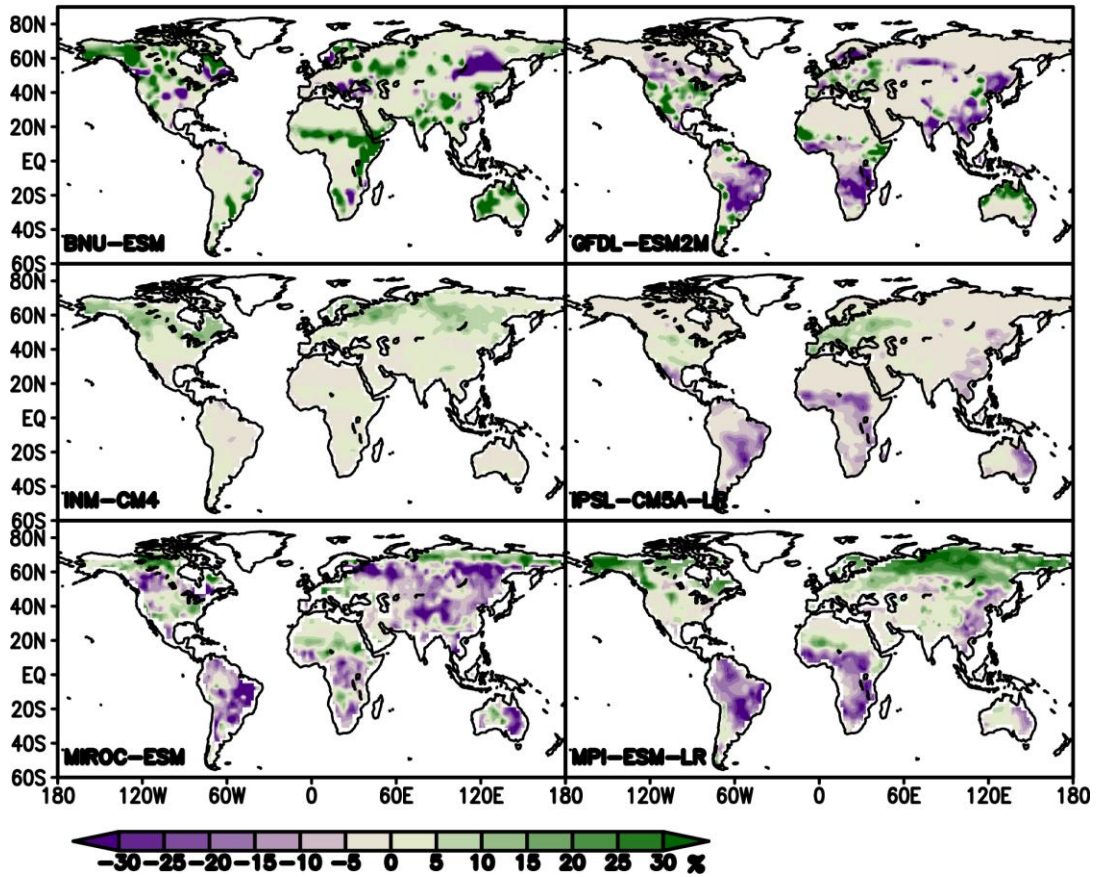


Figure 4-20: Changes of tree cover fractions between future (2081-2090) and historical (1961-1970) periods from six CMIP5 ESMs. The values represent fractional cover changes relative to the whole grid cell, instead of relative change of tree cover. For MPI-ESM-LR and INM-CM4, tree fraction has increased over wide areas of the Northern high latitude regions. For MIROC-ESM, tree fraction has generally decreased over the same regions, possibly in response to a hotter and drier climate condition.

Natural grass fraction change (2081–2090 – 1961–1970)

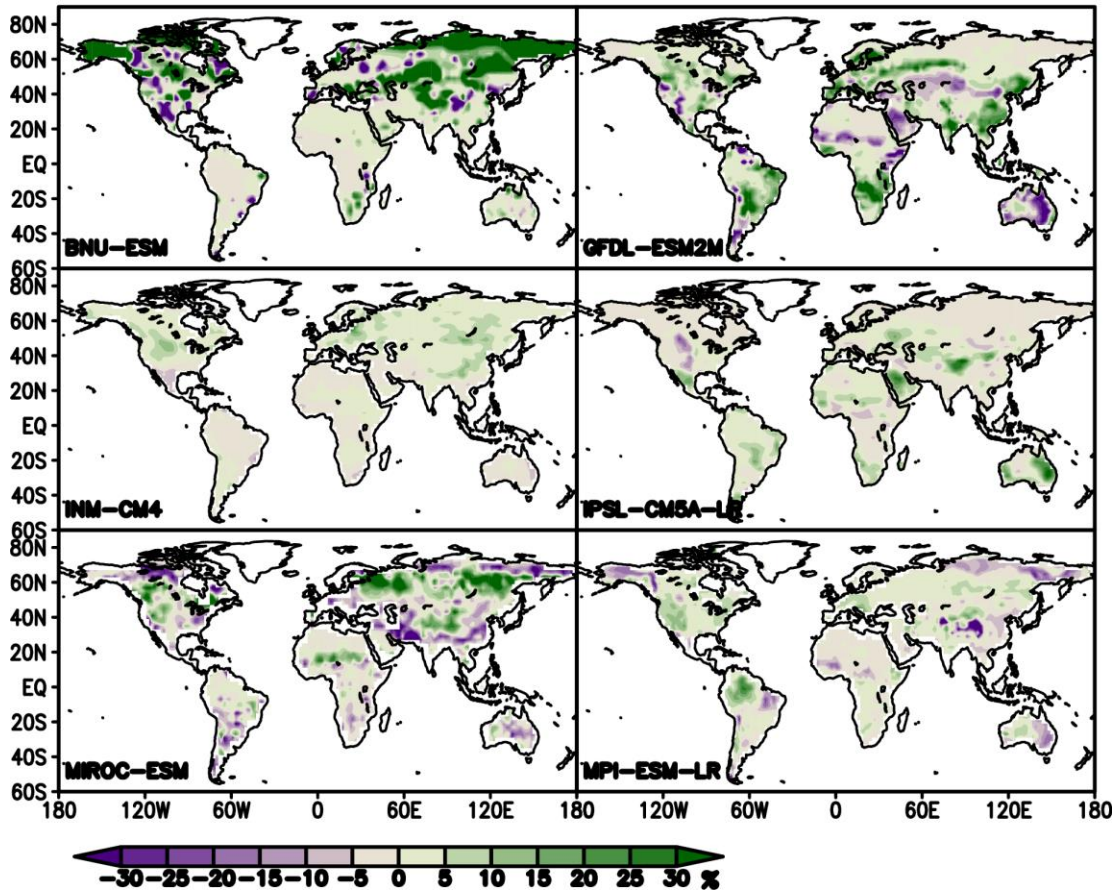


Figure 4-21: Changes of natural grass fractions between future (2081-2090) and historical (1961-1970) periods from six CMIP5 ESMs. The values represent fractional cover changes relative to the whole grid cell, instead of relative change of natural grass cover. Notable increase over the Northern high latitude regions is found for BNU-ESM.

The major crops are characterized by high productivity in a short growing season, and they tend to have larger NBP seasonal amplitude compared to the natural vegetation they replace (usually natural grass). An increase in cropland fraction over high latitude regions could contribute to the seasonal amplitude increase of NBP. As far as we know, no CMIP5 model has accounted for agricultural intensification, and only some models have implemented a conversion matrix (Brovkin et al., 2013). Therefore, the most important change implemented in the CMIP5 models is fractional

land cover change based on Hurtt et al. (2011). In Figure 4-22 we present the change of crop fraction, available from five models. It is apparent that crop area has increased

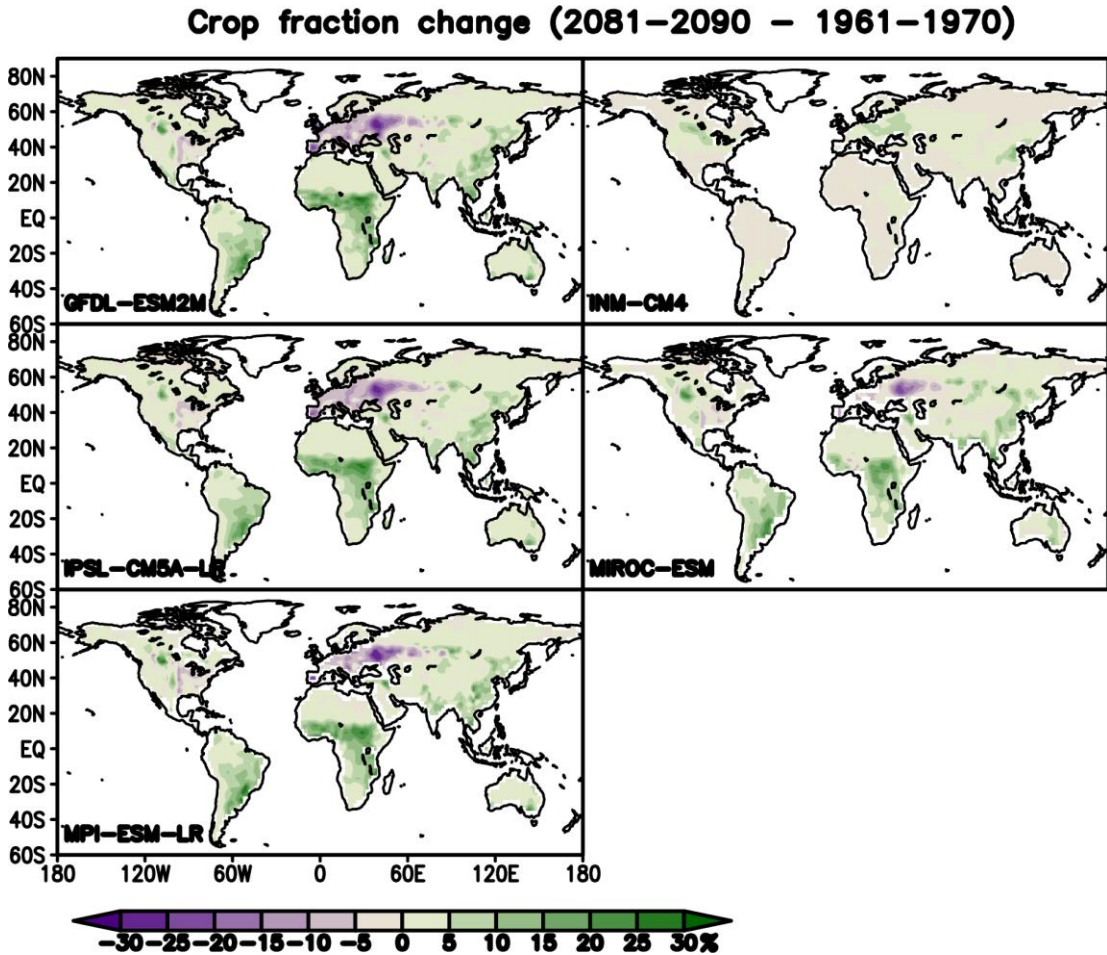


Figure 4-22: Changes of crop fraction between future (2081-2090) and historical (1961-1970) periods for five CMIP5 ESMs. Except for INM-CM4, the models show similar patterns of crop fraction change, which is expected given they are all driven by the same land cover change scenario.

mostly in the Tropics, while regions north of 30N have actually seen a decrease (due to a variety of factors: cropland abandonment, reforestation, urbanization, etc.).

Therefore, crop fractional cover change alone may decrease the NBP seasonal

amplitude in CMIP5 simulations. A better representation of land use change, especially the agricultural intensification, is needed in CMIP5 models to represent the CO₂ and NBP seasonal cycle better. On a side note, the other major part of land cover change—pasture (often treated as natural grass in ESMs, Brovkin et al., 2013) fraction change is unlikely to have a significant effect on NBP seasonal amplitude in the CMIP5 simulations.

Conclusion

Under the RCP8.5 emission scenario, all models examined in this study project an increase in seasonal amplitude of both CO₂ and NBP. The models' results indicate an earlier onset and peak of Northern Hemisphere biosphere growth and decay under future climate and CO₂ conditions. The amplitude increase is dominated by changes in net primary productivity, and changes in regions north of 45°N. Our results suggest the models simulating a larger mean carbon sink increase are likely to project a larger increase in NBP seasonal amplitude. Considerable model spread is found, likely due to different model setup and complexity, different climate conditions simulated by the models, sensitivity to CO₂ and climate and their combined effects, and strength of feedbacks. Our findings indicate factors including enhanced CO₂ fertilization and lengthening of growing season in high-latitude regions outcompetes possible severe drought and forest degradation (leading to loss of biosphere productivity) in the future.

Despite of the model consensus in global CO₂ and NBP seasonal amplitude increase, and a reasonable representation of CO₂ seasonal amplitude increase at

Mauna Loa and Point Barrow compared to surface in-situ observations, the mechanisms contributing to these changes are debatable. CO₂ fertilization may be too strong, and factors like ecosystem change and agricultural intensification are under-represented or missing in the CMIP5 ESMs. Future model-intercomparison projects should encourage models to participate in consistent and comprehensive sensitivity experiments.

Acknowledgements

We acknowledge the World Climate Research Programme's Working Group on Coupled Modeling, which is responsible for CMIP, and we thank the climate modeling groups (listed in Table 4-1 of this paper) for producing and making available their model output. For CMIP the U.S. Department of Energy's Program for Climate Model Diagnosis and Intercomparison provides coordinating support and led development of software infrastructure in partnership with the Global Organization for Earth System Science Portals. The authors also thank NOAA for providing global mean CO₂ estimates, and Yutong Pan for processing part of CMIP5 model data. We are grateful to the two anonymous reviewers for their helpful comments and suggestions. This research was supported by NOAA (NA10OAR4310248 and NA09NES4400006) and NSF (AGS-1129088).

Chapter 5: Conclusion and future perspective

Conclusions addressing main research questions

The individual studies in this dissertation examined the causes and future projections of CO₂ amplitude increase using surface observation-based estimates and ecosystem models. In Chapter 2, it was argued that land use/cover change, especially agricultural intensification, is an important driver to the observed CO₂ amplitude increase measured at Mauna Loa and surface stations worldwide. Sensitivity experiments conducted by our VEGAS model attributed the long-term trend of F_{TA} seasonal amplitude increase approximately equally to CO₂, climate, and land use/cover change (Figure 2-9). In Chapter 3, a comprehensive comparison of simulated amplitude change of carbon flux was conducted for nine terrestrial biosphere models including VEGAS. Some models were found to have serious issues in simulating the amplitude and phase of average seasonal cycle for 2001-2010 (Figure 3-1). In addition, spatial analyses highlighted considerable regional difference in the effect of CO₂, climate and land use/cover changes (Figure 3-11, Figure 3-12). For the simulated amplitude increase of F_{TA}, factorial experiments attributed 83±56%, -3±74% and 20±30% to CO₂, climate change and land use/cover change, respectively (Figure 3-9). Finally, in Chapter 4, future projections of CO₂ amplitude increase from ten fully coupled CMIP5 Earth system models were examined. Some of the CMIP5 models have terrestrial biosphere model component similar to the models analyzed in Chapter 3 (i.e., ORCHIDEE is the terrestrial biosphere model component of IPSL-CM5A-LR). The CMIP5 models projected an increase of CO₂ seasonal amplitude by

about 70% for 1961-2090 (Figure 4-1), and most models exhibited a relatively linear CO₂ amplitude increase throughout that long period (Figure 4-2).

Detailed conclusions addressing the main research questions outlined in Chapter 1 are presented below:

1. Is the observed CO₂ amplitude increase sufficiently explained by the effects of CO₂ fertilization and climate change?

Agricultural intensification, especially over the Northern mid-latitude regions (Figure 2-6), is also an important driver to the observed CO₂ amplitude increase measured at Mauna Loa and other surface stations (Chapter 2). The VEGAS model is the only terrestrial biosphere model that simulates the tripling of agricultural production through time-varying management intensity and harvest index (Figure 2-10). According to VEGAS, the large increase in cropland productivity accounted for 45% of global F_{TA} amplitude increase, higher than the effect of CO₂ fertilization and high latitude warming (Table 2-2). One reason was enhanced crop productivity driven by agricultural intensification, which was reflected by large trend of NPP increase over cropland area (Figure 2-7). Similarly, satellite-based estimate of Normalized Difference Vegetation Index (NDVI) also showed greatest increasing rate for 1981-2010 over cropland and other intensely used land classes (Mueller et al., 2014). Another reason was that crops on these intensively managed land demonstrated a narrower growing season with higher peak productivity compared to nearby natural vegetation (Figure 2-1 inset, Miles et al., 2012). Therefore, cropland could contribute

significantly to the amplification of global F_{TA} amplitude, even though it only covers about 20% of land area in Northern mid-latitude.

In addition to change in land use management practices, land cover change also had noticeable effect on global F_{TA} amplitude, reducing the trend of global F_{TA} amplitude increase by 17% in VEGAS. This was because of a decrease in cropland area north of 30N due to a variety of factors: cropland abandonment, reforestation, urbanization, etc., where the seasonal cycle of carbon flux over cropland had higher amplitude than the natural ecosystem it replaces. However, five of eight other TRENDY terrestrial biosphere models (except VEGAS, the TRENDY models do not simulate change in land use management) suggested land cover change would actually increase global F_{TA} amplitude, as demonstrated by sensitivity experiment results (Chapter 3). While land use/cover change on average accounted for 20% of global F_{TA} amplitude increase in the nine TRENDY models, the spatial contribution was notably different (Figure 3-12), suggesting varied model mechanisms. In many of the models, cropland was treated as natural grassland, and whether land conversion would increase or decrease F_{TA} amplitude depended on the difference in seasonal carbon flux between the old and new vegetation cover. For example, for some models (CLM4.5BGC, LPJ, ORCHIDEE), reforestation in the eastern U.S. led to increase in F_{TA} amplitude, whereas for some other models (LPX-Bern, VEGAS, VISIT), such process resulted in F_{TA} amplitude reduction. Overall, results in this research demonstrated that change in land use management and land cover should both be considered in explaining the observed CO_2 amplitude increase.

2. Can the latest generation of terrestrial ecosystem models capture the seasonal characteristics of global carbon cycle?

Several terrestrial ecosystem models had issues in simulating even the basic characteristics of global F_{TA} seasonal cycle (Chapter 3). Five of the nine models examined underestimated the amplitude of the F_{TA} seasonal cycle by about 50% compared to atmospheric inversions, and some models (ISAM, JULES, LPJ) had the tendency to rebound too early in mid-summer, possibly due to the strong exponential response of soil respiration to temperature increase. Similarly, the ORCHIDEE model exhibited F_{TA} seasonal amplitude over the tropical regions five times as high as the multi-model median and atmospheric inversions. Even for the three models (CLM4.5BGC, LPX-Bern, VEGAS) that agreed broadly with atmospheric inversions, the underlying mechanisms and spatial patterns were substantially different (Figure 3-12, 3-S2, 3-S3). The comparison results suggested that at most one, possibly none of the terrestrial ecosystem models correctly captures the seasonal characteristics of global carbon cycle for the right reasons.

Previous studies (Keeling et al., 1996; Graven et al., 2013) suggested warming over high latitude regions could result in lengthening of growing season and changes in ecosystem composition and structure, and therefore contributing to the F_{TA} amplitude increase. Aircraft measurements showed the amplitude increase was larger at higher latitude (Graven et al., 2013), supporting the role of high latitude warming. However, factorial experiments showed that climate change effect in the TRENDY models on average exhibited a near neutral ($-3 \pm 74\%$) effect on global F_{TA} amplitude. The reason was that the enhanced vegetation activity in the high latitude was offset by

the reduced seasonality in the mid-latitude regions, possibly due to mid-latitude droughts (Buermann et al., 2007). While all the models simulated both mechanisms (Figure 3-11), the models' climate sensitivity varied, and as a result, the simulated net effect of climate change on global F_{TA} amplitude was largely divided. Instead, CO_2 fertilization exhibited a dominant role on global F_{TA} amplitude increase ($83 \pm 56\%$), much higher than the upper limit of earlier estimate (Kohlmaier et al., 1987). Since the effect of CO_2 fertilization is proportional to gross assimilation rate of vegetation, a dominant CO_2 fertilization effect was unlikely to fully explain the latitudinal gradient of F_{TA} amplitude increase, further suggesting terrestrial biosphere models need further improvement in order to capture the seasonal characteristics of global carbon cycle.

3. Will the atmospheric CO_2 amplitude—indicator of terrestrial ecosystem activities—continues to increase in the future?

According to results from the CMIP5 Earth system models (Chapter 4), the atmospheric CO_2 amplitude would continue to increase almost linearly in the future, to about 70% higher than 1960s by the end of this century (Figure 4-1, Figure 4-2). As revealed by TRENDY's (Chapter 3) and CMIP5's sensitivity experiments results (Figure 4-6, Figure 4-7), this continuing amplitude increase was likely due to the dominant role of CO_2 fertilization effect under the business-as-usual high carbon emission scenario. In addition, the F_{TA} amplitude increase was mostly attributable to higher vegetation productivity (enhanced NPP) during peak growing season (Figure 4-3), and over most land area over 45N (Figure 4-4). The strong CO_2 fertilization

effect also overcame increased respiration for the 1961-2099 period (except for MIROC-ESM, a model with high climate sensitivity that showed little change in F_{TA} amplitude after 2080). In general, the CO_2 amplitude increase in the CMIP5 model simulations showed little sign of slowing down, suggesting the models might be too optimistic and may lack important negative feedbacks such as soil depletion of essential nutrients (such as nitrogen and phosphorous), excessive warming/drought, air/water pollution, and many other factors related to the intensive activity of increasing human population and development. Similar to TRENDY models (Chapter 3), CO_2 fertilization effect in the CMIP5 models was probably too strong at ecosystem level. Additionally, the CMIP5 model simulations did not include agricultural intensification presented in our VEGAS model (Chapter 2). Agricultural intensification was likely an important reason for the historical CO_2 amplitude increase, and crop yield recently showed signs of stagnation (Ray et al., 2012). Therefore, if a weaker CO_2 fertilization effect is closer to reality, large increase in atmospheric CO_2 amplitude is unlikely to occur in the future.

Additional findings from the dissertation

Questions regarding the relationship with terrestrial carbon sink and model-data inconsistency also gave rise to two unique findings below:

First, both the CMIP5 and TRENDY models showed a moderate cross-model correlation between simulated increase in global land carbon sink ($-F_{TA}$) and increase in global F_{TA} amplitude (Figure 3-13, Figure 4-9). This relationship suggested that a larger increase in global land carbon sink is usually accompanied by a larger F_{TA}

amplitude increase in model simulation, most likely due to a stronger peak of growing season. Considering that most models showed strong CO₂ fertilization effect, enhanced vegetation gross rate under elevated CO₂ likely caused both increased carbon sink and stronger peak growing season. One tantalizing possibility is to use observed atmospheric CO₂ seasonal cycle as an additional observational constraint for the future land carbon sink. As previous studies (Randerson et al., 1997; Graven et al., 2013) suggested, terrestrial carbon fluxes contribute about 90% to the seasonal cycle of CO₂. While the inventory-based estimate of residual land carbon sink is subject to large uncertainty range (Figure 3-13), atmospheric CO₂ measurement in general is better constrained. However, additional analyses have to be performed first in order to better understand the representativeness of surface CO₂ stations, and in particular, to what extent can Mauna Loa CO₂ observation represent the global average CO₂.

Second, comparison of CMIP5 simulated CO₂ with measurements at surface stations revealed a major difference in CO₂ amplitude observed at surface and a higher (3-6 km) altitude. Aircraft CO₂ measurements at high altitude suggested a much larger amplitude increase (over 1% y⁻¹) than the amplitude increase of surface CO₂ observation at Point Barrow, Alaska (0.4-0.6 % y⁻¹, depending on the time period and data source, in-situ or flask measurements). We showed the most consistent comparison between simulated and observed CO₂ for 1974-2005 at Point Barrow and for 1959-2005 at Mauna Loa, both displaying no obvious underestimation in simulated amplitude increase (Figure 4-12, Figure 4-14). It is a major mystery why aircraft measurements show much larger amplitude increase than

surface observations, suggesting more observation and analyses are necessary. Most of the models did show an underestimation of CO₂ amplitude averaged over 2001-2005, similar to the underestimation of global F_{TA} amplitude (Figure 3-1), suggesting possible model deficiencies.

Future research directions

It is “almost inevitable” that the world population will rise from 7.3 billion today to 9.7 billion in 2050, according to latest UN projections (United Nations, 2015). The increase in population and larger ecological footprint per capita would potentially further alter the environment. As suggested in this work, in general the current models’ representation of the agricultural system is insufficient and seems to lack negative feedbacks. In order to produce realistic future simulations until the end of this century or longer, it is necessary for the global models to have a bidirectional coupling of the human-earth system.

Efforts expanding our data collection both spatially and temporally would be crucial for continuous monitoring, better understanding and informed projection of global carbon cycle. Several recent observation campaigns (i.e., the Next-Generation Ecosystem Experiments in the arctic and tropics) have already taken place, and they will hopefully reduce uncertainties of model parameterizations in these regions. Similarly, continuous data collection from satellite CO₂ measurements (i.e., SCIAMACHY, GOSAT and OCO-2) can be cross validated with ground and aircraft observation, providing much needed better data constraints both spatially and temporally. In order to monitor and understand ecosystem changes, priority should be

given to ensure consistent long-term observations. After analyzing data from different sources, regions with high uncertainty can be identified, which will improve the efficiency of future experiments.

The accumulation and advanced processing (i.e., the Multi-Tree Ensemble of FLUXNET data in Jung et al., 2009) of observation and observation-based datasets have facilitated better assessment and comparison of different models. The recent model intercomparison projects (TRENDY, MsTMIP, ISI-MIP, etc.) has also provided opportunity to evaluate models under a consistent framework, which is helpful for further data-model integrations and assessing ecosystem changes and impacts. However, as indicated in this work, more effort should be invested in interpreting the model results. Because of the large model spread in simulating the terrestrial carbon cycle, the traditional approach of leaning heavily on model ensemble mean may risk burying important details from individual model, especially if individual model results are not displayed. For smaller model groups, it is challenging to participate in all the model intercomparison projects and have a wide representation. Therefore, better coordination among different projects and improved experiment design should be explored to encourage participation of more modeling groups.

In an effort to improve model's performance, the VEGAS model was improved with a new crop scheme, better high latitude representation, snow scheme and Gregorian calendar during the participation of MsTMIP and TRENDY projects. Current and planned model development work involves applying data assimilation for better parameter estimation and simulation of vegetation diurnal cycle. These

improvements will provide foundation for refining crop simulation, along with recently available yield and fractional cover data for key crop types (Ray et al., 2012). Currently there is one generic crop type in the model, which may not capture the seasonal cycle of some crops like winter wheat, leading to a possible overestimation of the agricultural intensification effect. Adding an additional crop functional type could improve overall crop simulation without over complicating the model, and it warrants interesting future work.

One important feature highlighted in this work is weak CO₂ fertilization in VEGAS, which has been discussed previously in the Friedlingstein et al. (2006) C4MIP (Coupled Carbon Cycle Climate Model Intercomparison Project) study. This feature represents our opinion that weaker CO₂ fertilization may be more likely than strong CO₂ fertilization represented in some other models. To verify this scenario, we may need additional observational evidence. If this is true, then we have to rethink not only the future projection of CO₂ amplitude increase, but also the fate of future land carbon sink. If the land ecosystems cannot take up as much CO₂, or even release CO₂ in future, then the rate of atmospheric CO₂ increase and thus warming of the climate could be much faster. Such knowledge is very useful and have significant policy implications.

Bibliography

Ainsworth, E. a. and Long, S. P.: What have we learned from 15 years of free-air CO₂ enrichment (FACE)? A meta-analytic review of the responses of photosynthesis, canopy properties and plant production to rising CO₂, *New Phytol.*, 165(2), 351–372, doi:10.1111/j.1469-8137.2004.01224.x, 2005.

Anav, A., Friedlingstein, P., Kidston, M., Bopp, L., Ciais, P., Cox, P., Jones, C., Jung, M., Myrneni, R. and Zhu, Z.: Evaluating the Land and Ocean Components of the Global Carbon Cycle in the CMIP5 Earth System Models, *J. Clim.*, 26(18), 6801–6843, doi:10.1175/JCLI-D-12-00417.1, 2013.

Andres, R. J., Gregg, J. S., Losey, L., Marland, G. and Boden, T. A.: Monthly, global emissions of carbon dioxide from fossil fuel consumption, *Tellus B*, 63(3), 309–327, doi:10.1111/j.1600-0889.2011.00530.x, 2011.

Arora, V. K., Boer, G. J., Friedlingstein, P., Eby, M., Jones, C. D., Christian, J. R., Bonan, G., Bopp, L., Brovkin, V., Cadule, P., Hajima, T., Ilyina, T., Lindsay, K., Tjiputra, J. F. and Wu, T.: Carbon–Concentration and Carbon–Climate Feedbacks in CMIP5 Earth System Models, *J. Clim.*, 26(15), 5289–5314, doi:10.1175/JCLI-D-12-00494.1, 2013.

Arora, V. K., Scinocca, J. F., Boer, G. J., Christian, J. R., Denman, K. L., Flato, G. M., Kharin, V. V., Lee, W. G. and Merryfield, W. J.: Carbon emission limits required to satisfy future representative concentration pathways of greenhouse gases, *Geophys. Res. Lett.*, 38(5), L05805, doi:10.1029/2010GL046270, 2011.

Bacastow, R. B., Keeling, C. D. and Whorf, T. P.: Seasonal amplitude increase in atmospheric CO₂ concentration at Mauna Loa, Hawaii, 1959–1982, *J. Geophys. Res.*, 90(D6), 10529–10540, doi:10.1029/JD090iD06p10529, 1985.

Baptist, F., Flahaut, C., Streb, P. and Choler, P.: No increase in alpine snowbed productivity in response to experimental lengthening of the growing season, *Plant Biol.*, 12(5), 755–764, doi:10.1111/j.1438-8677.2009.00286.x, 2010.

Bazzaz, F.: The Response of Natural Ecosystems to the Rising Global CO₂ Levels, *Annu. Rev. Ecol. Syst.*, 21(1), 167–196, doi:10.1146/annurev.es.21.110190.001123, 1990.

Bondeau, A., Smith, P. C., Zaehle, S., Schaphoff, S., Lucht, W., Cramer, W., Gerten, D., Lotze-Campen, H., Müller, C., Reichstein, M. and Smith, B.: Modelling the role of agriculture for the 20th century global terrestrial carbon balance, *Glob. Chang. Biol.*, 13(3), 679–706, doi:10.1111/j.1365-2486.2006.01305.x, 2007.

Brovkin, V., Boysen, L., Arora, V. K., Boisier, J. P., Cadule, P., Chini, L., Claussen, M., Friedlingstein, P., Gayler, V., van den Hurk, B. J. J. M., Hurtt, G. C., Jones, C. D., Kato, E., de Noblet-Ducoudré N., Pacifico, F., Pongratz, J. and Weiss, M.: Effect of Anthropogenic Land-Use and Land-Cover Changes on Climate and Land Carbon Storage in CMIP5 Projections for the Twenty-First Century, *J. Clim.*, 26(18), 6859–6881, doi:10.1175/JCLI-D-12-00623.1, 2013.

Buermann, W., Bikash, P. R., Jung, M., Burn, D. H. and Reichstein, M.: Earlier springs decrease peak summer productivity in North American boreal forests, *Environ. Res. Lett.*, 8(2), 024027, doi:10.1088/1748-9326/8/2/024027, 2013.

Buermann, W., Lintner, B. R., Koven, C. D., Angert, A., Pinzon, J. E., Tucker, C. J. and Fung, I. Y.: The changing carbon cycle at Mauna Loa Observatory, *Proc. Natl. Acad. Sci. U. S. A.*, 104(11), 4249–4254, 2007.

Cadule, P., Friedlingstein, P., Bopp, L., Sitch, S., Jones, C. D., Ciais, P., Piao, S. L. and Peylin, P.: Benchmarking coupled climate-carbon models against long-term atmospheric CO₂ measurements, *Global Biogeochem. Cycles*, 24(2), n/a–n/a, doi:10.1029/2009GB003556, 2010.

Ciais, P., Bousquet, P., Freibauer, A. and Naegler, T.: Horizontal displacement of carbon associated with agriculture and its impacts on atmospheric CO₂, *Global Biogeochem. Cycles*, 21(2), 1–12, doi:10.1029/2006gb002741, 2007.

Clark, D. B., Mercado, L. M., Sitch, S., Jones, C. D., Gedney, N., Best, M. J., Pryor, M., Rooney, G. G., Essery, R. L. H., Blyth, E., Boucher, O., Harding, R. J., Huntingford, C. and Cox, P. M.: The Joint UK Land Environment Simulator (JULES), model description – Part 2: Carbon fluxes and vegetation dynamics, *Geosci. Model Dev.*, 4(3), 701–722, doi:10.5194/gmd-4-701-2011, 2011.

Cleveland, W., Freeny, A. E. and Graedel, T. E.: The Seasonal Component of Atmospheric CO₂: Information From New Approaches to the Decomposition of Seasonal Time Series, *J. Geophys. Res.*, 88(C15), 10934–10946, 1983.

Conway, T. J., Tans, P. P., Waterman, L. S., Thoning, K. W., Kitzis, D. R., Masarie, K. A. and Zhang, N.: Evidence for interannual variability of the carbon cycle from the National Oceanic and Atmospheric Administration / Climate Monitoring and Diagnostics Laboratory Global Air Sampling Network, *J. Geophys. Res.*, 99(D11), 22831–22855, 1994.

Cramer, W., Kicklighter, D. W., Bondeau, A., Iii, B. M., Cedex, F.-O., Haxeltine, A., Heimann, M., Hoffstadt, J., Kaduk, J., Kergoat, L., Knorr, W., Kohlmaier, G., Lurin, B., Prince, S., Randerson, J., Rasool, I., Rizzo, B., Ruimy, A., Running, S., Sahagian, D. and Saugier, B.: Comparing global models of terrestrial net primary productivity (NPP): overview and key results, *Global Change Biology*, 5, 1999.

Curtis, P. S., Drake, B. G. and Whigham, D. F.: OL colgia Nitrogen and carbon dynamics in C3 and C4 estuarine marsh plants grown under elevated CO₂ in situ, *Oecologia*, 78, 297–301, 1989.

DeLucia, E. H., Moore, D. J. and Norby, R. J.: Contrasting responses of forest ecosystems to rising atmospheric CO₂: Implications for the global C cycle, *Global Biogeochem. Cycles*, 19(3), 1–9, doi:10.1029/2004GB002346, 2005.

Drake, B. G., Gonzalez-Meler, M. a. and Long, S. P.: MORE EFFICIENT PLANTS: A Consequence of Rising Atmospheric CO₂?, *Annu. Rev. Plant Physiol. Plant Mol. Biol.*, 48, 609–639, doi:10.1146/annurev.arplant.48.1.609, 1997.

Dufresne, J.-L., Foujols, M. -a., Denvil, S., Caubel, A., Marti, O., Aumont, O., Balkanski, Y., Bekki, S., Bellenger, H., Benshila, R., Bony, S., Bopp, L., Braconnot, P., Brockmann, P., Cadule, P., Cheruy, F., Codron, F., Cozic, A., Cugnet, D., Noblet, N., Duvel, J.-P., Ethé C., Fairhead, L., Fichefet, T., Flavoni, S., Friedlingstein, P., Grandpeix, J.-Y., Guez, L., Guilyardi, E., Hauglustaine, D., Hourdin, F., Idelkadi, A., Ghattas, J., Joussaume, S., Kageyama, M., Krinner, G., Labetoulle, S., Lahellec, A., Lefebvre, M.-P., Lefevre, F., Levy, C., Li, Z. X., Lloyd, J., Lott, F., Madec, G., Mancip, M., Marchand, M., Masson, S., Meurdesoif, Y., Mignot, J., Musat, I., Parouty, S., Polcher, J., Rio, C., Schulz, M., Swingedouw, D., Szopa, S., Talandier, C., Terray, P. and Viovy, N.: Climate change projections using the IPSL-CM5 Earth System Model: from CMIP3 to CMIP5, *Clim. Dyn.*, 40(9-10), 2123–2165, doi:10.1007/s00382-012-1636-1, 2013.

Dukes, J. S., Chiariello, N. R., Cleland, E. E., Moore, L. a., Rebecca Shaw, M., Thayer, S., Tobeck, T., Mooney, H. a. and Field, C. B.: Responses of grassland production to single and multiple global environmental changes, *PLoS Biol.*, 3(10), doi:10.1371/journal.pbio.0030319, 2005.

Dunne, J. P., John, J. G., Shevliakova, E., Stouffer, R. J., Krasting, J. P., Malyshev, S. L., Milly, P. C. D., Sentman, L. T., Adcroft, A. J., Cooke, W., Dunne, K. A., Griffies, S. M., Hallberg, R. W., Harrison, M. J., Levy, H., Wittenberg, A. T., Phillips, P. J. and Zadeh, N.: GFDL's ESM2 Global Coupled Climate–Carbon Earth System Models. Part II: Carbon System Formulation and Baseline Simulation Characteristics*, *J. Clim.*, 26(7), 2247–2267, doi:10.1175/JCLI-D-12-00150.1, 2013.

Field, C. B., Randerson, J. T. and Malmström, C. M.: Global net primary production: Combining ecology and remote sensing, *Remote Sens. Environ.*, 51(1), 74–88, doi:10.1016/0034-4257(94)00066-V, 1995.

Friedlingstein, P., Cox, P., Betts, R., Bopp, L., Von Bloh, W., Brovkin, V., Cadule, P., Doney, S., Eby, M., Fung, I., Bala, G., John, J., Jones, C., Joos, F., Kato, T., Kawamiya, M., Knorr, W., Lindsay, K., Matthews, H. D., Raddatz, T., Rayner, P., Reick, C., Roeckner, E., Schnitzler, K. G., Schnur, R., Strassmann, K., Weaver, A. J., Yoshikawa, C. and Zeng, N.: Climate-carbon cycle feedback analysis: Results from the C⁴MIP model intercomparison, *J. Clim.*, 19, 3337–3353, doi:10.1175/jcli3800.1, 2006.

Friedlingstein, P., Meinshausen, M., Arora, V. K., Jones, C. D., Anav, A., Liddicoat, S. K. and Knutti, R.: Uncertainties in CMIP5 climate projections due to carbon cycle feedbacks, *J. Clim.*, 27, 511–526, doi:10.1175/JCLI-D-12-00579.1, 2013.

Fung, I. Y., Tucker, C. J. and Prentice, K. C.: Application of Advanced Very High Resolution Radiometer vegetation index to study atmosphere-biosphere exchange of CO₂, *J. Geophys. Res.*, 92(D3), 2999–3015, doi:10.1029/JD092iD03p02999, 1987.

Gedalof, Z. and Berg, A. a.: Tree ring evidence for limited direct CO₂ fertilization of forests over the 20th century, *Global Biogeochem. Cycles*, 24(3), 2–7, doi:10.1029/2009GB003699, 2010.

Gervois, S., de Noblet-Ducoudré N., Viovy, N., Ciais, P., Brisson, N., Seguin, B. and Perrier, A.: Including Croplands in a Global Biosphere Model: Methodology and Evaluation at Specific Sites, *Earth Interact.*, 8(16), 1–25, doi:10.1175/1087-3562(2004)8<1:ICIAGB>2.0.CO;2, 2004.

Graven, H. D., Keeling, R. F., Piper, S. C., Patra, P. K., Stephens, B. B., Wofsy, S. C., Welp, L. R., Sweeney, C., Tans, P. P., Kelley, J. J., Daube, B. C., Kort, E. a, Santoni, G. W. and Bent, J. D.: Enhanced Seasonal Exchange of CO₂ by Northern Ecosystems Since 1960., *Science*, 341, 1085–1089, doi:10.1126/science.1239207, 2013.

Gray, J. M., Frohking, S., Kort, E. a., Ray, D. K., Kucharik, C. J., Ramankutty, N. and Friedl, M. a.: Direct human influence on atmospheric CO₂ seasonality from increased cropland productivity, *Nature*, 515(7527), 398–401, doi:10.1038/nature13957, 2014.

Guanter, L., Zhang, Y., Jung, M., Joiner, J., Voigt, M., Berry, J. a, Frankenberg, C., Huete, A. R., Zarco-Tejada, P., Lee, J.-E., Moran, M. S., Ponce-Campos, G., Beer, C., Camps-Valls, G., Buchmann, N., Gianelle, D., Klumpp, K., Cescatti, A., Baker, J. M. and Griffis, T. J.: Global and time-resolved monitoring of crop photosynthesis with chlorophyll fluorescence., *Proc. Natl. Acad. Sci. U. S. A.*, 111(14), E1327–33, doi:10.1073/pnas.1320008111, 2014.

Gurney, K. R. and Eckels, W. J.: Regional trends in terrestrial carbon exchange and their seasonal signatures, *Tellus B*, 63(3), 328–339, doi:10.1111/j.1600-0889.2011.00534.x, 2011.

Haberl, H., Erb, K. H., Krausmann, F., Gaube, V., Bondeau, A., Plutzer, C., Gingrich, S., Lucht, W. and Fischer-Kowalski, M.: Quantifying and mapping the human appropriation of net primary production in earth's terrestrial ecosystems., *Proc. Natl. Acad. Sci. U. S. A.*, 104(31), 12942–7, doi:10.1073/pnas.0704243104, 2007.

Hall, C. A. S., Ekdahl, C. A. and Wartenberg, D. E.: A fifteen-year record of biotic metabolism in the Northern Hemisphere, *Nature*, 255, 136–138, doi:10.1038/255136a0, 1975.

Harris, F. J.: On the use of windows for harmonic analysis with the discrete Fourier transform, *Proc. IEEE*, 66(1), 51–83, doi:10.1109/PROC.1978.10837, 1978.

Heimann, M.: *The Changing Carbon Cycle, a Global Analysis*, edited by J. R. Trabalka and D. E. Reichle, Springer New York, New York, NY., 1986.

Hoffman, F. M., Randerson, J. T., Arora, V. K., Bao, Q., Cadule, P., Ji, D., Jones, C. D., Kawamiya, M., Khatiwala, S., Lindsay, K., Obata, A., Shevliakova, E., Six, K. D., Tjiputra, J. F., Volodin, E. M. and Wu, T.: Causes and implications of persistent

atmospheric carbon dioxide biases in Earth System Models, *J. Geophys. Res. Biogeosciences*, 119(2), 141–162, doi:10.1002/2013JG002381, 2014.

Huntzinger, D. N., Schwalm, C., Michalak, a. M., Schaefer, K., King, a. W., Wei, Y., Jacobson, a., Liu, S., Cook, R. B., Post, W. M., Berthier, G., Hayes, D., Huang, M., Ito, a., Lei, H., Lu, C., Mao, J., Peng, C. H., Peng, S., Poulter, B., Ricciuto, D., Shi, X., Tian, H., Wang, W., Zeng, N., Zhao, F. and Zhu, Q.: The North American Carbon Program Multi-Scale Synthesis and Terrestrial Model Intercomparison Project – Part 1: Overview and experimental design, *Geosci. Model Dev.*, 6(6), 2121–2133, doi:10.5194/gmd-6-2121-2013, 2013.

Hurtt, G. C., Chini, L. P., Frohking, S., Betts, R. a, Feddema, J., Fischer, G., Fisk, J. P., Hibbard, K., Houghton, R. a, Janetos, a, Jones, C. D., Kindermann, G., Kinoshita, T., Klein Goldewijk, K., Riahi, K., Shevliakova, E., Smith, S., Stehfest, E., Thomson, a, Thornton, P., Van Vuuren, D. P. and Wang, Y. P.: Harmonization of land-use scenarios for the period 1500-2100: 600 years of global gridded annual land-use transitions, wood harvest, and resulting secondary lands, *Clim. Change*, 109(1), 117–161, doi:10.1007/s10584-011-0153-2, 2011.

Ilyina, T., Six, K. D., Segschneider, J., Maier-reimer, E., Li, H. and Núñez-Riboni, I.: Global ocean biogeochemistry model HAMOCC: Model architecture and performance as component of the MPI-Earth system model in different CMIP5 experimental realizations, *J. Adv. Model. Earth Syst.*, 5, 287–315, doi:10.1029/2012MS000178, 2013.

Imhoff, M. L., Bounoua, L., Ricketts, T., Loucks, C., Harriss, R. and Lawrence, W. T.: Global patterns in human consumption of net primary production, *Nature*, 429, 870–873, doi:10.1038/nature02685.Published, 2004.

International Panel on Climate Change: *Climate Change 2013: the Physical Science Basis. Working Group 1 Contribution to the Fifth Assessment Report of the International Panel on Climate Change International Panel on Climate Change*, Cambridge University Press, Cambridge, New York., 2013.

Ito, A., Inatomi, M., Deborah N. Huntzinger, Christopher Schwalm, Anna M. Michalak, R. C., King, A. W., Mao, J., Wei, Y., Wang, W., Arain, M. A., Hayes, D. J., Huang, M., Tian, H., Lu, C., Yang, J., Tao, B., Ricciuto, D., Jain, A., Poulter, B., Peng, S., Ciais, P., Parazoo, N., Fisher, J. B., Schaefer, K., Peng, C., Zeng, N., Zhao, F., Lei, H. and Post, W. Mac: Decadal trends in seasonal amplitude of terrestrial CO₂ exchange: an analysis of MsTMIP, *Tellus B*, Submitted, 2015.

Jain, A. K., Meiyappan, P., Song, Y. and House, J. I.: CO₂ emissions from land-use change affected more by nitrogen cycle, than by the choice of land-cover data., *Glob. Chang. Biol.*, 19(9), 2893–906, doi:10.1111/gcb.12207, 2013.

Jain, H. K.: *The Green Revolution: History, Impact and Future*, 2010.

Ji, D., Wang, L., Feng, J., Wu, Q., Cheng, H., Zhang, Q., Yang, J., Dong, W., Dai, Y., Gong, D., Zhang, R.-H., Wang, X., Liu, J., Moore, J. C., Chen, D. and Zhou, M.: Description and basic evaluation of BNU-ESM version 1, *Geosci. Model Dev.*, 7, 2039–2064, doi:10.5194/gmdd-7-1601-2014, 2014.

Joiner, J., Guanter, L., Lindstrot, R., Voigt, M., Vasilkov, a. P., Middleton, E. M., Huemmrich, K. F., Yoshida, Y. and Frankenberg, C.: Global monitoring of terrestrial chlorophyll fluorescence from moderate-spectral-resolution near-infrared satellite measurements: methodology, simulations, and application to GOME-2, *Atmos. Meas. Tech.*, 6(10), 2803–2823, doi:10.5194/amt-6-2803-2013, 2013.

Joos, F. and Spahni, R.: Rates of change in natural and anthropogenic radiative forcing over the past 20,000 years., *Proc. Natl. Acad. Sci. U. S. A.*, 105(5), 1425–30, doi:10.1073/pnas.0707386105, 2008.

Jung, M., Reichstein, M. and Bondeau, A.: Towards global empirical upscaling of FLUXNET eddy covariance observations: validation of a model tree ensemble approach using a biosphere model, *Biogeosciences*, 6, 2001–2013 [online] Available from: <Go to ISI>://WOS:000271354900005, 2009.

Kaminski, T., Giering, R. and Heimann, M.: Sensitivity of the seasonal cycle of CO₂ at remote monitoring stations with respect to seasonal surface exchange fluxes determined with the adjoint of an atmospheric transport model, *Phys. Chem. Earth*, 21(5-6), 457–462, 1996.

Kato, E., Kinoshita, T., Ito, A., Kawamiya, M. and Yamagata, Y.: Evaluation of spatially explicit emission scenario of land-use change and biomass burning using a process-based biogeochemical model, *J. Land Use Sci.*, 8(1), 104–122, doi:10.1080/1747423X.2011.628705, 2013.

Keeling, C. D., Chin, J. F. S. and Whorf, T. P.: Increased activity of northern vegetation inferred from atmospheric CO₂ measurements, *Nature*, 382, 146–149, doi:10.1038/382146a0, 1996.

Keeling, C. D., Whorf, T. P., Wahlen, M. and van der Plichtt, J.: Interannual extremes in the rate of rise of atmospheric carbon dioxide since 1980, *Nature*, 375, 666–670, doi:10.1038/375666a0, 1995.

Keenan, T., Gray, J. and Friedl, M.: Net carbon uptake has increased through warming-induced changes in temperate forest phenology, *Nat. Clim. Chang.*, 4, 598–604, doi:10.1038/NCLIMATE2253, 2014.

Klein Goldewijk, K., Beusen, A., Van Drecht, G. and De Vos, M.: The HYDE 3.1 spatially explicit database of human-induced global land-use change over the past 12,000 years, *Glob. Ecol. Biogeogr.*, 20(1), 73–86, doi:10.1111/j.1466-8238.2010.00587.x, 2011.

Klironomos, J. N., Allen, M. F., Rillig, M. C., Piotrowski, J., Makvandi-Nejad, S., Wolfe, B. E. and Powell, J. R.: Abrupt rise in atmospheric CO₂ overestimates community response in a model plant-soil system., *Nature*, 433(7026), 621–624, doi:10.1038/nature03268, 2005.

Kohlmaier, B. G. H., Brohl, H. and Sire, E. O.: Modelling stimulation of plants and ecosystem response to present levels of excess atmospheric CO₂, *Tellus*, 39B, 155–170, 1987.

Kohlmaier, G. H., Siré E. O., Janecek, A., Keeling, C. D., Piper, S. C. and Revelle, R.: Modelling the seasonal contribution of a CO₂ fertilization effect of the terrestrial vegetation to the amplitude increase in atmospheric CO₂ at Mauna Loa Observatory, *Tellus Ser. B-Chemical Phys. Meteorol.*, 41, 487–510, doi:10.1111/j.1600-0889.1989.tb00137.x, 1989.

Korner, C.: Biosphere responses to CO₂ enrichment, *Ecol. Appl.*, 10(6), 1590–1619, doi:10.1890/1051-0761(2000)010[1590:BRTCE]2.0.CO;2, 2000.

Krinner, G., Viovy, N., de Noblet-Ducoudré N., Ogée, J., Polcher, J., Friedlingstein, P., Ciais, P., Sitch, S. and Prentice, I. C.: A dynamic global vegetation model for studies of the coupled atmosphere-biosphere system, *Global Biogeochem. Cycles*, 19(1), 1–33, doi:10.1029/2003GB002199, 2005.

Kucharik, C. J. and Brye, K. R.: Plant and Environment Interactions Integrated Biosphere Simulator (IBIS) Yield and Nitrate Loss Predictions for Wisconsin Maize Receiving Varied Amounts of Nitrogen Fertilizer, , 247–268, 2003.

Long, M. C., Lindsay, K., Peacock, S., Moore, J. K. and Doney, S. C.: Twentieth-Century Oceanic Carbon Uptake and Storage in CESM1(BGC)*, *J. Clim.*, 26(18), 6775–6800, doi:10.1175/JCLI-D-12-00184.1, 2013.

Masarie, K. A. and Tans, P. P.: Extension and integration of atmospheric carbon dioxide data into a globally consistent measurement record, *J. Geophys. Res.*, 100(D6), 11593, doi:10.1029/95JD00859, 1995.

McGuire, A. D., Sitch, S., Clein, J. S., Dargaville, R., Esser, G., Foley, J., Heimann, M., Joos, F., Kaplan, J., Kicklighter, D. W., Meier, R. a, Melillo, J. M., Moore III, B., Prentice, I. C., Ramankutty, N., Reichenau, T., Schloss, A., Tian, H., Williams, L. J.

and Wittenberg, U.: Carbon balance of the terrestrial biosphere in the twentieth century: Analyses of CO₂, climate and land use effects with four process-based ecosystem models, *Global Biogeochem. Cycles*, 15(1), 183–206, 2001.

Miles, N. L., Richardson, S. J., Davis, K. J., Lauvaux, T., Andrews, A. E., West, T. O., Bandaru, V. and Crosson, E. R.: Large amplitude spatial and temporal gradients in atmospheric boundary layer CO₂ mole fractions detected with a tower-based network in the U.S. upper Midwest, *J. Geophys. Res. Biogeosciences*, 117, 1–13, doi:10.1029/2011JG001781, 2012.

Moss, R. H., Edmonds, J. a, Hibbard, K. a, Manning, M. R., Rose, S. K., van Vuuren, D. P., Carter, T. R., Emori, S., Kainuma, M., Kram, T., Meehl, G. a, Mitchell, J. F. B., Nakicenovic, N., Riahi, K., Smith, S. J., Stouffer, R. J., Thomson, A. M., Weyant, J. P. and Wilbanks, T. J.: The next generation of scenarios for climate change research and assessment., *Nature*, 463, 747–756, doi:10.1038/nature08823, 2010.

Mueller, T., Dressler, G., Tucker, C., Pinzon, J., Leimgruber, P., Dubayah, R., Hurtt, G., Böhning-Gaese, K. and Fagan, W.: Human Land-Use Practices Lead to Global Long-Term Increases in Photosynthetic Capacity, *Remote Sens.*, 6(6), 5717–5731, doi:10.3390/rs6065717, 2014.

Myneni, R. B., Keeling, C. D., Tucker, C. J., Asrar, G. and Nemani, R. R.: Increased plant growth in the northern high latitudes from 1981 to 1991, *Nature*, 386, 698–702, doi:10.1038/386698a0, 1997.

Oechel, W. C., Cowles, S., Grulke, N., Hastings, S. J., Lawrence, B., Prudhomme, T., Riechers, G., Strain, B., Tissue, D. and Vourlitis, G.: Transient nature of CO₂ fertilization in Arctic tundra, *Nature*, 371(6497), 500–503, doi:10.1038/371500a0, 1994.

Oleson, K., Lawrence, D., Bonan, G., Drewniak, B., Huang, M., Koven, C., Levis, S., Li, F., Riley, W., Subin, Z., Swenson, S., Thornton, P., Bozbiyik, A., Fisher, R., Heald, C., Kluzek, E., Lamarque, J.-F., Lawrence, P., Leung, L., Lipscomb, W.,

Muszala, S., Ricciuto, D., Sacks, W., Sun, Y., Tang, J. and Yang, Z.-L.: Technical description of version 4.5 of the Community Land Model (CLM), [online] Available from: <http://opensky.library.ucar.edu/collections/TECH-NOTE-000-000-000-870> (Accessed 30 August 2015), 2013.

Parazoo, N. C., Bowman, K., Frankenberg, C., Lee, J.-E., Fisher, J. B., Worden, J., Jones, D. B. a., Berry, J., Collatz, G. J., Baker, I. T., Jung, M., Liu, J., Osterman, G., O'Dell, C., Sparks, A., Butz, A., Guerlet, S., Yoshida, Y., Chen, H. and Gerbig, C.: Interpreting seasonal changes in the carbon balance of southern Amazonia using measurements of XCO₂ and chlorophyll fluorescence from GOSAT, *Geophys. Res. Lett.*, 40(11), 2829–2833, doi:10.1002/grl.50452, 2013.

Pearman, G. I. and Hyson, P.: Activities of the Global Biosphere as Reflected in Atmospheric CO₂ Records, *J. Geophys. Res.*, 85(C8), 4457–4467 [online] Available from: <http://www.agu.org/pubs/crossref/1980/JC085iC08p04457.shtml>, 1980.

Pearman, G. I. and Hyson, P.: The annual variation of atmospheric CO₂ concentration Observed in the Northern Hemisphere, *J. Geophys. Res.*, 86, 9839–9843, 1981.

Peng, S., Ciais, P., Chevallier, F., Peylin, P., Cadule, P., Sitch, S., Piao, S., Ahlström, A., Huntingford, C., Levy, P., Li, X., Liu, Y., Lomas, M., Poulter, B., Viovy, N., Wang, T., Wang, X., Zaehle, S., Zeng, N., Zhao, F. and Zhao, H.: Benchmarking the seasonal cycle of CO₂ fluxes simulated by terrestrial ecosystem models, *Global Biogeochem. Cycles*, 29(1), 46–64, doi:10.1002/2014GB004931, 2015.

Peters, W., Jacobson, A. R., Sweeney, C., Andrews, A. E., Conway, T. J., Masarie, K., Miller, J. B., Bruhwiler, L. M. P., Páron, G., Hirsch, A. I., Worthy, D. E. J., van der Werf, G. R., Randerson, J. T., Wennberg, P. O., Krol, M. C. and Tans, P. P.: An atmospheric perspective on North American carbon dioxide exchange: CarbonTracker., *Proc. Natl. Acad. Sci. U. S. A.*, 104(48), 18925–18930, 2007.

Peylin, P., Law, R. M., Gurney, K. R., Chevallier, F., Jacobson, a. R., Maki, T., Niwa, Y., Patra, P. K., Peters, W., Rayner, P. J., Rödenbeck, C., van der Laan-Luijkx, I. T.

and Zhang, X.: Global atmospheric carbon budget: results from an ensemble of atmospheric CO₂ inversions, *Biogeosciences*, 10(10), 6699–6720, doi:10.5194/bg-10-6699-2013, 2013.

Piao, S., Sitch, S., Ciais, P., Friedlingstein, P., Peylin, P., Wang, X., Ahlström, A., Anav, A., Canadell, J. G., Cong, N., Huntingford, C., Jung, M., Levis, S., Levy, P. E., Li, J., Lin, X., Lomas, M. R., Lu, M., Luo, Y., Ma, Y., Myneni, R. B., Poulter, B., Sun, Z., Wang, T., Viovy, N., Zaehle, S. and Zeng, N.: Evaluation of terrestrial carbon cycle models for their response to climate variability and to CO₂ trends, *Glob. Chang. Biol.*, 19(7), 2117–2132, doi:10.1111/gcb.12187, 2013.

Prather, M. J., Holmes, C. D. and Hsu, J.: Reactive greenhouse gas scenarios: Systematic exploration of uncertainties and the role of atmospheric chemistry, *Geophys. Res. Lett.*, 39(9), 6–10, doi:10.1029/2012GL051440, 2012.

Le Quéré C., Andres, R. J., Boden, T., Conway, T., Houghton, R. a., House, J. I., Marland, G., Peters, G. P., van der Werf, G. R., Ahlström, A., Andrew, R. M., Bopp, L., Canadell, J. G., Ciais, P., Doney, S. C., Enright, C., Friedlingstein, P., Huntingford, C., Jain, a. K., Jourdain, C., Kato, E., Keeling, R. F., Klein Goldewijk, K., Levis, S., Levy, P., Lomas, M., Poulter, B., Raupach, M. R., Schwinger, J., Sitch, S., Stocker, B. D., Viovy, N., Zaehle, S. and Zeng, N.: The global carbon budget 1959–2011, *Earth Syst. Sci. Data*, 5(1), 165–185, doi:10.5194/essd-5-165-2013, 2013.

Le Quéré C., Moriarty, R., Andrew, R. M., Peters, G. P., Ciais, P., Friedlingstein, P. and Jones, S. D.: Global carbon budget 2014, *Earth Syst. Sci. Data*, 7, 47–85, doi:10.5194/essd-7-47-2015, 2015.

Randerson, J. T., Field, C. B., Fung, I. Y. and Tans, P. P.: Increases in early season ecosystem uptake explain recent changes in the seasonal cycle of atmospheric CO₂ at high northern latitudes, *Geophys. Res. Lett.*, 26(17), 2765–2768, doi:10.1029/1999GL900500, 1999.

Randerson, J. T., Thompson, M. V., Conway, T. J., Fung, I. Y., Field, C. B., Randerson, T., Thompson, V., Conway, J. and Field, B.: The contribution of terrestrial sources and sinks to trends in the seasonal cycle of atmospheric carbon dioxide, *Global Biogeochem. Cycles*, 11(4), 535–560, doi:10.1029/97gb02268, 1997.

Ray, D. K., Ramankutty, N., Mueller, N. D., West, P. C. and Foley, J. a: Recent patterns of crop yield growth and stagnation., *Nat. Commun.*, 3, 1293, doi:10.1038/ncomms2296, 2012.

Reich, P. B. and Hobbie, S. E.: Decade-long soil nitrogen constraint on the CO₂ fertilization of plant biomass, *Nat. Clim. Chang.*, 3(3), 278–282, doi:10.1038/nclimate1694, 2013.

Reich, P. B., Hobbie, S. E., Lee, T., Ellsworth, D. S., West, J. B., Tilman, D., Knops, J. M. H., Naeem, S. and Trost, J.: Nitrogen limitation constrains sustainability of ecosystem response to CO₂. *Nature*, 440(7086), 922–925, doi:10.1038/nature04486, 2006.

Reiners, W.: Terrestrial detritus and the carbon cycle, in US AEC Conf 720510, pp. 317–327., 1973.

Rodenbeck, C., Houweling, S., Gloor, M. and Heimann, M.: CO₂ flux history 1982–2001 inferred from atmospheric data using a global inversion of atmospheric transport, *Atmos. Chem. Phys.*, 3, 1919–1964, doi:10.5194/acpd-3-2575-2003, 2003.

Schneider, M. K., Lüscher, A., Richter, M., Aeschlimann, U., Hartwig, U. a., Blum, H., Frossard, E. and Nösberger, J.: Ten years of free-air CO₂ enrichment altered the mobilization of N from soil in *Lolium perenne* L. swards, *Glob. Chang. Biol.*, 10(8), 1377–1388, doi:10.1111/j.1365-2486.2004.00803.x, 2004.

Schneising, O., Reuter, M., Buchwitz, M., Heymann, J., Bovensmann, H. and Burrows, J. P.: Terrestrial carbon sink observed from space: variation of growth rates and seasonal cycle amplitudes in response to interannual surface temperature

variability, *Atmos. Chem. Phys.*, 14(1), 133–141, doi:10.5194/acp-14-133-2014, 2014.

Sillen, W. M. a and Dieleman, W. I. J.: Effects of elevated CO₂ and N fertilization on plant and soil carbon pools of managed grasslands: A meta-analysis, *Biogeosciences*, 9(6), 2247–2258, doi:10.5194/bg-9-2247-2012, 2012.

Sinclair, T. R.: Historical changes in harvest index and crop nitrogen accumulation, *Crop Sci.*, 38(3), 638–643, doi:10.2135/cropsci1998.0011183X003800030002x, 1998.

Sitch, S., Friedlingstein, P., Gruber, N., Jones, S. D., Murray-Tortarolo, G., Ahlström, A., Doney, S. C., Graven, H., Heinze, C., Huntingford, C., Levis, S., Levy, P. E., Lomas, M., Poulter, B., Viovy, N., Zaehle, S., Zeng, N., Arneth, A., Bonan, G., Bopp, L., Canadell, J. G., Chevallier, F., Ciais, P., Ellis, R., Gloor, M., Peylin, P., Piao, S., Le Quéré C., Smith, B., Zhu, Z. and Myneni, R.: Trends and drivers of regional sources and sinks of carbon dioxide over the past two decades, *Biogeosciences Discuss.*, 10(12), 20113–20177, doi:10.5194/bgd-10-20113-2013, 2015.

Sitch, S., Smith, B., Prentice, I. C., Arneth, A., Bondeau, A. and Cramer, W.: Evaluation of ecosystem dynamics , plant geography and terrestrial carbon cycling in the LPJ dynamic global vegetation model, , 161–185, 2003.

Stocker, B. D., Spahni, R. and Joos, F.: DYPTOP: a cost-efficient TOPMODEL implementation to simulate sub-grid spatio-temporal dynamics of global wetlands and peatlands, *Geosci. Model Dev.*, 7(6), 3089–3110, doi:10.5194/gmd-7-3089-2014, 2014.

Tans, P. P. & Keeling, R.: Trends in Atmospheric Carbon Dioxide, <<http://www.esrl.noaa.gov/gmd/ccgg/trends/>>, 2013.

Taylor, K. E., Stouffer, R. J. and Meehl, G. a.: An Overview of CMIP5 and the Experiment Design, *Bull. Am. Meteorol. Soc.*, 93(4), 485–498, doi:10.1175/BAMS-D-11-00094.1, 2012.

Thompson, R.: The relationship of the phase and amplitude of the annual cycle of CO₂ to phenological events, *Plant Ecol. Divers.*, 4(2-3), 213–226, doi:10.1080/17550874.2011.615347, 2011.

Thoning, K. W., Tans, P. P. and Komhyr, W. D.: Atmospheric carbon dioxide at Mauna Loa Observatory: 2. Analysis of the NOAA GMCC data, 1974–1985, *J. Geophys. Res.*, 94(D6), 8549, doi:10.1029/JD094iD06p08549, 1989.

Tjiputra, J. F., Roelandt, C., Bentsen, M., Lawrence, D. M., Lorentzen, T., Schwinger, J., Seland, Ø. and Heinze, C.: Evaluation of the carbon cycle components in the Norwegian Earth System Model (NorESM), *Geosci. Model Dev.*, 6, 301–325, doi:10.5194/gmd-6-301-2013, 2013.

Tucker, C. J., Fung, I. Y., Keeling, C. D. and Gammon, R. H.: Relationship between atmospheric CO₂ variations and a satellite-derived vegetation index, *Nature*, 319(6050), 195–199, doi:10.1038/319195a0, 1986.

United Nations: *World Population Prospects: The 2015 Revision*, New York., 2015.

Vitousek, P. M., Ehrlich, P. R., Ehrlich, A. H. and Matson, P. A.: Human Appropriation of the Products of Photosynthesis, *Bioscience*, 36(6), 368–373, 1986.

Vitousek, P. M., Porder, S., Houlton, B. Z. and Chadwick, O. a.: Terrestrial phosphorus limitation: Mechanisms, implications, and nitrogen-phosphorus interactions, *Ecol. Appl.*, 20(1), 5–15, doi:10.1890/08-0127.1, 2010.

Volodin, E. M., Dianskii, N. a. and Gusev, a. V.: Simulating present-day climate with the INMCM4.0 coupled model of the atmospheric and oceanic general circulations, *Izv. Atmos. Ocean. Phys.*, 46(4), 414–431, doi:10.1134/S000143381004002X, 2010.

Walther, G., Post, E., Convey, P., Menzel, A., Parmesan, C., Beebee, T. J. C., Fromentin, J., I. O. H. and Bairlein, F.: Ecological response to recent climate change, *Nature*, 416, 389–395, doi:10.2519/jospt.2011.3814, 2002.

Wang, X., Piao, S., Ciais, P., Friedlingstein, P., Myneni, R. B., Cox, P., Heimann, M., Miller, J., Peng, S., Wang, T., Yang, H. and Chen, A.: A two-fold increase of carbon cycle sensitivity to tropical temperature variations., *Nature*, 506(7487), 212–5, doi:10.1038/nature12915, 2014.

Watanabe, S., Hajima, T., Sudo, K., Nagashima, T., Takemura, T., Okajima, H., Nozawa, T., Kawase, H., Abe, M., Yokohata, T., Ise, T., Sato, H., Kato, E., Takata, K., Emori, S. and Kawamiya, M.: MIROC-ESM 2010: model description and basic results of CMIP5-20c3m experiments, *Geosci. Model Dev.*, 4, 845–872, doi:10.5194/gmd-4-845-2011, 2011.

Wei, Y., Liu, S., Huntzinger, D. N., Michalak, A. M., Viovy, N., Post, W. M., Schwalm, C. R., Schaefer, K., Jacobson, A. R., Lu, C., Tian, H., Ricciuto, D. M., Cook, R. B., Mao, J. and Shi, X.: The North American Carbon Program Multi-scale Synthesis and Terrestrial Model Intercomparison Project – Part 2: Environmental driver data, *Geosci. Model Dev.*, 7(6), 2875–2893, doi:10.5194/gmd-7-2875-2014, 2014.

Whittaker, R. H. and Likens, G. E.: Primary production: The biosphere and man, *Hum. Ecol.*, 1(4), 357–369, doi:10.1007/BF01536732, 1973.

Williams, D. N., Taylor, K. E., Cinquini, L., Evans, B., Kawamiya, M., Lawrence, B. N. and Middleton, D. E.: The Earth System Grid Federation : Software Framework Supporting CMIP5 Data Analysis and Dissemination, *CLIVAR Exch.*, 16(56), 40–42, 2011.

Yukimoto, S., Yoshimura, H., Hosaka, M., Sakami, T., Tsujino, H., Hirabara, M., Tanaka, T. Y., Deushi, M., Obata, A., Nakano, H., Adachi, Y., Shindo, E., Yabu, S.,

Ose, T. and Kitoh, A.: Meteorological Research Institute-Earth System Model Version 1 (MRI-ESM1), Tech. Reports, 64, 88, 2011.

Zaehle, S. and Friend, a. D.: Carbon and nitrogen cycle dynamics in the O-CN land surface model: 1. Model description, site-scale evaluation, and sensitivity to parameter estimates, *Global Biogeochem. Cycles*, 24(1), 1–13, doi:10.1029/2009GB003521, 2010.

Zeng, N.: Glacial-interglacial atmospheric CO₂ change - The glacial burial hypothesis, *Adv. Atmos. Sci.*, 20, 677–693, doi:10.1007/bf02915395, 2003.

Zeng, N., Mariotti, A. and Wetzel, P.: Terrestrial mechanisms of interannual CO₂ variability, *Global Biogeochem. Cycles*, 19, doi:Gb1016 10.1029/2004gb0022763, 2005a.

Zeng, N., Qian, H., Roedenbeck, C. and Heimann, M.: Impact of 1998–2002 midlatitude drought and warming on terrestrial ecosystem and the global carbon cycle, *Geophys. Res. Lett.*, 32(22), L22709, doi:10.1029/2005GL024607, 2005b.

Zeng, N., Zhao, F., Collatz, G. J., Kalnay, E., Salawitch, R. J., West, T. O. and Guanter, L.: Agricultural Green Revolution as a driver of increasing atmospheric CO₂ seasonal amplitude, *Nature*, 515(7527), 394–397, doi:10.1038/nature13893, 2014.

Zhao, F. and Zeng, N.: Continued increase in atmospheric CO₂ seasonal amplitude in the 21st century projected by the CMIP5 Earth system models, *Earth Syst. Dyn.*, 5(2), 423–439, doi:10.5194/esd-5-423-2014, 2014.

Zimov, S. A., Davidov, S. P., Zimova, G. M., Davidova, A. I., Chapin, F. S., Chapin, M. C. and Reynolds, J. F.: Contribution of Disturbance to Increasing Seasonal Amplitude of Atmospheric CO₂, *Science*, 284, 1973–1976, doi:10.1126/science.284.5422.1973, 1999.